FINAL REPORT

CHARACTERIZATION OF REACTION KINETICS IN A POROUS ELECTRODE

NAG 3-649

Principal Investigator:
Professor Peter S. Fedkiw
Department of Chemical Engineering
North Carolina State University
Raleigh, NC 27695-7905

Grant Monitor:
Mr. Norman H. Hagedorn
NASA Lewis Research Center
21000 Brookpark Avenue, MS 301-3
Cleveland, OH 44135

Prepared: April 23, 1990

TABLE OF CONTENTS

SECTION 1

SUMMARY

This is the final report for the NASA Lewis funded grant "Characterization of Reaction Kinetics in a Porous Electrode" (originally titled "Cyclic Voltammetry in a Porous Electrode"). The name change was approved in the third-project year to reflect the more general electroanalytical nature of the mathematical methodology which was being developed.

Our objective has been to develop a procedure by which electrode reaction kinetic constants can be extracted from impedance or linear sweep voltammetry measurements on a porous electrode. The mathematical theory to interpret such measurements on planar electrodes is well known; however, due to the three-dimensional, distributed reaction distribution in a porous electrode, it cannot be rigorously applied to this electrode. By using a tube-analog model for the pore geometry, we have developed such a methodology and it is reported upon in the following sections.

Our approach has been to develop these tools using simplified redox kinetics (Butler-Volmer) as the example reaction sequence. It should be emphasized, however, that more complex reaction expressions can be used within the context of the models with appropriate modification of the computer programs. We have attempted to write the FORTRAN

substitution of alternative kinetic equations possible.

Two chemical engineering graduate students have worked on the project. Mr. Andrew Viner received his MS degree in 1988 for his thesis "A Model of Steady-State and Impedance Measurements in Flooded Porous Electrodes," and currently Mr. John Weidner is working on his PhD dissertation "Linear-Sweep Voltammetry in Porous Nickel Oxide Electrodes" with an anticipated graduation date of no later than May, 1991. Because Mr. Weidner's work is still in progress, this "final" report is not complete. In the last section of the document, the ongoing work is outlined. Upon completion of Mr. Weidner's dissertation, a copy will be forwarded to the grant monitor, Mr. N. Hagedorn.

The following sections of this report are self-contained documents and are presented in the chronological order in which the work described in each was done. Each section has appeared as a paper in a peer-reviewed Journal (Sections 2-4) or is currently being prepared for submission (Section 5). The financial support of the NASA grant has been acknowledged in each publication. A short summary of each follows.

The ohmic resistance in a pore will distort the shape of a voltammogram. As a first attempt to quantitatively understand the phenomena, Section 2 reports upon the ohmic-distortion effect for thin-layer cells when a reversible redox reaction occurs. A simple-to-apply correlation to account for the shift in the peak potential as a function dimensionless solution resistance is presented. The theoretical calculations based on porous electrode theory provide the basis for the correlation.

The MS thesis of Mr. Viner provided an extensive theoretical foundation to calculate the steady-state and transient response of a porous electrode. Two-dimensional, analytical solutions to the diffusion and Laplace equation in the tube geometry were developed, and we demonstrated how the two may be used in a numerical calculation to determine current-voltage behavior when coupled through the reaction-kinetic expression. Section 3 reports upon a specific electroanalytic measurement, the open-circuit impedance, and illustrates how the interaction of ohmic, kinetic, and mass-transfer resistances influence the results. With this methodology available to separate the various resistances, kinetic constants can be extracted from the measured impedance.

During the course of developing the mathematics to predict the voltammogram for a porous electrode, we discovered a minor limitation of the classic Nicholson-Shain treatment for voltammetry at a planar electrode. In their work, the assumption was made that the reactant only is present at the onset of the sweep. From our mathematical development, we determined that if both reactant and product are initially present at comparable concentrations, the peak potential and current for a reversible redox reaction are significantly changed from that predicted by Nicholson and Shain. In Section 4, we report upon this work which is of importance to the electroanalytical community. The magnitude of the effect is a function of the ratio of the initial reactant-to-product concentration ratio times the square root of the ratio of the two diffusivities, and a correlation for the peak potential and current is presented as a function of this variable.

The peak potential and current for linear sweep voltammetry in a pore when ohmic, kinetic, and mass-transfer resistances may all be of importance is presented in Section 5. Again, correlations are presented, based upon the theoretical calculations, which enable the determination of the kinetic constants. This Section is nearly ready for submission for peer review except a few additional calculations must be made, as appropriately noted in the Section.

SECTION 2

OHMIC DISTORTION OF REVERSIBLE VOLTAMMOGRAMS IN THIN-LAYER CELLS

by

Peter S. Fedkiw and John W. Weidner
Department of Chemical Engineering
North Carolina State University
Raleigh, NC 27695-7905

and

M. Paul Kang
NASA Lewis Research Center
Cleveland, Ohio 44135

Published in

Electrochimica Acta, **33**, 421 (1988)

ABSTRACT

A continuum-model approach, analogous to porous electrode theory, has been applied to a thin-layer cell of rectangular and cylindrical geometry. A reversible redox couple is assumed, and the local reaction current density is related to the potential through the formula of Hubbard and Anson for a uniformily accessible thin-layer cell. The placement of the reference electrode is also accounted for in the analysis. Primary emphasis is placed on the effect of the solution-phase ohmic potential drop on the voltammogram characteristics. Correlation equations for the peak-potential displacement from $E^{o'}$ and the peak current are presented in terms of two dimensionless parameters.

Hinman, Pons, and Cassidy [1] discussed the effects of solution-phase resistance on the shape of the voltammogram of a reversible redox couple in a thin-layer cell. In this cell, the working electrode was separated from an insulating plane by a thin gap filled with electrolyte, and a reference electrode was placed between the leading edge of the working electrode and the counterelectrode. Hubbard and Anson's [2] formula for the current in a uniformly accessible, thin-layer cell was used to represent the surface impedance in an equivalent network model. Both a rectangular and a circular geometry for the working electrode were considered. In both cases, the peak potential of the reversible voltammogram was shown to be displaced from $E^{o\prime}$—where it otherwise would be located—by solution-resistance effects. The circular electrode was found to be the better of the two in that, given equal areas, the current wave was less distorted.

In this communication, a one dimensional, porous-electrode model [3] of the cell will be used as an alternative to the network model of Hinman *et al.* The current-voltage behavior was found, as expected, to be identical in the two approaches. However, in formulating the differential equation of the present work, two dimensionless parameters are shown to govern the behavior of the voltammogram. We present correlations which show how the peak-potential displacement from $E^{o\prime}$ and peak current are dependent upon these two parameters. With such relationships available, a thin-layer cell may be, for example, designed with a known deviation from ideal behavior.

MODEL FORMULATION

Consider the rectangular thin-layer cell shown in Figure 1a with the reference electrode located at x = -x_{RE}. Because the cell gap is much smaller than the electrode length, the potential distribution in the electrolyte is assumed to be one dimensional and dependent only upon x. A differential conservation of charge equation may be written as

$$h\frac{di_s}{dx} = -i_n \tag{1}$$

where h is the gap height, i_s is the current density in the solution phase, and i_n is the reaction current density—with a cathodic reaction current being positive. Subject to the assumptions and limitations discussed by Hinman *et al.*, the local reaction current density is calculable from Hubbard and Anson's formula for the current as

$$i_n = \frac{(nF)^2 \nu C_{ox}^o h}{RT} \cdot \frac{exp\left[\frac{nF}{RT}(E - E^{o'})\right]}{\left\{1 + exp\left[\frac{nF}{RT}(E - E^{o'})\right]\right\}^2} \tag{2}$$

Because the potential is position dependent, so must be i_n according to equation 2. If ohm's law is used to relate i_s to the solution potential gradient ($i_s = \kappa \nabla E$ where E is the potential difference between the working and a reference electrode located at position x), the resultant dimensionless differential charge-conservation equation may be written as

$$\frac{d^2E^*}{dX^2} = -\theta\frac{e^{E^*}}{[1 + e^{E^*}]^2} \tag{3}$$

where the dimensionless groupings are defined in the nomenclature. The two requisite bound-

(a)

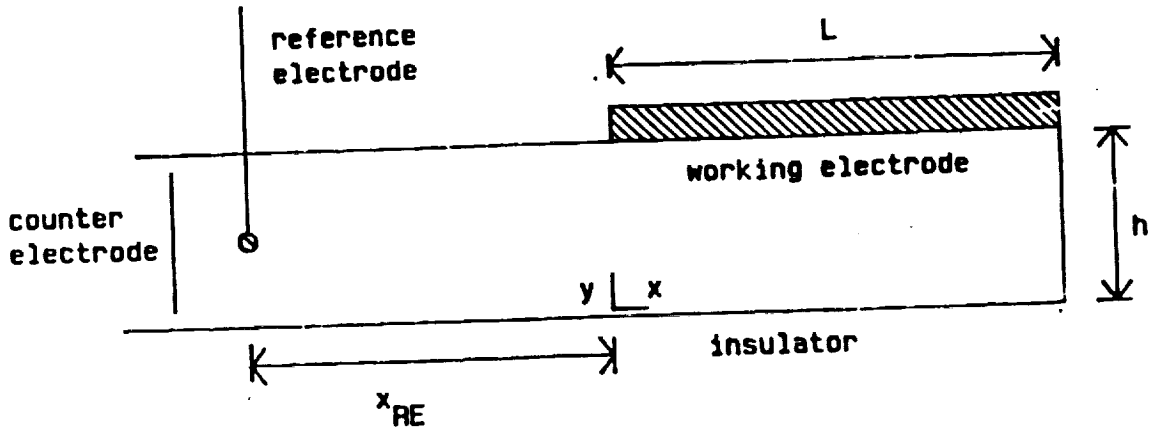

(b)

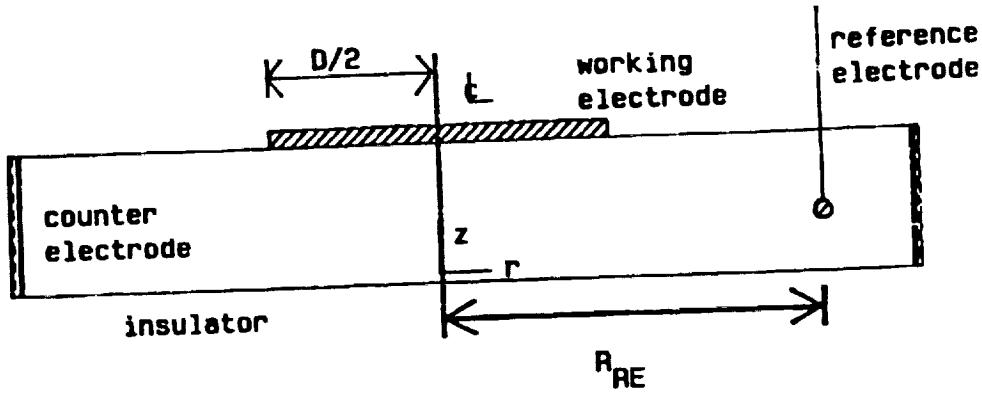

Figure 1: **Schematic illustration of thin-layer cell. (a) Rectangular (b) Circular**

ary conditions reflect the insulating wall at the far end of the working electrode (equation 4a), and the pure ohmic voltage loss from the reference electrode to the leading edge of the working electrode (equation 4b).

$$\frac{dE^*}{dX} = 0, \quad X = 1 \tag{4}$$

$$E^* = E^*_{app} + \gamma \frac{dE^*}{dX}, \quad X = 0 \tag{4}$$

Upon specification of the applied voltage, E^*_{app}, the reference electrode location γ, and the parameter θ, the nonlinear ODE was numerically integrated using the technique given by Newman [4]. With the potential distribution available, the cell current is found by numerical integration of equation 2 along the electrode surface. If the current is normalized by the maximum at $E^{o'}$ in the absence of resistance effects, the result is defined as I and may be calculated from

$$I = 4 \int_0^1 \frac{e^{E^*}}{[1 + e^{E^*}]^2} dX \tag{5}$$

If a circular working electrode is considered (Figure 1b), the dimensionless charge-conservation equation may be written as

$$\frac{1}{X} \frac{d}{dX} \left(X \frac{dE^*}{dX} \right) = -\theta \frac{e^{E^*}}{[1 + e^{E^*}]^2} \tag{6}$$

with boundary conditions

$$\frac{dE^*}{dX} = 0, \quad X = 0 \tag{7}$$

$$E^* = E^*_{app} - \ln\gamma\frac{dE^*}{dX}, \quad X = 1 \tag{7}$$

Numerical integration of equation (6) using Newman's technique enabled a calculation of the integral current as a function of the applied voltage and the two parameters θ and γ.

RESULTS AND DISCUSSION

Calculations using the pore-analog model result in voltammograms identical to those reported by Hinman *et al.* from a network model. For a circular electrode, Figure 2 illustrates the shape of the voltammogram for the anodic portion of the scan ($\theta < 0$). On Figure 2a is shown the dimensionless current vs applied voltage for various values of the parameter θ with the reference electrode located at $\gamma = 1$. Figure 2b presents the same calculation for $|\theta| = 10$, but with the reference electrode located at various positions upstream from the leading edge of the working electrode. The parameter θ is a measure of the relative importance of ohmic resistance. For $|\theta|$ much greater than one, the voltammogram becomes distorted; but if $|\theta|$ is 0(1) or less, the voltammogram assumes the symmetric Nernstian behavior. For example, even at $|\theta| = 10$ with $\gamma = 1$, the peak potential is displaced only 8 mV from $E^{o'}$ (25°C, n = 1); whereas at $|\theta| = 100$ the displacement is 43 mV, and the wave is severly distorted. As the reference electrode is moved farther from the leading edge (Figure 2b), the peak displacement and wave distortion become more pronounced at any value of θ.

The peak current is dependent upon θ but not γ; whereas the peak potential is sensitive

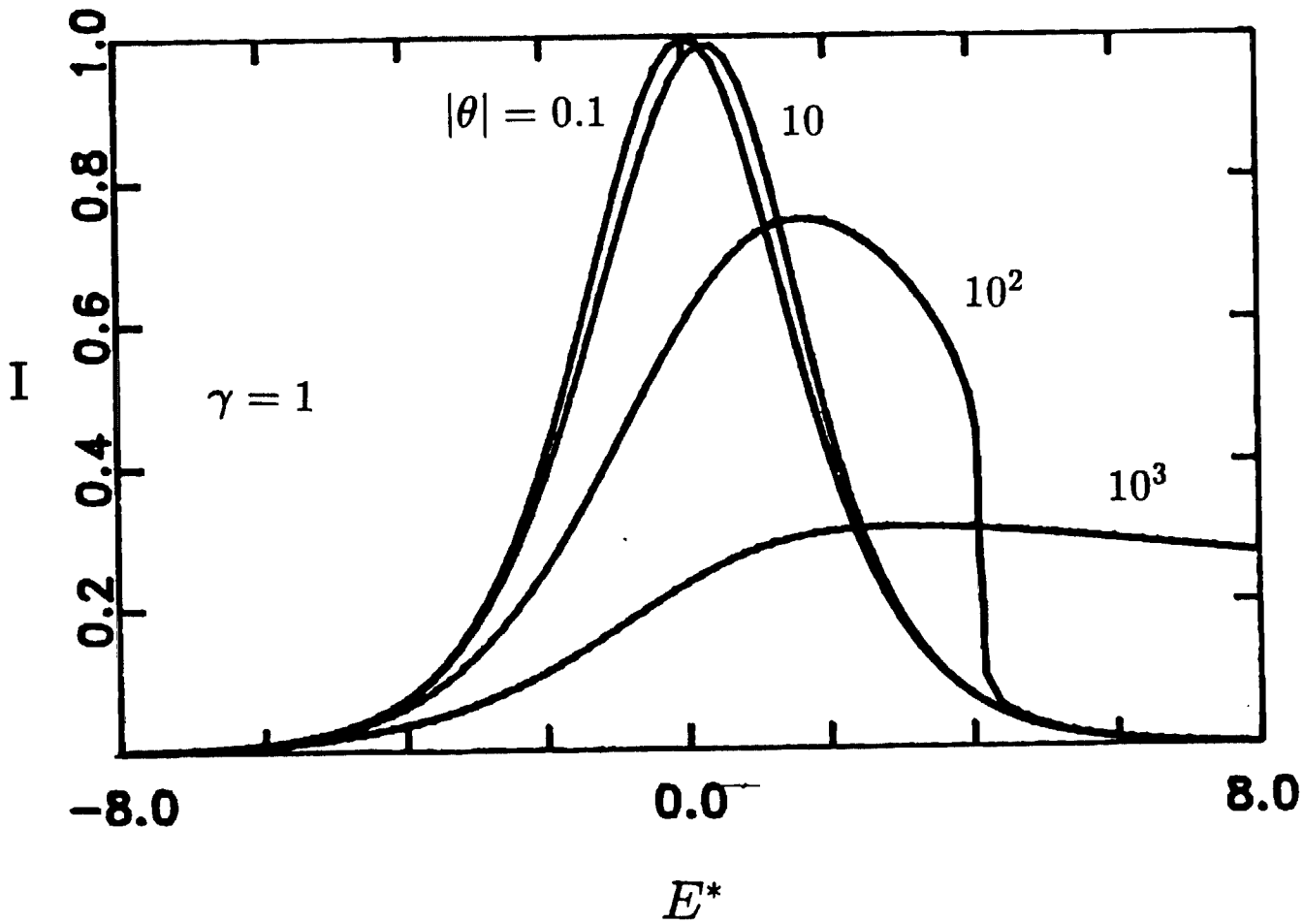

Figure 2. **Anodic portion of voltammogram for reversible redox couple in circular thin-layer cell. (a) Effect of θ with $\gamma = 1$; (b) Effect of γ with $|\theta| = 10$.**

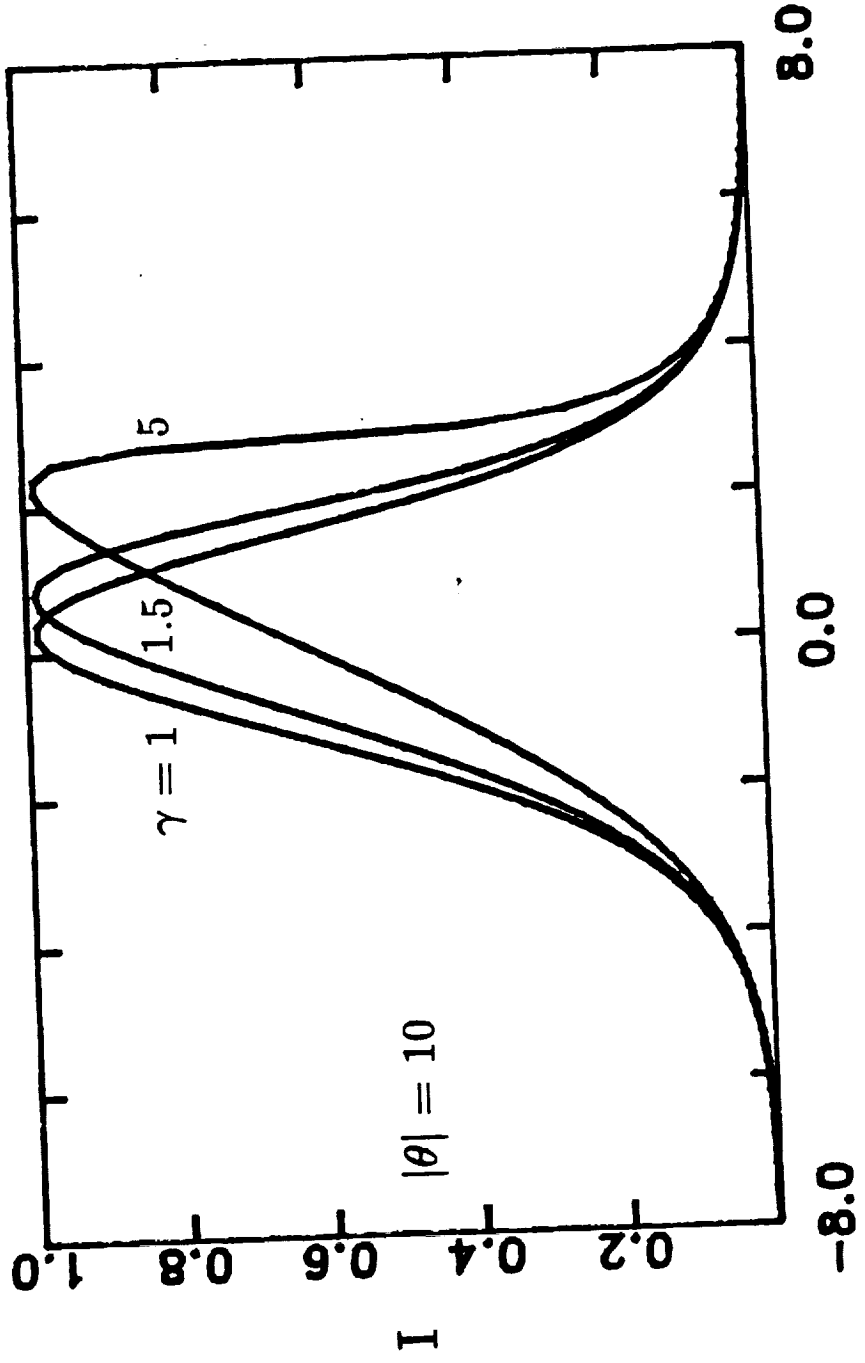

Figure 2b.

to both. The identical behavior is found in the rectangular electrode , but the current-wave distortion occurs at lower $|\theta|$ values in this geometry.

A large number of calculations were performed to generate a relationship between the peak potential and current and the two parameters θ and γ. An empirical relationship was fit to the data as reported below

$$|E_p^*| = \frac{|\theta|}{1/c(\gamma) + |\theta|/b(\gamma)} \tag{8}$$

where b(γ) and c(γ) are polynomial functions of γ as given by

Rectangular electrode:

$$b(\gamma) = 6.9811 + 26.6299\gamma - 0.06605\gamma^2 + 7.084 \times 10^{-4}\gamma^3 \tag{9}$$

$$c(\gamma) = 0.09468 + 0.2621\gamma + 1.694 \times 10^{-3}\gamma^2 - 1.314 \times 10^{-4}\gamma^3 \tag{10}$$

Circular electrode:

$$b(\gamma) = -23.2683 + 29.4229\gamma - 3.3209\gamma^2 + 0.1342\gamma^3 \tag{11}$$

$$c(\gamma) = -0.0765 + 0.1318\gamma - 0.01821\gamma^2 + 9.183 \times 10^{-4}\gamma^3 \tag{12}$$

Figure 3 illustrates these correlations for E_p^* in comparison to the numerically calculated values. The discrepancy between the two is seen to be the largest when the reference electrode is placed at the leading edge and $|\theta|$ is less than 1. However, at these values of γ and θ, wave distortion would be difficult to measure experimentally and is not important.

The peak current, I_p, was also empirically correlated with θ for each electrode geometry and is given below.

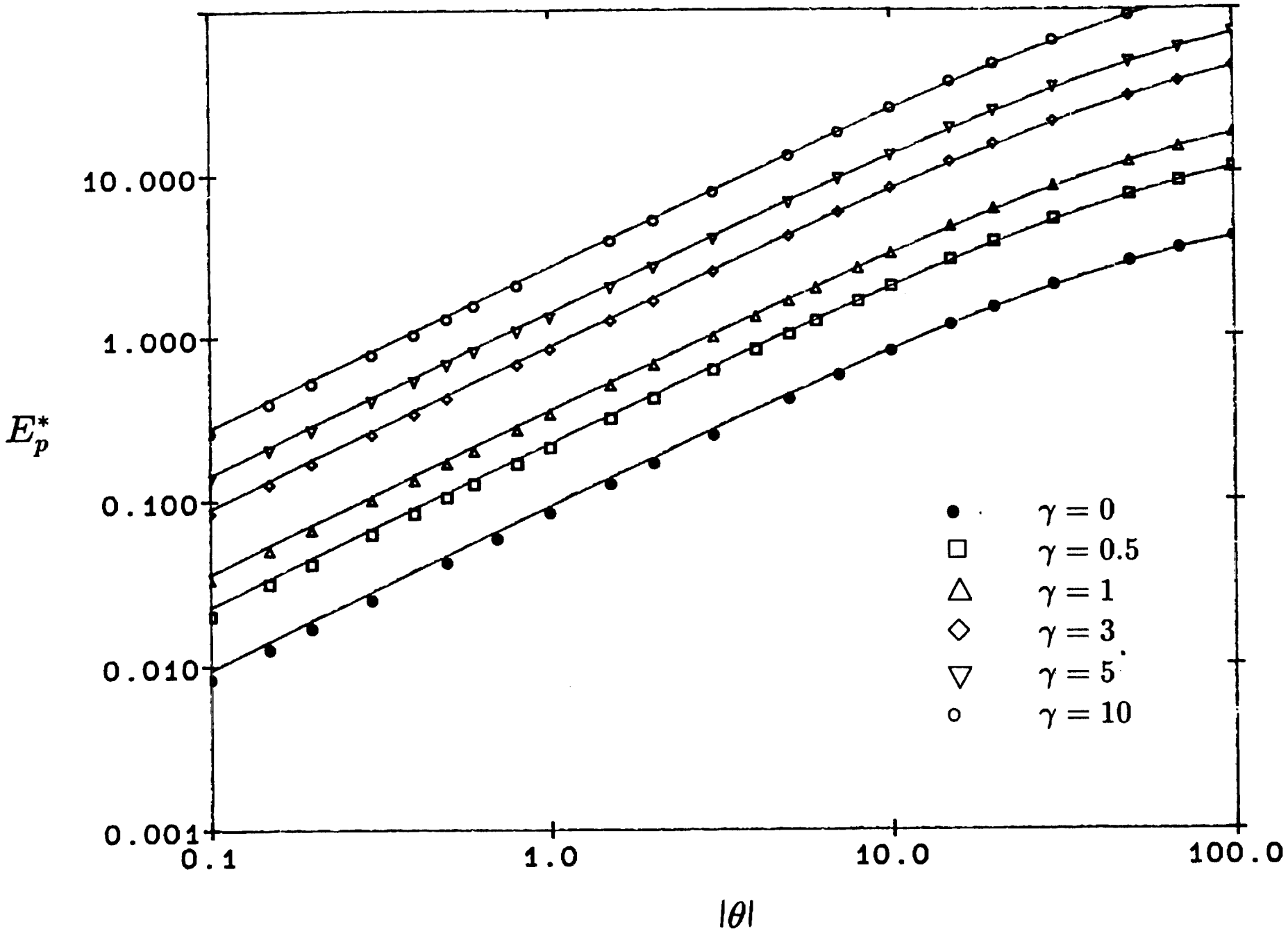

Figure 3. **Dimensionless potential at peak anodic current. The symbols are calculated from the solution of the differential equation and the lines are the empirical fit to these values.**

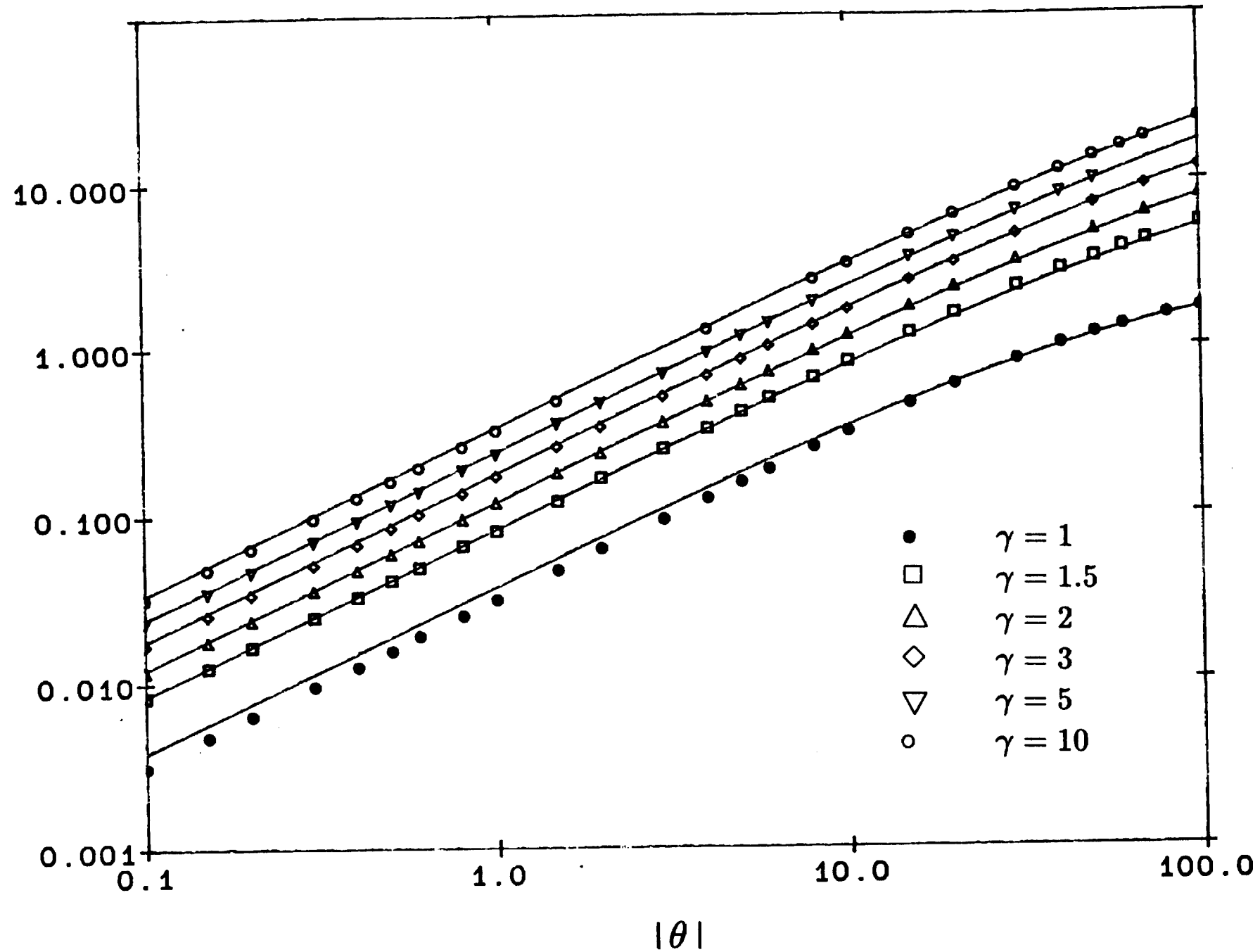
10.000
1.000
0.100
0.010
0.001
0.1
1.0
10.0
100.0
E_p^*
$|\theta|$
$\gamma = 1$
$\gamma = 1.5$
$\gamma = 2$
$\gamma = 3$
$\gamma = 5$
$\gamma = 10$

Figure 3b.

$$Rectangular\ cell: \quad I_p = 1 - 6.237 \times 10^{-3}|\theta|^{0.951} \tag{13}$$

$$Circular\ cell: \quad I_p = 1 - 9.724 \times 10^{-4}|\theta|^{1.219} \tag{14}$$

The correlations may be used, for example, to estimate the size of an electrode which can be used in a particular media to maintain the wave-distortion at an acceptable level, or to anticipate the distortion of the wave due to reference electrode placement. It must be emphasized that these relationships are empirical and should be used with caution outside of the range used to establish the equations: $0.1 \leq |\theta| \leq 10^2$; $0 < \gamma < 10$. This is not a severe limitation considering that at low $|\theta|$ the distortion is unmeasurable, and no experiments would likely be carried out at $|\theta|$ values much larger than 100 where the current wave is grossly distorted.

ACKNOWLEDGMENT

This work was supported by a grant from the NASA Lewis Research Center.

REFERENCES

1. A. Scott Hinman, S. Pons, and J. Cassidy, Electrochimica Acta, 30, 89 (1985); 30, 95 (1985).
2. A. T. Hubbard and C. F. Anson, Analytical Chemistry, 38, 58 (1966).
3. R. DeLevie, Adv. Electrochem. Electrochem. Engr., 6, 329 (1967).
4. J. Newman, Electrochemical Systems, Appendix C, Prentice Hall, NJ (1973).

NOTATION

C^o_{ox}	initial concentration of oxidized species of redox couple, mol/cm^3
D	diameter of circular electrode, cm
E	working electrode voltage relative to reference, V
$E^{o'}$	formal potential of redox couple, V
E^*	dimensionless voltage, $nF(E-E^{o'})/RT$
E^*_p	dimensionless voltage at peak current
E^*_{app}	dimensionless voltage applied at reference electrode
F	Faraday's constant, C/equiv
h	cell gap height, cm
i_n	reaction current density, Eqn. 2, A/cm^2
i_s	solution current density, A/cm^2
I	dimensionless current: rectangular cell—$\int_o^L i_n dx / [(nF)^2 \nu C^o_{ox} hL/4RT]$ circular cell—$\int_o^{D/2} r i_n dr / [(nF)^2 \nu C^o_{ox}(D/2)^2/8RT]$
I_p	dimensionless peak current
L	rectangular electrode length, cm
n	number of e^- in redox couple
r	radial coordinate, cm
R	gas constant

R_{RE}	radial position of reference electrode in circular cell, cm
T	temperature, °K
x	rectilinear coordinate, cm
x_{RE}	position of reference electrode in rectangular cell, cm
X	dimensionless coordinate: rectangular cell—x/L circular cell—2r/D

Greek

γ	dimensionless location of reference electrode: rectangular cell—x_{RE}/L circular cell——$2R_{RE}$/D
κ	solution conductivity, $(ohm \cdot cm)^{-1}$
ν	negative of voltage scan rate, −dE/dt, v/s
θ	dimensionless resistance: rectangular cell--$\left(\frac{nF}{RT}\right)^2 \frac{\nu n F C^{o}_{ox} L^2}{\kappa}$ circular cell—$\left(\frac{nF}{RT}\right)^2 \frac{\nu n F C^{o}_{ox} (D/2)^2}{\kappa}$

SECTION 3

THE IMPEDANCE OF A TUBULAR ELECTRODE: A MODEL FOR A POROUS ELECTRODE

by

Andrew S. Viner
Research Triangle Institute
P.O. Box 12194
Research Triangle Park, NC 27709-2194

Peter S. Fedkiw
Department of Chemical Engineering
North Carolina State University
Raleigh, NC 27695-7905

Published in

Journal of the Electrochemical Society, **137**, 1435 (1990)

ABSTRACT

A cylindrical tube is used as the basis for a two-dimensional mathematical model to calculate the impedance of a flooded porous electrode. The model incorporates charge-transfer, mass-transfer, and ohmic resistances to obtain the axial and radial dependencies of the concentration and potential profiles. A linearized Butler-Volmer kinetic expression for a simple redox reaction $O + e \rightleftharpoons R$ is used, in conjunction with analytical expressions for the surface concentration and overpotential, to compute the open-circuit impedance. The results of the two-dimensional model, which omits double-layer charging, are compared with the results of a more standardly applied one-dimensional model, in which radial variations are neglected, *with* and *without* double-layer charging. The simpler-to-apply one-dimensional model is found to be satisfactory when mass-transfer and ohmic resistances are small with respect to charge-transfer resistance. The omission of double-layer charging does not introduce any error into the two-dimensional model in the frequency range in which capacitive-like effects are caused by mass-transfer limitations.

1 INTRODUCTION

Impedance spectroscopy is a powerful tool for analyzing the kinetics of electrode reactions, but its application to porous electrode systems has been hindered by the lack of a comprehensive model for analyzing the frequency-response data. This paper presents a two-dimensional mathematical model of mass and charge transport in a tube-analog model of a pore in a porous electrode and has been used to predict the current density distribution in response to both a steady and a sinusoidally oscillating potential for a redox reaction $O + e \rightleftharpoons R$. The details of the model are described below, along with sample results for the open-circuit impedance and a comparison of results from the two-dimensional model with a more simplified one-dimensional model. The details of the steady-state model are presented elsewhere [1] .

Considerable effort has been invested in the analysis of impedance measurements for porous electrodes; however, mathematical complexity has generally limited the development to one-dimensional models. One of the early workers in this area was Winsel [2] who solved the two-dimensional Laplace equation for the potential distribution in a cylindrical pore given an arbitrary expression for the current at the pore wall. He proposed a constant interfacial impedance comprised of a sum of parallel impedances arising from double-layer capacitance and coupled diffusion and reaction impedances. A linearized Butler-Volmer expression was used to describe the current-overpotential relation. Winsel

simplified the problem by approximating the radial diffusion of reactants and products as simply linear diffusion to and from a flat plane, thereby limiting the model to large pore diameters and high frequencies.

Darby [3,4] developed a model for the diffusional impedance based on a radially-averaged concentration while ignoring ohmic drop within the pore. De Levie [5] considered the case in which only kinetic resistance was significant. Keddam et al. [6] proposed a one-dimensional model incorporating both charge- and mass-transfer resistance while ignoring the effects of ohmic resistance. One of the most ambitious models was that of Rangarajan [7] who developed a one-dimensional model for the impedance in a pore including charge- and mass-transfer resistance extending from within the pore to a distance δ outside of the pore. A linearized Butler-Volmer expression was used to describe the current-overpotential relation. Keiser *et al.* [8] incorporated a variable-pore diameter into a one-dimensional microscopic model of a pore. Cachet and Wiart [9] developed a one-dimensional model similar to that of Rangarajan, extending it to conditions far from the equilibrium potential.

Most of these models are based on a one-dimensional description of the concentration or potential field within the pore. The present work follows the course first set by Winsel [2]; i.e., development of a two-dimensional model of the concentration and potential fields in a cylindrical pore. In the present case, the local impedance is a function of distance from the pore entrance; however, for the sake of simplicity, double-layer capac-

itance has been ignored. (Note, however, that an analytical expression has been obtained to incorporate the effects of double-layer charging [see Reference [1]]).

The details of the two-dimensional model are presented below, along with the description of a one-dimensional model which includes double-layer charging. A sensitivity analysis is presented to describe the results of the two-dimensional model under a variety of conditions. A comparison of the impedance predictions from the one- and two-dimensional models indicates the conditions under which the approximations in the one-dimensional model fail. Finally, impedance predictions from the one-dimensional model including double-layer charging are compared with those from the two-dimensional model to assess the impact of neglecting double-layer charging from the two-dimensional model.

2 THEORETICAL DEVELOPMENT

2.1 Assumptions

For the purpose of model development, a porous electrode is assumed to consist of a solid phase permeated by a series of identical, non-interconnected cylindrical pores that are filled with an electrolyte solution. Since all tubes are equivalent in this idealized electrode, the behavior of the complete electrode will be the same as that predicted for a single tube. Alternatively, it is possible to predict the performance for several different tube sizes and then combine the results based on a given pore-size frequency distribution, as suggested by Winsel [2] and de Levie [5].

A cylindrical tube of diameter d extends from $z = 0$ to a distance L within the electrode. At the pore aperture ($z = 0$), the tube is exposed to the bulk solution containing both oxidized species O and reduced species R. The potential at the inlet of the tube is potentiostatically controlled. The inner wall of the tube is electroactive and the end wall ($z = L$) is inactive. Other assumptions are:

1. The solid phase is isopotential.
2. The reaction is a simple redox reaction with both reactant and product soluble ($O + e \rightleftharpoons R$).
3. No other processes limit or alter the rates of mass transfer and charge transfer (i.e. no adsorption or desorption and no preceding or following reactions).
4. The electrolyte is well supported so that the solution phase potential is governed by the Laplace equation and migration is insignificant.
5. Diffusion is the only mass-transfer mechanism.
6. There is no uncompensated resistance from the reference electrode to the pore aperture.
7. The reactant and product species have equal diffusivities ($\mathcal{D}_O = \mathcal{D}_R = \mathcal{D}$).
8. The electrolyte reservoir at the pore aperture is well mixed so that there is no mass-transfer resistance from the bulk solution to tube inlet.
9. The potential and reagent concentrations are radially uniform at the mouth of the tube.

Assumptions 1–5 are common to most models of porous electrodes, although some models, such as that of Grens and Tobias [10,11], include the effects of migration and variable conductivity. Grens [12] addresses the importance of these and other assumptions for the prediction of steady-state current density with a one-dimensional model. For the systems to

be considered here (i.e. simple redox reactions in well-supported electrolyte) it is reasonable to neglect those effects. Assumptions 6–7 limit the scope of the model slightly, however, they are invoked for the sake of mathematical convenience. If different diffusivities were included for oxidized and reduced species, then separate concentration profiles would result for each and the amount of "bookkeeping" required in the calculations would be increased. The greatest limitations in the proposed model arise from Assumptions 8 and 9. An approximate boundary condition could be invoked to eliminate the need for Assumption 8 as was done recently in a similar analysis [13]. A more difficult problem arises in trying to eliminate Assumption 9. In reality, the concentration and potential gradients at the inlet of the tube will be radially dependent. The concentration gradient will be greatest near the wall of the tube and decrease towards the centerline of the tube. A rigorous treatment of this problem would require the simultaneous solution of the diffusion equations inside and outside of the tube — a fairly intractable problem.

2.2 Solution to Transport Equations

The development of the impedance model begins with the general time-dependent description of mass and charge transfer in a cylindrical tube. Once the transport equations have been solved, then the specific case of impedance measurements can be simulated by application of a sinusoidal potential at the aperture.

The concentration profile for both species of the redox couple is governed by

Fick's second law

$$\frac{\partial C_O}{\partial t} = \mathcal{D}\nabla^2 C_O \tag{1}$$

where C_O is the O species concentration and $\mathcal{D}$ is the diffusivity. The concentration is initially uniform throughout the tube and equal to the bulk concentration. The concentration at the inlet of the tube is constant at the bulk concentration and there is no diffusion through the end wall of the tube. In the radial direction, the concentration profile is symmetrical about the centerline of the tube and the flux at the tube wall is proportional to the reaction rate. These constraints can be expressed mathematically as

$$\text{(1a) } t = 0;\ C_O(r,z) = C_O^o$$

$$\text{(1b) } z = 0;\ C_O(r,0) = C_O^o \qquad \text{(1d) } r = 0;\ \frac{\partial C_O}{\partial r} = 0$$

$$\text{(1c) } z = L;\ \frac{\partial C_O}{\partial z} = 0 \qquad \text{(1e) } r = d/2;\ -\mathcal{D}\frac{\partial C_O}{\partial r} = j(z,t)$$

where C_O^o is the bulk concentration of the species and $j(z,t)$ is the molar reaction flux at the wall of the tube.

Laplace's equation governs the solution potential Φ_2

$$0 = \nabla^2 \Phi_2 \tag{2}$$

As with the concentration profile, the potential is symmetrical about the centerline of the tube and the current density at the tube wall is the sum of the reaction current density and double-layer charging. It is assumed that no current flows through the end wall of the tube and at the inlet the potential varies according to a known time-dependent function.

These constraints can be expressed mathematically as

$$\text{(2a) } z = 0;\ \Phi_2 = \Phi_2^o(t) \quad \text{(2c) } r = 0;\ \frac{\partial \Phi_2}{\partial r} = 0$$

$$\text{(2b) } z = L;\ \frac{\partial \Phi_2}{\partial z} = 0 \qquad \text{(2d) } r = d/2;\ \kappa \frac{\partial \Phi_2}{\partial r} = i_n(z,t) + C_{dl} \frac{\partial (\Phi_1 - \Phi_2)}{\partial t}$$

where $\Phi_2^o(t)$ is the applied potential at the mouth of the tube, κ is the solution conductivity, $i_n(z,t)$ is the reaction current (related to $j(z,t)$ of Equation 1e by Faraday's law), C_{dl} is the double-layer capacitance, and Φ_1 is the solid phase potential (assumed constant).

The concentration and potential profiles are obtained by first solving Equations 1 and 2 for a delta function distribution both in space and time for $j(z,t)$ and $i_n(z,t)$. A separation of variables and Laplace transform procedure was used to find these solutions as described in Reference [1]. The resulting dimensionless concentration and overpotential are indicated by $\tilde{\theta}(R, Z, Z_0, \tau)$ and $\tilde{\eta}(R, Z, Z_0, \tau)$, respectively. A convolution (in time) and superposition (in space) integral was then applied to write θ and η for any arbitrary $j(z,t)$ and $i_n(z,t)$ as

$$\theta(R, Z, \bar{t}) = \int_0^{\bar{t}} \int_0^{\gamma} \tilde{\theta}(R, Z, Z_o, \bar{t} - \tau)\, \mathcal{J}(Z_o, \tau)\, d\tau\, dZ_o \tag{3}$$

$$\eta(R, Z, \hat{t}) = \int_0^{\hat{t}} \int_0^{\gamma} \tilde{\eta}(R, Z, Z_o, \hat{t} - \tau)\, \mathcal{I}(Z_o, \tau)\, d\tau\, dZ_o \tag{4}$$

where $\mathcal{J}(Z_o, \tau)$ and $\mathcal{I}(Z_o, \tau)$ are the dimensionless analogs of $j(z,t)$ and $i_n(z,t)$ as defined in the Nomenclature section. Note that the dimensionless time scale is different in the two equations; a characteristic diffusion time (t_D) and a double-layer charging time (t_{dl}) are used. Further simplification is possible by recognizing that only the quantities at the tube

wall are of interest. Therefore, we define

$$\theta_w(Z,\bar{t}) = \theta(R=1,Z,\bar{t})$$

$$\eta_w(Z,\hat{t}) = \eta(R=1,Z,\hat{t})$$

and write

$$\theta_w(Z,\bar{t}) = -4\sum_{n=1}^{\infty}\int_0^{\bar{t}}\int_0^{\gamma}\mathcal{J}(Z_0,\tau)\frac{\sin\beta_n Z_0}{\gamma}\sin\beta_n Z\, e^{-\beta_n^2(\bar{t}-\tau)} \times\left[1+\sum_{j=1}^{\infty}e^{-\delta_j^2(\bar{t}-\tau)}\right]d\tau\, dZ_0 \tag{5}$$

and

$$\eta_w(Z,\hat{t}) = \eta^o(\hat{t}) + \frac{2}{\gamma}\sum_{n=1}^{\infty}\frac{I_1(\beta_n)}{I_0(\beta_n)}\sin\beta_n Z\int_0^{\hat{t}}\eta^o(\tau)e^{-\sigma_n(\hat{t}-\tau)}\,d\tau -\frac{2}{\gamma}\sum_{n=1}^{\infty}\sin\beta_n Z\int_0^{\gamma}\int_0^{\hat{t}}\left[\mathcal{I}(Z_0,\tau)\sin\beta_n Z_0 e^{-\sigma_n(\hat{t}-\tau)}\right]d\tau\, dZ_0 \tag{6}$$

where the analytical expression for $\bar{\eta}$ and $\bar{\theta}$ have been used and $\beta_n = (n-\frac{1}{2})\pi/\gamma$, δ_j are the zeroes of the Bessel function $J_1(\delta)$, $I_0(u)$ and $I_1(u)$ are modified Bessel functions, and $\sigma_n = \beta_n I_1(\beta_n)/I_0(\beta_n)$. No further integration of Equations 5 and 6 can be carried out until functional dependencies are specified for $\mathcal{J}(Z_0,\bar{t})$ and $\mathcal{I}(Z_0,\hat{t})$. At steady-state conditions, equations 5 and 6 are linearily related because both the potential and concentration profile are governed by the Laplace equation and have similar boundary conditions; hence, only one is needed to calculate the reaction profiles in this circumstance.

In summary, Equations 5 and 6 give the expressions for the concentration and overpotential at the tube wall, respectively, and were generated by the solution to the two-dimensional fields subject to the assumptions and boundary conditions listed above.

Note that neither the overpotential function $\eta^o(\hat{t})$, the mass flux $\mathcal{J}(Z,\bar{t})$, nor the reaction current $\mathcal{I}(Z,\hat{t})$ at the wall have been specified in these equations and can be any arbitrary function. Of course, there is the requirement that mass flux and reaction current must be proportional, according to Faraday's law. In the most general case, the electrochemical reaction rate is a function of the concentration and overpotential at the tube wall through the kinetic expression. This introduces two levels of complication in the use of Equations 5 and 6. First, the kinetic equations are typically non-linear and second, the equations are coupled, since $\mathcal{J}(Z,\bar{t})$ and $\mathcal{I}(Z,\hat{t})$ are both functions of θ_w and η_w. An added complication arises from the two different characteristic times used to make these equations dimensionless; nevertheless, Equations 5 and 6 can be evaluated numerically. A considerable savings of computation time is realized by linearization of the kinetic expression. For the purpose of model development, it is further assumed that the capacitance of the double-layer is negligible, so that only faradaic current need be considered. This assumption simplifies the analysis because the double-layer charging time scale is eliminated; however, it has the disadvantage that it eliminates double-layer charging from the impedance model and consequently limits the frequency range over which the model is applicable. Additional analysis has been completed to include double-layer charging in the impedance model at the expense of added complexity [1]; however, the results presented below do not include it.

Elimination of double-layer charging does not affect the expression for the con-

centration profile (Equation 5), however, the overpotential equation will be different. The modification is accomplished by dropping the second term on the right side of boundary condition 2d. With this simplification, the solution to Equation 2 at the pore wall is

$$\eta_w(Z,\bar{t}) = \eta^o(\bar{t}) - \frac{2}{\gamma}\sum_{n=1}^{\infty}\frac{I_0(\beta_n)}{\beta_n I_1(\beta_n)}\sin\beta_n Z \int_0^{\gamma}\mathcal{I}(Z_0,\bar{t})\sin\beta_n Z_0\, dZ_0 \qquad (7)$$

This result is equivalent to Equation 9 of Winsel [2], in which double-layer charging is also ignored. With this result, the time dependence is now entirely in terms of the diffusion time scale.

2.3 Impedance Calculation

In principle, Equations 5 and 7 could be used to calculate the current-voltage-time behavior for any arbitrary imposed voltage and kinetic equation. However, the numerical evaluation of these equations would be quite difficult since it involves the double integration of the product of infinite sums (Equation 5). In addition, for a non-linear kinetic equation (e.g. the Butler-Volmer expression) an iterative procedure would have to be applied at each time step in the calculations. Fortunately, this calculational burden can be avoided in calculating the impedance at the open-circuit potential as shown below.

For small-amplitude oscillations about an arbitrary steady-state potential, the dimensionless mass flux can be approximated by a first-order Taylor-series expansion

$$\mathcal{J}(\theta,\eta) = \mathcal{J}_{ss} + \alpha_1(\theta-\theta_{ss}) + \alpha_2(\eta-\eta_{ss}) \qquad (8)$$

where $\mathcal{J}_{ss}$ is the mass flux at the steady-state potential, and α_1 and α_2 are the partial derivatives of $\mathcal{J}$ with respect to θ and η, respectively. For the case of oscillation about the open circuit potential $\mathcal{J}_{ss} = \theta_{ss} = \eta_{ss} = 0$; however, for the sake of generality we will retain the form

$$\mathcal{J}(\theta,\eta) = \mathcal{J}^o + \alpha_1\theta_w(Z,\bar{t}) + \alpha_2\eta_w(Z,\bar{t}) \tag{9}$$

where $\mathcal{J}^o$ incorporates all of the steady-state terms. A similar equation can be written for the reaction current density

$$\mathcal{I}(\theta,\eta) = \mathcal{I}^o + \alpha_3\theta_w(Z,t) + \alpha_4\eta_w(Z,t) \tag{10}$$

where $\mathcal{I}^o$ is defined in the same manner as $\mathcal{J}^o$.

The definitions of the Taylor-series coefficients α_i depend on the kinetic expression. For a system governed by the Butler-Volmer expression, the explicit expressions for α_1 and α_2 are

$$\alpha_1 \equiv \left(\frac{\partial\mathcal{J}}{\partial\theta}\right)_{\eta_{ss}} = \Gamma_2\left(\frac{C_O^o}{C_R^o}e^{\alpha_A\eta_{ss}} + e^{-\alpha_C\eta_{ss}}\right) \tag{11}$$

$$\alpha_2 \equiv \left(\frac{\partial\mathcal{J}}{\partial\eta}\right)_{\theta_{ss}} = -\Gamma_2\left[\alpha_A(1-\theta_{ss}\frac{C_O^o}{C_R^o})e^{\alpha_A\eta_{ss}} + \alpha_C(1+\theta_{ss})e^{-\alpha_C\eta_{ss}}\right] \tag{12}$$

where Γ_2 is a constant that relates the reaction current to mass flux and the quantities α_A and α_C are the anodic and cathodic transfer coefficients, respectively. Given that the reaction current and mass flux are related by Faraday's law, the α_i are related

$$\alpha_3 \equiv \left(\frac{\partial\mathcal{I}}{\partial\theta}\right)_{\eta_{ss}} = -\Gamma_1\alpha_1 \tag{13}$$

$$\alpha_4 \equiv \left(\frac{\partial\mathcal{I}}{\partial\eta}\right)_{\theta_{ss}} = -\Gamma_1\alpha_2 \tag{14}$$

For oscillations about the open-circuit potential, $\eta_\infty = 0$ and $\theta_\infty = 0$ so the α_i are constant. However, for conditions other than the open-circuit potential, η_∞, θ_∞, and hence the α_i are functions of position by Equations 11 and 12. Consequently, the quantities $\mathcal{J}^\circ$ and $\mathcal{I}^\circ$, are also functions of position Z and the analysis that is required becomes much more difficult than that which is presented below. Therefore, we shall proceed on the basis that $\mathcal{J}^\circ, \mathcal{I}^\circ$, and the α_i are constants, assuming that an appropriate (approximate) average values can be used when $\eta_\infty \neq 0$.

Equation 10 can be integrated over the pore length to yield the total current once expressions are found for θ_w and η_w. The appropriate functional forms are based on an expansion in the eigenfunctions of the partial differential equations (Eqns. 1 and 2). In this case

$$\theta_w(Z,\bar{t}) = \sum_{n=1}^{\infty} b_n(\bar{t}) \sin \beta_n Z \tag{15}$$

$$\eta_w(Z,\bar{t}) = \eta^\circ(\bar{t}) + \sum_{n=1}^{\infty} a_n(\bar{t}) \sin \beta_n Z \tag{16}$$

The coefficients $a_n(\bar{t})$ and $b_n(\bar{t})$ are unknown functions of time which can be determined by substituting the linearized current and flux (Eqns. 9 and 10) and the assumed expressions for θ_w and η_w (Eqns. 15 and 16) into Equations 5 and 7. Details of the manipulations are summarized in the Appendix. The total dimensionless current density is thus calculated as

$$\mathcal{I}_T = \int_0^\gamma [\mathcal{I}^\circ + \alpha_3 \theta_w(Z) + \alpha_4 \eta_w(Z)]\, dZ$$

$$= \gamma\left[\mathcal{I}^o + \alpha_4\eta^o(\bar{t})\right] + \sum_{n=1}^{\infty}\frac{1}{\beta_n}\left[\alpha_3 b_n(\bar{t}) + \alpha_4 a_n(\bar{t})\right] \tag{17}$$

where explicit expressions for $a_n(\bar{t})$ and $b_n(\bar{t})$ are given by Equations 55 and 56 in the Appendix. Taking $\eta_{ss} = 0$, Equation 17 can be rearranged to yield

$$\mathcal{I}_T = \mathcal{A}\cos\omega t + \mathcal{B}\sin\omega t \tag{18}$$

$$= \sqrt{\mathcal{A}^2 + \mathcal{B}^2}\cos(\omega t - \phi) \tag{19}$$

where

$$\phi = \tan^{-1}(\mathcal{B}/\mathcal{A}) \tag{20}$$

$$\mathcal{A} = \alpha_4\eta_c^o\left[\gamma - \frac{2\alpha_4}{\gamma}\sum_{n=1}^{\infty}\frac{1}{\beta_n^2(\alpha_4+\sigma_n)}\right] + \frac{2\alpha_4}{\gamma\alpha_1}\eta_c^o\sum_{n=1}^{\infty}\left(\frac{\rho_n}{\beta_n}\right)^2\sum_{k=1}^{\infty}\frac{1}{D^*(s_{kn})}\frac{s_{kn}^2}{s_{kn}^2+\bar{\omega}^2} \tag{21}$$

$$\mathcal{B} = -\frac{2\alpha_4}{\gamma\alpha_1}\bar{\omega}\eta_c^o\sum_{n=1}^{\infty}\left(\frac{\rho_n}{\beta_n}\right)^2\sum_{k=1}^{\infty}\frac{1}{D^*(s_{kn})}\frac{s_{kn}}{s_{kn}^2+\bar{\omega}^2} \tag{22}$$

$$\rho_n = \alpha_1\left(1 - \frac{\alpha_4}{\alpha_4+\sigma_n}\right) \tag{23}$$

$$D^*(s_{kn}) = \left(\rho_n + \frac{s_{kn}}{2}\right) - \left(\chi_{kn} - \frac{s_{kn}\rho_n}{2\chi_{kn}}\right)\frac{J_1(\chi_{kn})}{J_0(\chi_{kn})} \tag{24}$$

$$\chi_{kn} = \sqrt{s_{kn} + \beta_n^2} \tag{25}$$

$J_0(\chi)$ and $J_1(\chi)$ are Bessel functions and s_{kn} are the zeros of the function $D(s)$ given by equation 52 in the Appendix. Finally, the dimensionless impedance Z can then be calculated as

$$\frac{\eta^o}{\mathcal{I}} \equiv \mathbf{Z} = |\mathbf{Z}|e^{j\phi} \tag{26}$$

$$= Z_{Re} + jZ_{Im} \tag{27}$$

where

$$|\mathbf{Z}| = \frac{\eta_c^o}{\sqrt{\mathcal{A}^2 + \mathcal{B}^2}} \tag{28}$$

Several observations can be made concerning these equations. First, values of functions $\mathcal{A}$ and $\mathcal{B}$, and hence Z, are determined by the three dimensionless groups α_1, α_4, and γ (length-to-radius ratio) and the dimensionless frequency $\bar{\omega}$, which is related to the dimensional frequency f by the expression

$$\bar{\omega} = 2\pi f \frac{(d/2)^2}{\mathcal{D}} \tag{29}$$

The quantities α_1 and α_4 can be interpreted as

$$\alpha_1 \equiv \frac{\text{mass-transfer resistance}}{\text{charge-transfer resistance}}$$

$$\alpha_4 \equiv \frac{\text{ohmic resistance}}{\text{charge-transfer resistance}}$$

These definitions will be useful in the interpretation of the results presented in the Discussion section.

3 ONE-DIMENSIONAL IMPEDANCE MODEL

The two-dimensional model presented above is a rigorous treatment of transport in a cylindrical tube, however it is incomplete due to the omission of double-layer charging effects. In order to estimate the seriousness of that omission, a simpler, one-dimensional model was developed with double-layer charging included. A comparison of impedance predicted for the two different models will provide insight into the importance of double-layer charging. The comparison will also provide a means to assess when the radial effects neglected by the more commonly used one-dimensional models are important.

The one-dimensional model material- and charge-conservation equations in a dimensionless format are

$$\begin{aligned} \frac{\partial\theta}{\partial\bar{t}} &= \frac{\partial^2\theta}{\partial Z^2} - \mathcal{I}_{1d} \\ &= \frac{\partial^2\theta}{\partial Z^2} - 2\alpha_1\theta - 2\alpha_2\eta \end{aligned} \tag{30}$$

$$Z = 0;\ \theta = 0 \qquad Z = \gamma;\ \frac{\partial\theta}{\partial Z} = 0$$

and

$$\frac{\partial\eta}{\partial\bar{t}} = \lambda\frac{\partial^2\eta}{\partial Z^2} + 4\lambda\alpha_4\theta - 2\lambda\alpha_4\eta \tag{31}$$

$$Z = 0;\ \eta = e^{j\bar{\omega}\bar{t}} \qquad Z = \gamma;\ \frac{\partial\eta}{\partial Z} = 0$$

where $\mathcal{I}_{1d}$ is the reaction current at position Z and the concentration and overpotential are radially-averaged quantities. For convenience, Equations 30 and 31 were derived with

the same coefficients α_i as appear in the two-dimensional model. An important feature of Equation 31 is the inclusion of double-layer charging, which gives rise to the parameter

$$\lambda = \frac{\kappa(d/2)}{2C_{dl}\mathcal{D}} \tag{32}$$

where C_{dl} is the double-layer capacitance (per unit area) of the interface. In effect, λ is the ratio of the diffusion time scale to the double-layer charging time scale.

The solution of these equations is straightforward and is found as

$$\theta = G_1(Z)\, e^{j\bar{\omega}\bar{t}} \tag{33}$$

$$\eta = G_2(Z)\, e^{j\bar{\omega}\bar{t}} \tag{34}$$

where

$$G_1(Z) = \frac{2\alpha_2}{r_1^2 - r_2^2}\left[\frac{\cosh[r_1(Z-\gamma)]}{\cosh(r_1\gamma)} - \frac{\cosh[r_2(Z-\gamma)]}{\cosh(r_2\gamma)}\right] \tag{35}$$

$$\begin{aligned} G_2(Z) = \frac{1}{r_1^2 - r_2^2}\Bigg[&\left(r_1^2 - (2\alpha_1 + j\bar{\omega})\right)\frac{\cosh[r_1(Z-\gamma)]}{\cosh(r_1\gamma)} \\ &- \left(r_2^2 - (2\alpha_1 + j\bar{\omega})\right)\frac{\cosh[r_2(Z-\gamma)]}{\cosh(r_2\gamma)}\Bigg] \end{aligned} \tag{36}$$

$$r_1 = \sqrt{\frac{1}{2}\left[\Psi + \sqrt{\Psi^2 - 4\Pi}\right]} \tag{37}$$

$$r_2 = \sqrt{\frac{1}{2}\left[\Psi - \sqrt{\Psi^2 - 4\Pi}\right]} \tag{38}$$

and

$$\Psi = 2(\alpha_1 + \alpha_4) + \left(1 + \frac{1}{\lambda}\right) j\bar{\omega} \tag{39}$$

$$\Pi = 4\alpha_4(\alpha_1 + 2\alpha_2) - \frac{\bar{\omega}^2}{\lambda} + \left(\frac{2\alpha_1}{\lambda} + 2\alpha_4\right) j\bar{\omega} \tag{40}$$

The average dimensionless current density is the sum of the reaction current and the double-layer charging current

$$\mathcal{I}_{1d} = -2\Gamma_1\alpha_1 \int_0^\gamma \theta(Z)\, dZ - 2\Gamma_1\alpha_2 \int_0^\gamma \eta(Z)\, dZ + \Gamma_1 \int_0^\gamma \left(\frac{\partial \eta}{\partial \bar{t}}\right) dZ \tag{41}$$

The impedance is computed as the ratio of the potential to the resulting current. After manipulation the complete expression for Z becomes

$$\begin{aligned} \frac{1}{\mathbf{Z}} = \frac{1}{r_1^2 - r_2^2} \Bigg[& \left(\left[2\alpha_4 + \frac{j\bar{\omega}}{\lambda}\right] \left(r_1^2 - j\bar{\omega}\right) - \frac{2\alpha_1 j\bar{\omega}}{\lambda} \right) \frac{\tanh(r_1\gamma)}{r_1} \\ & - \left(\left[2\alpha_4 + \frac{j\bar{\omega}}{\lambda}\right] \left(r_2^2 - j\bar{\omega}\right) - \frac{2\alpha_1 j\bar{\omega}}{\lambda} \right) \frac{\tanh(r_2\gamma)}{r_2} \Bigg] \end{aligned} \tag{42}$$

Note that the one-dimensional current density given by Equation 41 is defined on the basis of the aperture area of the pore ($\pi d^2/4$) whereas the current density resulting from the two-dimensional model is based on the total internal area of the pore (πdL). Consequently, the dimensionless impedance computed by the two-dimensional model must be divided by 2 in order to compare with the results of the one-dimensional model.

4 RESULTS AND DISCUSSION

The approach taken in this study was to conduct a parametric evaluation of the two-dimensional impedance model for 27 different combinations of the three governing dimensionless groups: α_1, α_4, and γ. Three values of aspect ratio ($\gamma = 5, 20, 50$) and three values

of the resistance parameters ($\alpha_1, \alpha_4 = 0.1, 1.0, 10.0$) were used in the calculations. These values span the range from short pores ($\gamma = 5$) to fairly long pores ($\gamma = 50$), and a wide range of resistance ratios. A summary of the results of the parametric evaluation will be presented below, followed by a comparison of the results from the two-dimensional model with those obtained from the one-dimensional model in the limit of negligible double-layer capacitance. The comparison of the two models will indicate when it is appropriate to ignore radial dependencies of concentration and overpotential. Lastly, the results of the two-dimensional model will be compared with those obtained from the one-dimensional model when double-layer charging is included so as to assess the importance of its omission from the two-dimensional model. Complete details on the results of the parametric study and further discussion of the numerical calculational procedure can be found in Reference [1].

4.1 Parametric Evaluation of the Two-Dimensional Model

4.1.1 Aspect Ratio

The effect of aspect ratio (i.e., pore length) is illustrated in the Nyquist plot in Figure 1. Dimensional impedances can be obtained by multiplying the dimensionless quantities by $d/2\kappa$ (with units of $\Omega \cdot cm^2$). A total of 36 points were calculated for each curve, spanning 12 decades of frequency. A spline routine was used to draw smooth curves between the points. A limited number of calculated points are shown explicitly in the Figure with the

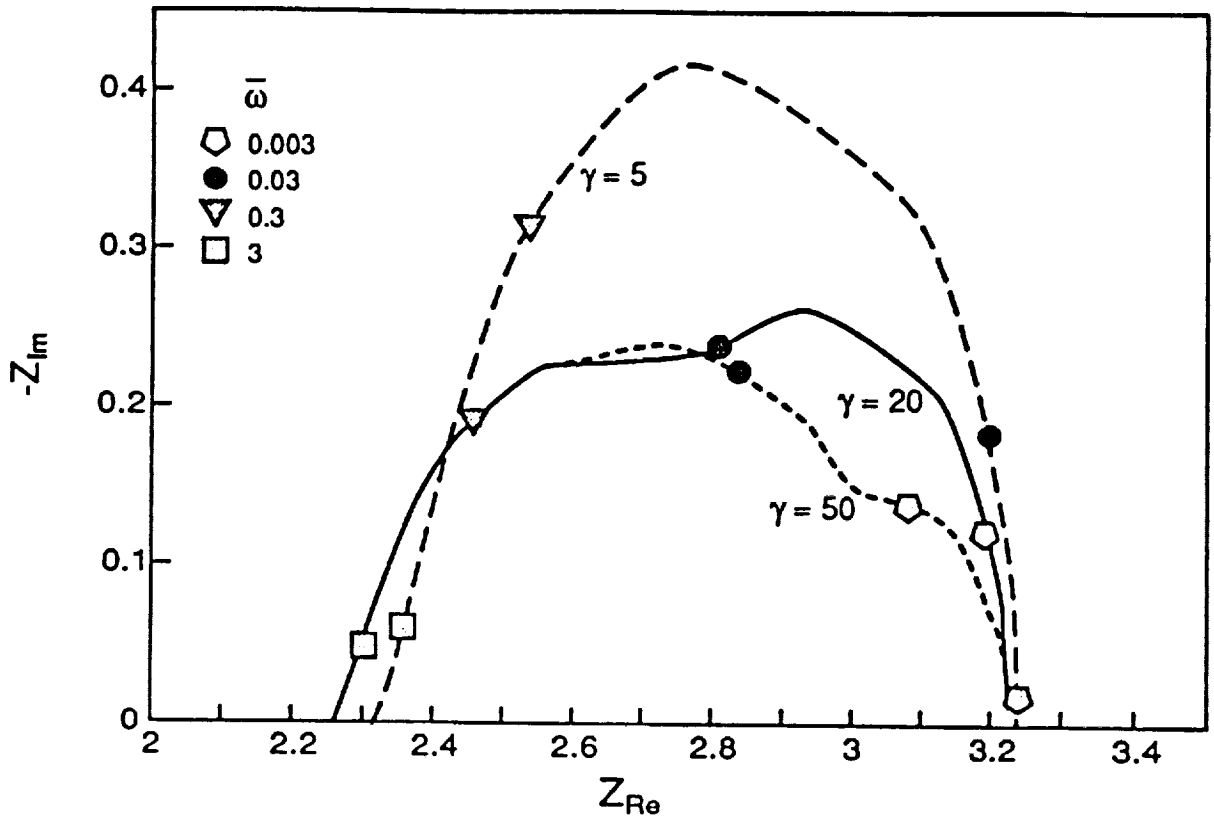

Figure 1: Dimensionless impedance as a function of aspect ratio ($\alpha_1 = \alpha_4 = 0.1$).

corresponding dimensionless frequencies. The three curves in the Figure correspond to short, medium, and long pores.

The model shows that the effective capacitance and resistance are both affected by pore length. The maximum value of Z_{Im} decreases with increasing aspect ratio as does the low frequency limit of Z_{Re}. The curves for $\gamma = 20$ and $\gamma = 50$ converge at a frequency of $\bar{\omega} = 0.3$, suggesting that both behave as semi-infinite pores above this frequency. That is, the impedance predicted at frequencies above $\bar{\omega} = 0.3$ for a pore with an aspect ratio of 20 is the same as that expected for a semi-infinite pore when $\alpha_1 = \alpha_4 = 0.1$.

An interesting feature of Figure 1 is the inflection that occurs in the curves for $\gamma = 20$ (between $\bar{\omega} = 0.03$ and 0.3) and $\gamma = 50$ (between $\bar{\omega} = 0.003$ and 0.03). For some cases reported in Reference [1] (e.g., when $\alpha_1 = \alpha_4 = 0.1$ and $\gamma = 50$), a local minimum occurs, giving the appearance of two separate loops that are added together. The feature is believed to be real (as opposed to a numerical aberration), since similar behavior is predicted by the one-dimensional model of Rangarajan [7] and the one-dimensional model described in Section 3. Presumably the inflection and the local minima are manifestations of the complex, non-spatially uniform interacions between kinetic, ohmic and mass-transfer effects.

4.1.2 Mass-Transfer Resistance

The effect of mass-transfer resistance on the impedance (as measured by the parameter α_1) is shown in Figure 2 for a pore aspect ratio of 20 when ohmic resistance is small with respect to the charge transfer resistance ($\alpha_4 = 0.1$). Note that the smallest loop in Figure 2 ($\alpha_1 = 0.1$) is identical to the loop for $\gamma = 20$ shown in Figure 1. As expected, the maximum values of Z_{Re} and Z_{Im} increase with increasing mass-transfer resistance (i.e. α_1). However, the high frequency limit of Z_{Re} is independent of the mass-transfer resistance. The reason for this behavior is that in the limit as $\bar{\omega} \rightarrow \infty$, the reaction is confined to a thin region near the inlet of the pore where the concentration is fixed through the boundary condition, hence, the high frequency limit of Z_{Re} is not dependent upon mass-transfer resistance. When $\alpha_1 = 10$, neither the low-frequency limit of Z_{Re} nor the maximum value of Z_{Im} is evident, since they occur at frequencies below the lowest value used in the calculations.

4.1.3 Ohmic Resistance

The effect of ohmic resistance on the impedance of a tubular pore is illustrated in Figure 3. The curves in the Figure for $\alpha_4 = 1$ and $\alpha_4 = 10$ are scaled by the factors 10 and 50, respectively, to make them more easily visible on the plot. In fact, the Z_{Re} values for $\alpha_4 = 10$ are actually less than those for $\alpha_4 = 1$, which, in turn, are less than those for $\alpha_4 = 0.1$. This apparently anomalous behavior is actually an artifact of the manner in

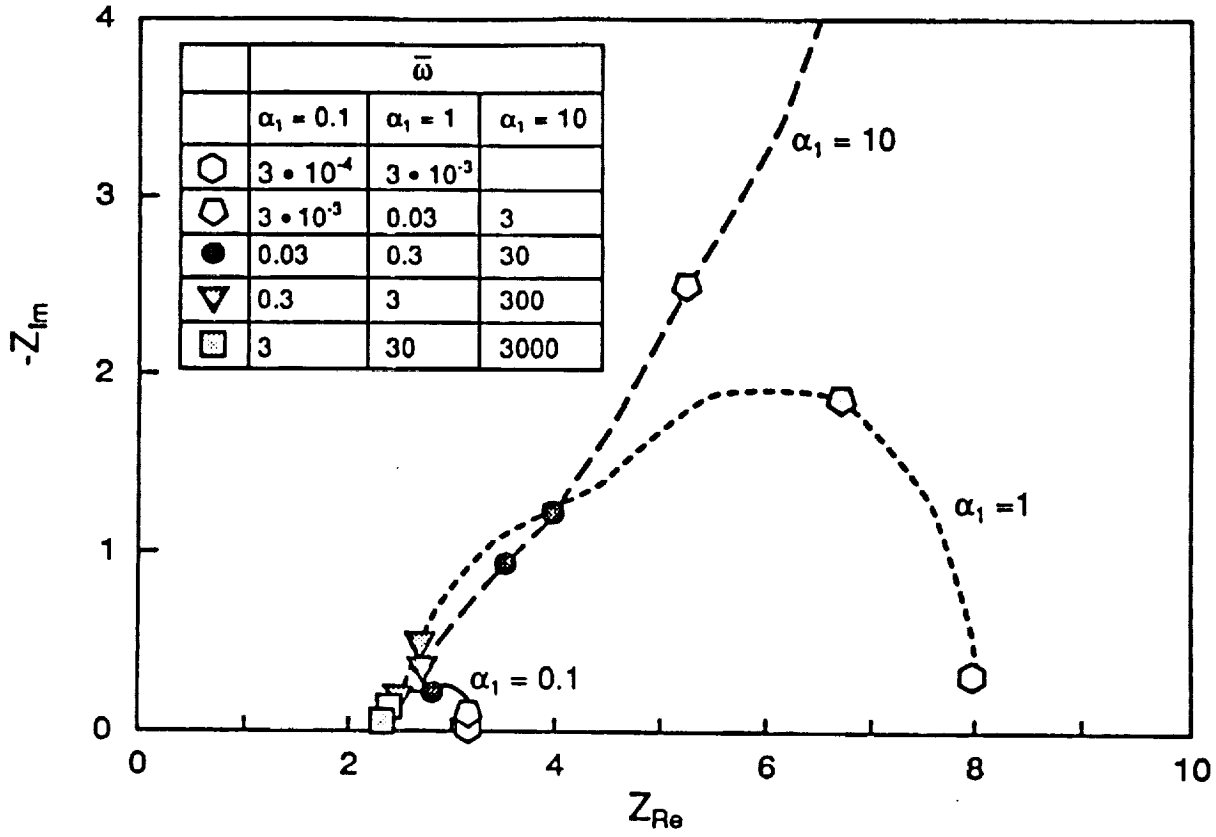

Figure 2: Dimensionless impedance as a function of mass-transfer resistance ($\alpha_1 = 0.1$, $\gamma = 20$).

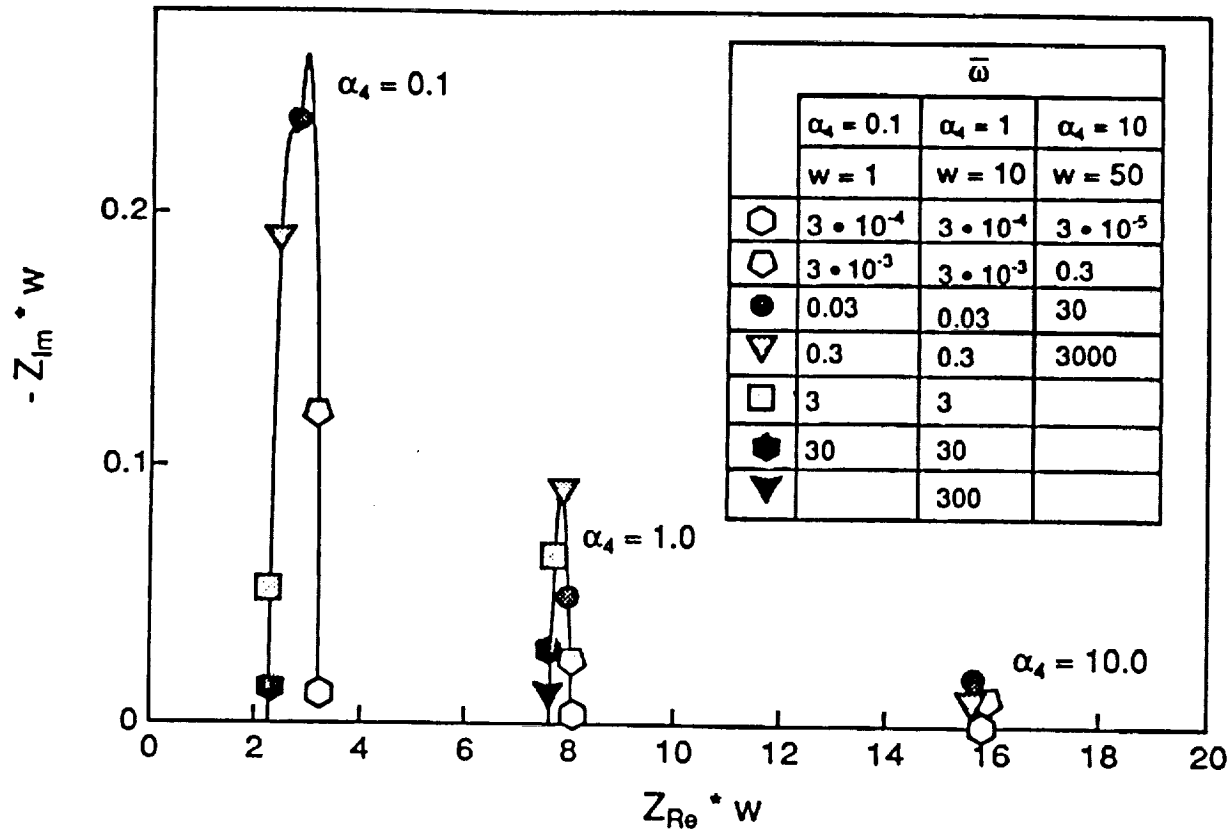

Figure 3: Dimensionless impedance as a function of ohmic resistance. Impedance values computed with $\alpha_4 = 1$ and $\alpha_4 = 10$ are scaled by factors of 10 and 50, respectively. ($\alpha_1 = 0.1$, $\gamma = 20$).

which Z_{Re} is made dimensionless. Specifically, the dimensional impedance is multiplied by $2\kappa/d$. Therefore, as the conductivity decreases, the product of the dimensional impedance and conductivity also decreases. The trend of the capacitance is intuitive: as the ohmic resistance increases, the resulting faradaic and capacitive current decrease.

4.2 Comparison of One- and Two-Dimensional Models for Calculation of the Impedance

The major advantage of the two-dimensional model is that it can be applied in cases where the radially averaged quantities inherent in the one-dimensional models result in poor approximations. Furthermore, with the two-dimensional model available, it can be used to assess the error in one-dimensional approximations. The major disadvantage of the two-dimensional model is that it requires a greater amount of computational effort. The purpose of this section is to assess when that effort is necessary and when the one-dimensional approximation is sufficient. For the results described here, the double-layer capacitance in the one-dimensional model was set to zero.

4.2.1 Parametric Test of One-Dimensional Impedance Model

The one-dimensional model is expected to fail when radial gradients become large (i.e. when mass-transfer and ohmic resistances are large with respect to the charge-transfer resistance). The error in the impedance resulting from the neglect of radial gradients in

concentration and overpotential profiles is illustrated in Figures 4 - 6, which compare the results of the two-dimensional model with those from the one-dimensional model. The data presented in Figure 2 are used as the example for comparison. As expected, when mass-transfer resistance is small with respect to charge-transfer resistance (i.e. $\alpha_1 = 0.1$, Figure 4), the one-dimensional model mimics the two-dimensional model quite well. The peak value of Z_{Im} appears to be the same for the two but the real component of the impedance is slightly shifted for the one-dimensional model. At higher values of mass-transfer resistance, (Figures 5 and 6), the absolute difference between the predictions for the two models increases. Whereas the maximum value of Z_{Im} is approximately the same for the two curves in Figure 4, the maximum value for the one-dimensional model is lower as the mass-transfer resistance increases. It may be expected that an increase in the mass-transfer resistance would yield an increase in the capacitive component of the impedance. However the one-dimensional model tends to dampen the effects of mass-transfer resistance by equating the wall concentration of reactant species with the average value at that location. There is a small difference between the values $Z_{Re}(\bar{\omega} \rightarrow \infty)$, however it is not evident at the scale shown in the Figures. Although the curves in Figure 6 do not show the low frequency loop, it is evident that the same trends will apply.

The effect of ohmic resistance on the one-dimensional model is illustrated in Figure 7, which shows a log-log plot of the impedance modulus as a function of frequency. The three pairs of curves in the figure are the results from the two-dimensional model

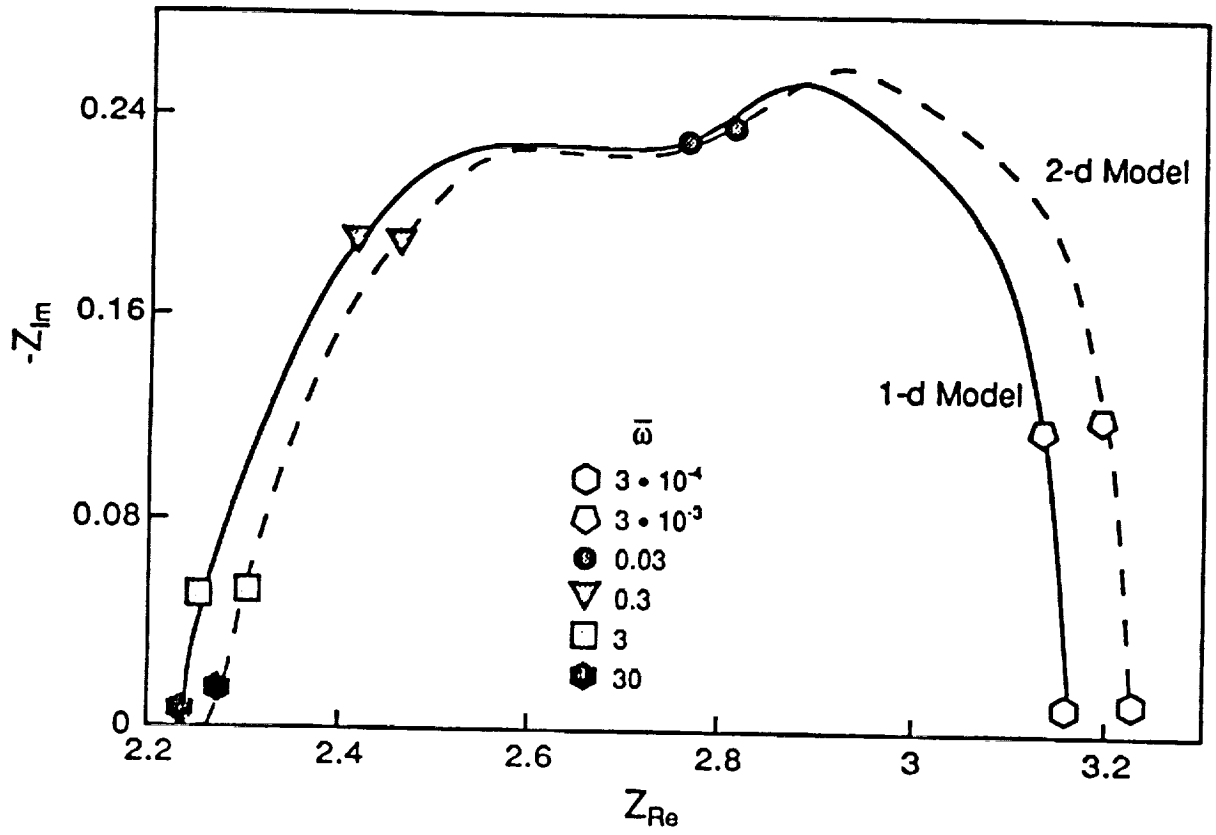

Figure 4: Comparison of the predicted impedance found from the one- and two-dimensional models. ($\alpha_1 = \alpha_4 = 0.1$, $\gamma = 20$).

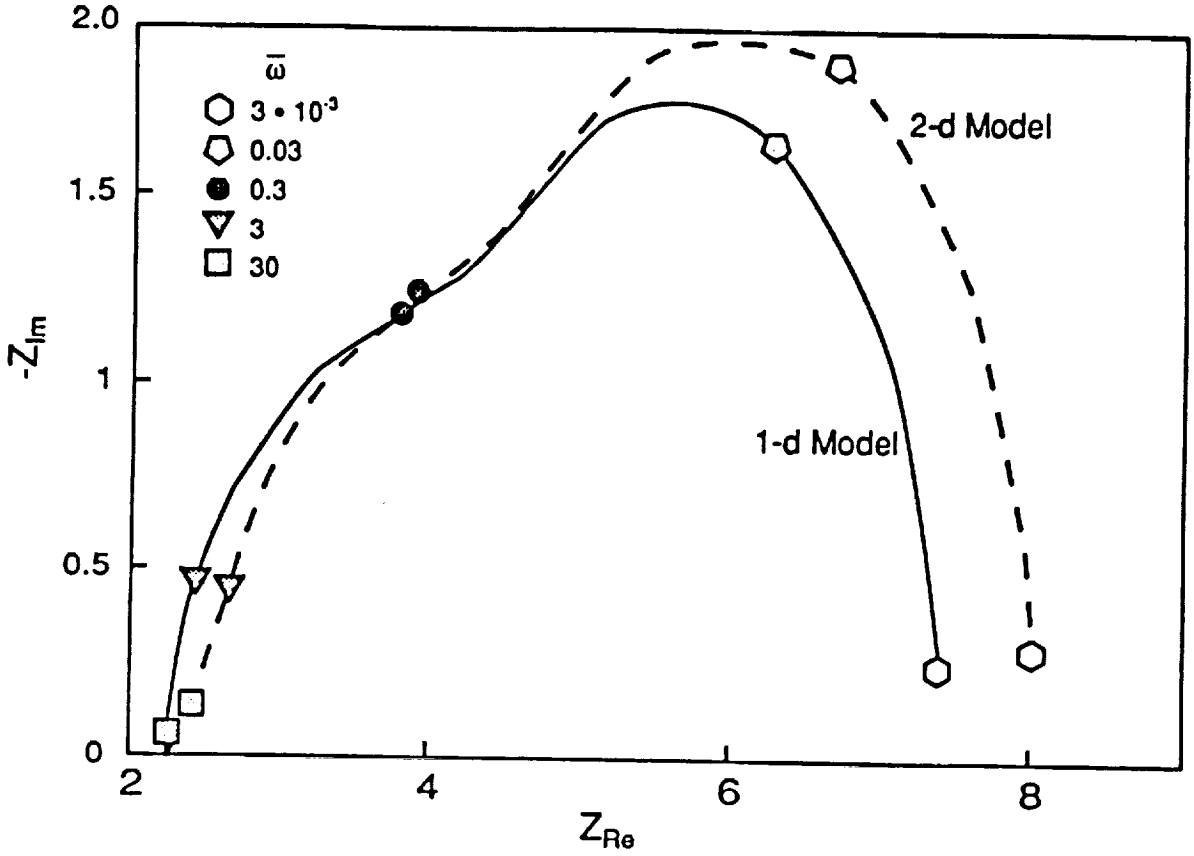

Figure 5: Comparison of the predicted impedance found from the one- and two-dimensional models. ($\alpha_1 = 1$, $\alpha_4 = 0.1$, $\gamma = 20$).

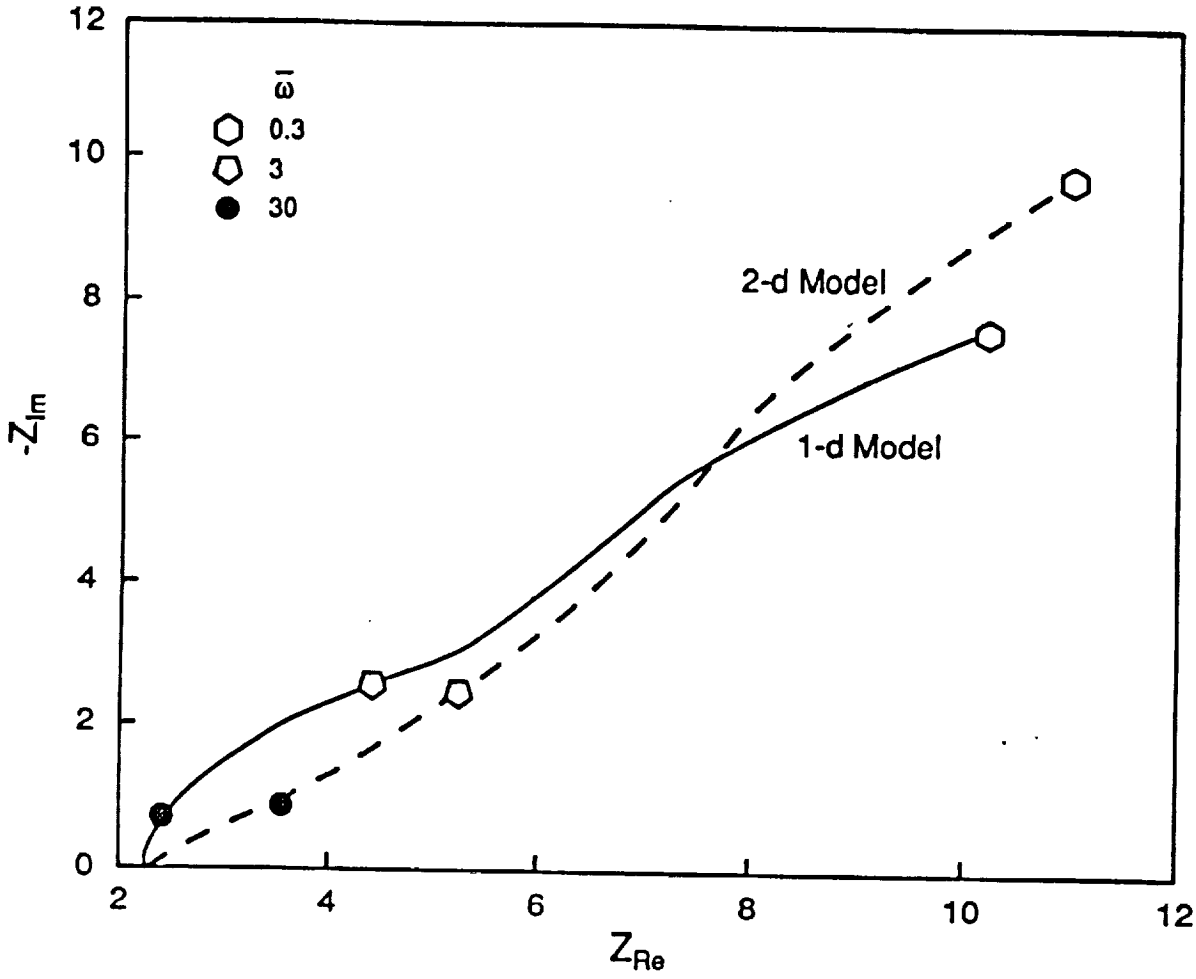

Figure 6: Comparison of the predicted impedance found from the one- and two-dimensional models. ($\alpha_1 = 10$, $\alpha_4 = 0.1$, $\gamma = 20$)

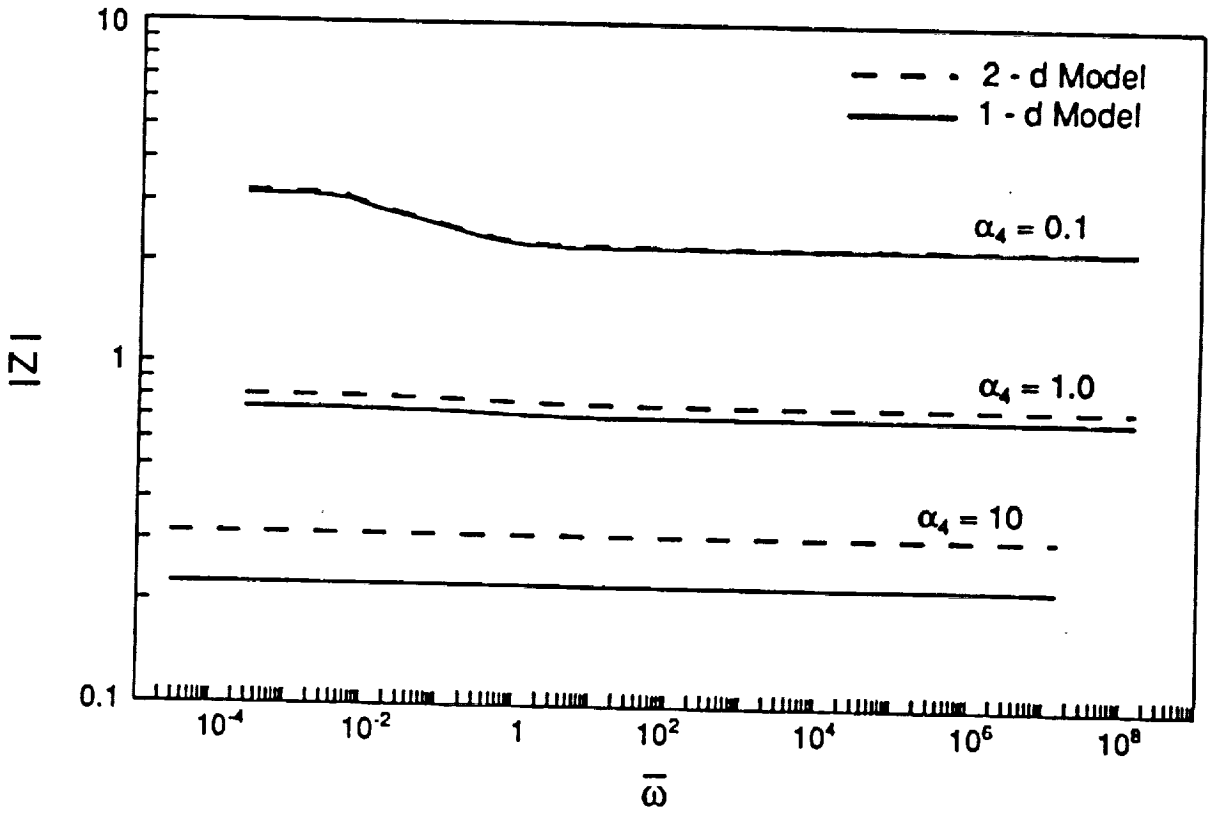

Figure 7: The modulus of the impedance as a function of frequency for 1-d (solid line) and 2-d (dashed line) models. ($\alpha_1 = 0.1$, $\gamma = 20$).

presented in Figure 3 and the corresponding results from the one-dimensional model. As α_4 increases, the modulus decreases and the slope of the modulus-frequency curve goes to zero. The zero slope is a result of the fact that the effective capacitive component of the impedance goes to zero. (The modulus decreasing with increasing α_4 is an artifact of the way in which the impedance is made dimensionless, as discussed in conjunction with Figure 3.) The results shown in the Figure suggest that the one-dimensional model would be a poor choice for analyzing data collected from a system with high ohmic resistance.

In many applications, the dimensionless parameter α_4 will be less than 1 and typically on the order of 0.1 or less. Note, however, that it would be an oversight to ignore the effects of ohmic resistance completely. As an illustration, consider the set of curves shown in Figure 8, which were obtained with the one-dimensional model. At a value of $\alpha_4 = 0.1$, ohmic resistance is low with respect to the charge-transfer resistance. However, decreasing that value by half (i.e. $\alpha_4 = 0.05$) produces a significant shift in both the real and imaginary components of the impedance. A ten-fold decrease in α_4 (from 0.1 to 0.01) increases the maximum value Z_{Im} roughly three-fold. In the limit of very low ohmic resistance, the impedance plot appears quite different from that obtained with what appears to be a "low" value (i.e. $\alpha_4 = 0.1$). Therefore, one should use care in applying models that ignore the ohmic potential drop completely such as that of Keddam *et al.*[6].

Since both the one- and two-dimensional models account for axial gradients in a finite pore, it is intuitive that the agreement between the two models would not be

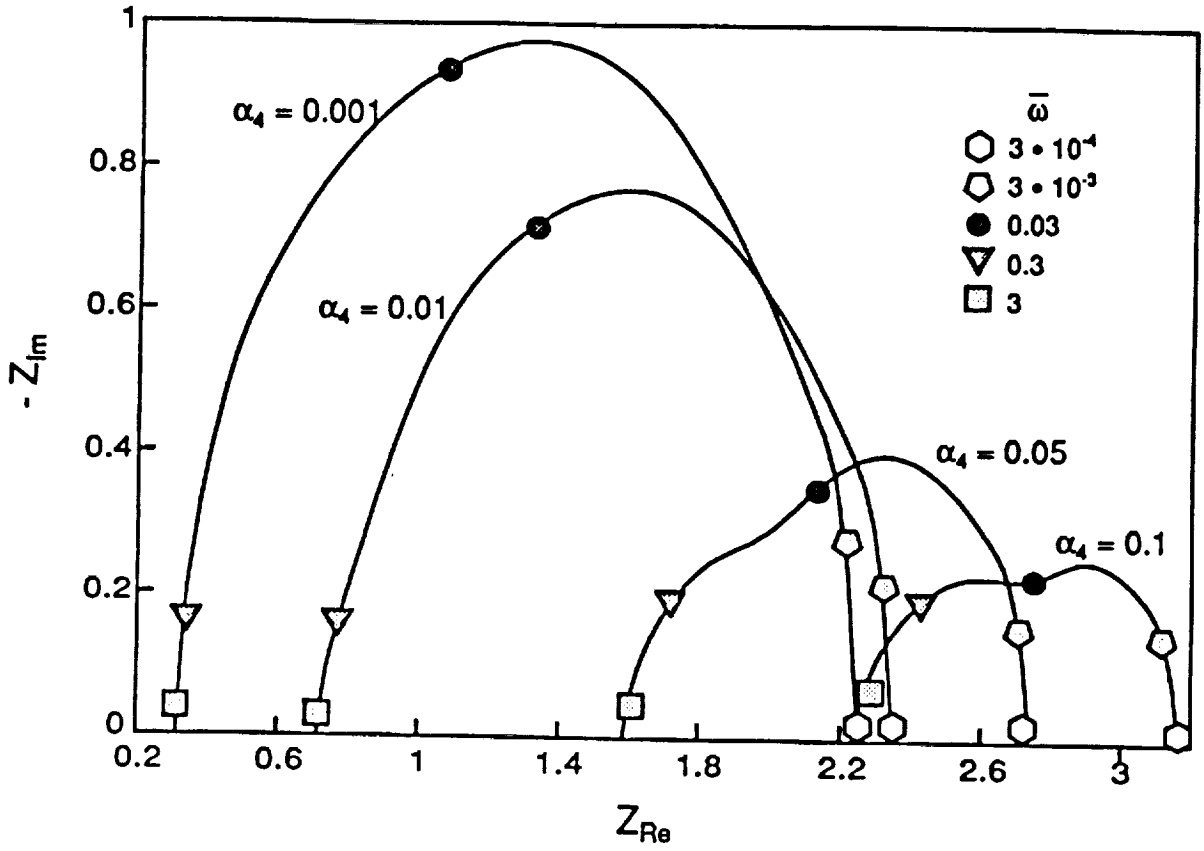

Figure 8: The variation of impedance with ohmic resistance for decreasing α_4 (computed with the 1-d model) ($\alpha_1 = 0.1$, $\gamma = 20$).

affected by the aspect ratio and is not discussed further here.

4.2.2 Applicable Parameter Range of the One-Dimensional Model

The results presented above show that the assumption of radially-averaged concentrations and potentials can be a serious limitation to the one-dimensional model. The problem arises when mass-transfer resistance is high, and concentration gradients extend far from the wall of the tube. Likewise for the relation between ohmic resistance and the radial gradient of the potential. Consequently, a radially-averaged quantity can be significantly different from the actual value at the wall, with the result that the current predicted from averaged quantities will differ from that predicted from the two-dimensional model.

The problem of radial averaging will be most significant at very low frequencies and/or when diffusion and ohmic resistances are large with respect to charge-transfer resistance. Based on the results of the parameter study it appears that, over the frequency range where double-layer charging is not important, the one-dimensional model is an adequate approximation to the two-dimensional model when ohmic resistance is low ($\alpha_4 \leq 0.1$) and mass-transfer resistance is low-to-moderate with respect to charge-transfer resistance ($\alpha_1 \leq 1$).

4.3 Assessment of the Double-Layer Effects

The most significant limitation of the two-dimensional model for the impedance calculation is the omission of double-layer capacitance; however, the one-dimensional model does incorporate it and a comparison of the two will indicate when the omission adversely affects the results of the two-dimensional model. As described in the preceding sections, the one-dimensional model is not without limitations. Nevertheless, for cases where mass-transfer and ohmic resistances are small relative to the charge-transfer resistance (e.g. when $\alpha_1 = \alpha_4 = 0.1$), the one-dimensional model is an adequate approximation to the two-dimensional model. Therefore, conclusions based on the behavior of the one-dimensional model in these parameter ranges will be applicable to the two-dimensional model.

The effect of double-layer charging as predicted by the one-dimensional model is illustrated in Figure 9. The dashed line in the Figure shows the results computed with the two-dimensional model and the solid line was obtained with the one-dimensional model, including double-layer effects. For the results shown here, the ratio of diffusion to double-layer charging characteristic times is $\lambda = 2.27 \times 10^6$. The two semi-circular curves obtained in the frequency range $\bar{\omega} = 3 \times 10^{-4}$ to 30 are identical to the diffusion loops shown in Figure 4. The large loop at higher frequencies ($\bar{\omega} \geq 3 \times 10^4$) is a result of the interaction of double-layer charging with charge-transfer kinetics.

The significance of these results can be seen more easily in Figure 10, which

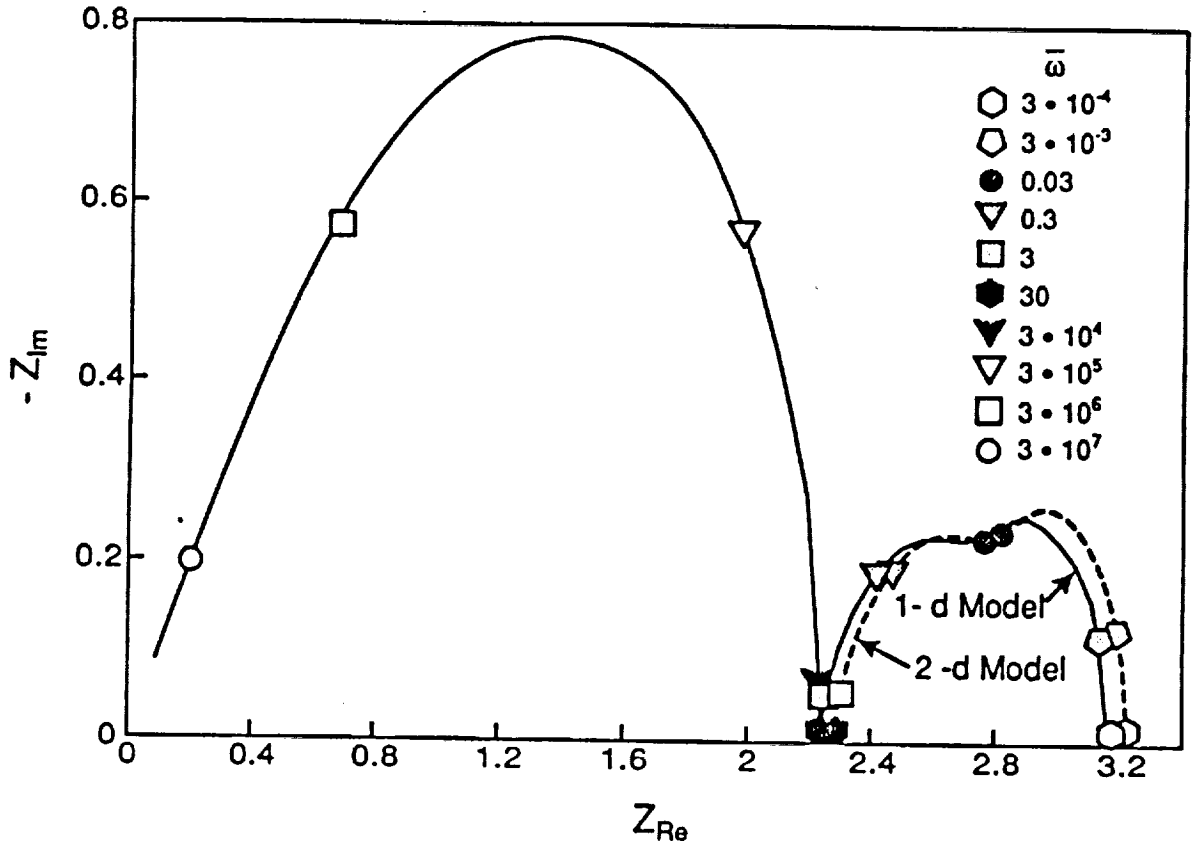

Figure 9: A comparison of the impedance calculated from the two-dimensional model (dashed line) with the one-dimensional model including double-layer charging (solid line); ($\alpha_1 = \alpha_4 = 0.1$, $\gamma = 20$, $\lambda = 2.27 \times 10^6$).

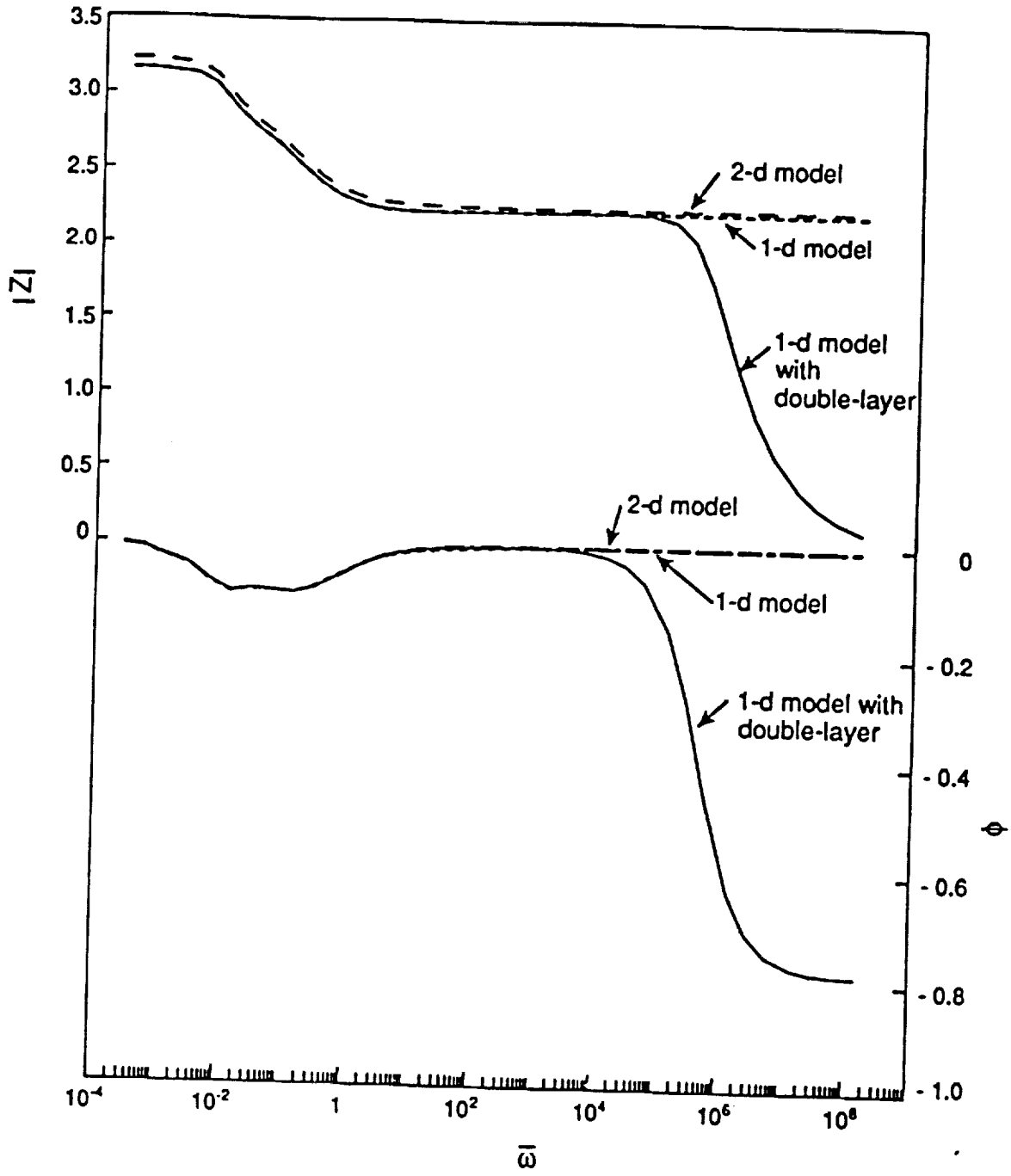

Figure 10: A Bode plot comparing the two-dimensional model with the one-dimensional models (with and without double-layer charging). $\alpha_1 = \alpha_4 = 0.1$, $\gamma = 20$, $\lambda = 2.27 \times 10^6$.

shows the modulus of the impedance ($|Z|$) and phase lag (ϕ) as a function of frequency for the one-dimensional model with and without double-layer charging as well as the two-dimensional model. There are two points to be made from these results. First, in the low frequency range ($\bar{\omega} \leq 10^4$), the one-dimensional model *with* double-layer charging is identical to the one-dimensional model *without* it. The overlap of the results from the one-dimensional models is quite evident. The agreement between the two models in the low frequency range leads to the conclusion that the omission of double-layer charging does not introduce any error into the prediction of the diffusion loop in the impedance diagram. By analogy, we can conclude that the results presented for the two-dimensional model are also correct as presented.

The second important result shown in the Figure is that it clearly illustrates the wide frequency separation of the diffusion and double-layer loops that appear in Figure 9. The diffusion effect is confined entirely in the frequency range below $\bar{\omega} = 100$. That is, at frequencies above $\bar{\omega} = 100$ mass-transfer resistance becomes insignificant in the vicinity of the pore wall. Conversely, the double-layer charging effect is not significant below frequencies of $\bar{\omega} = 10^4$. Thus, for the case considered here, diffusion and double-layer charging are independent effects which can be considered separately. The fact that the two curves do not interact with each other arises from the large difference in the characteristic time scales of the phenomena involved. Diffusion, a relatively slow process, is important at low frequencies and insignificant at high frequencies. Conversely, double-layer charging,

which is a relatively fast process, can only be detected at high frequencies.

The frequency separation between the two loops in the impedance diagram is solely a function of the parameter λ and is not affected by the parameters α_1 and α_4. Changing the values of α_1 and α_4 have the effect of shifting the curves in the Bode plot horizontally and vertically, but the shape of the curve is not affected. Consequently, the parameter λ can be used to judge whether or not the omission of double-layer charging introduces errors into the impedances predicted by the two-dimensional model. Results of a numerical study show that the frequency separation between the two loops will be at least one order of magnitude as long as $\lambda \geq 3000$. That is, given $\lambda \geq 3000$, then the double-layer charging loop will not become evident until a frequency that is 10 times greater than the frequency at which the diffusion loop disappears.

5 Summary

A tube-analog model of a pore was used to develop the two-dimensional, time-dependent concentration and potential profiles in the pore. Impedance results were computed by application of appropriate boundary conditions to the solution obtained for the general problem. A comparison of the two-dimensional model with a one-dimensional model based on the same assumptions shows that the one-dimensional model is a poor approximation when mass-transfer and/or ohmic resistance are dominant. In addition, it was found that omitting ohmic resistance altogether can introduce errors in the computed impedance.

Although the model presented above omits double-layer charging, no significant errors are introduced into the mass-transfer capacitance loop.

Acknowledgments

This research was supported by NASA grant NAG 3-649 and, in part, by a Professional Development Award to ASV from the Research Triangle Institute.

6 APPENDIX

The coefficients $a_n(\bar{t})$ and $b_n(\bar{t})$ can be determined by substituting the linearized current and flux (Eqns 9 and 10) and the assumed expressions for θ_w and η_w (Eqns 15 and 16) into Equations 5 and 7. When the resulting equations are multiplied by $\sin\beta_n Z_o$ and the orthogonality property of the sinusoidal eigenfunctions is applied, an integral equation is obtained for $b_n(\bar{t})$, and $a_n(\bar{t})$ is algebraically related to $b_n(\bar{t})$.

$$b_n(\bar{t}) = -\frac{4}{\gamma}\int_0^{\bar{t}}\left[\frac{1}{\beta_n}\left(\mathcal{J}^o + \alpha_2\eta^o(\tau)\right) + \frac{\gamma}{2}\left(\alpha_1 b_n(\tau) + \alpha_2 a_n(\tau)\right)\right] \times e^{-\beta_n^2(\bar{t}-\tau)} \times \left[1 + \sum_{j=1}^{\infty} e^{-\delta_j^2(\bar{t}-\tau)}\right] d\tau \tag{43}$$

$$a_n(\bar{t}) = \frac{-2}{\gamma(\alpha_4+\sigma_n)}\left[\frac{\mathcal{I}^o}{\beta_n} + \frac{\alpha_3\gamma}{2}b_n(\bar{t}) + \frac{\alpha_4}{\beta_n}\eta^o(\bar{t}) + \frac{\alpha_4\gamma}{2}a_n(\bar{t})\right] \tag{44}$$

where $\sigma_n = \beta_n I_1(\beta_n)/I_0(\beta_n)$. The solutions to Equations 43 and 44 are obtainable by Laplace transform. In Laplace domain Equations 43 and 44 are expressed as

$$\begin{aligned}\bar{b}_n(s) &= -\frac{4}{\gamma}\left[\frac{1}{\beta_n}\left(\frac{\mathcal{J}^o}{s}+\alpha_2\bar{\eta}^o\right)+\frac{\gamma}{2}\left(\alpha_1\bar{b}_n+\alpha_2\bar{a}_n\right)\right] \\ &\quad\times\left(\frac{1}{s+\beta_n^2}+\sum_{j=1}^{\infty}\frac{1}{s+\beta_n^2+\delta_j^2}\right) \qquad (45)\end{aligned}$$

$$\bar{a}_n = \frac{-2}{\gamma(\sigma_n+\alpha_4)}\left[\frac{\mathcal{I}^o}{s\beta_n}+\frac{\alpha_3\gamma}{2}\bar{b}_n(s)+\frac{\alpha_4\bar{\eta}^o(s)}{\beta_n}\right] \qquad (46)$$

Equations 45 and 46 can be manipulated to yield explicit expressions for $\bar{b}_n$ based only on the Laplace variable s and the physical parameters of the system; however, reinversion of that expression would yield an integral that could only be evaluated numerically. A more useful approach is to invoke the identity relation

$$\frac{1}{x^2}+\sum_{j=1}^{\infty}\frac{1}{x^2+\delta_j^2}=\frac{1}{2}\frac{I_0(x)}{xI_1(x)} \qquad (47)$$

This identity was derived by comparing the concentration profile obtained from the steady-state formulation of the governing equations with that obtained by considering the long-time response of Equation 5 to a step-change in the mass flux at the wall of the tube. The two expressions must be identical which results in equation 47. The identity relationship has been verified numerically [1]. After substitution of Equation 47 into Equation 45 and rearrangement, the resulting expression for $\bar{b}_n(s)$ is

$$\begin{aligned}\bar{b}_n(s) &= -\frac{2}{\gamma}\left[\left(\frac{1}{\beta_n}(\mathcal{J}^o+\alpha_2\bar{\eta}^o s)+\frac{\gamma\alpha_2\bar{a}_n s}{2}\right)I_0(\sqrt{s+\beta_n^2})\right] \\ &\quad\times\left[s\sqrt{s+\beta_n^2}\,I_1(\sqrt{s+\beta_n^2})+\alpha_1 s I_0(\sqrt{s+\beta_n^2})\right]^{-1} \qquad (48)\end{aligned}$$

Substitution of Equation 46 into Equation 48 and rearranging leads to

$$\bar{b}_n(s) = \frac{N_1(s) + \bar{\eta}^o N_2(s)}{D(s)} \tag{49}$$

where

$$N_1(s) \equiv -\frac{2}{\gamma\beta_n}\left[\mathcal{J}^o - \frac{\alpha_2}{\alpha_4+\sigma_n}\mathcal{I}^o\right] I_0(\sqrt{s+\beta_n^2}) \tag{50}$$

$$N_2(s) \equiv -\frac{2\alpha_2 s}{\gamma\beta_n}\left(1 - \frac{\alpha_4}{\alpha_4+\sigma_n}\right) I_0(\sqrt{s+\beta_n^2}) \tag{51}$$

$$D(s) \equiv s\left[\sqrt{s+\beta_n^2}\, I_1(\sqrt{s+\beta_n^2}) + \alpha_1\left(1 - \frac{\alpha_4}{\alpha_4+\sigma_n}\right) I_0(\sqrt{s+\beta_n^2})\right] \tag{52}$$

Equation 49 can be inverted according to the formula

$$b_n(\bar{t}) = \mathcal{L}^{-1}\left[\frac{N(s)}{D(s)}\right] = \sum_{k=1}^{\infty} \frac{N(s_{kn})}{D'(s_{kn})} \exp(s_{kn}\bar{t})$$

where $D'(s)$ is the derivative of the function D with respect to s

$$\begin{aligned} D'(s) &= \left[\sqrt{s+\beta_n^2} + \frac{s}{2\sqrt{s+\beta_n^2}}\alpha_1\left(1 - \frac{\alpha_4}{\alpha_4+\sigma_n}\right)\right] I_1(\sqrt{s+\beta_n^2}) \\ &+ \left[\alpha_1\left(1 - \frac{\alpha_4}{\alpha_4+\sigma_n}\right) + \frac{s}{2}\right] I_0(\sqrt{s+\beta_n^2}) \end{aligned} \tag{53}$$

and s_{kn} are the roots $D(s_{kn}) = 0$. The inverted expression for $b_n(\bar{t})$ is:

$$b_n(\bar{t}) = \sum_{k=1}^{\infty} \frac{N_1(s_{kn})}{D'(s_{kn})} e^{s_{kn}\bar{t}} + \int_0^{\bar{t}} \eta^o(\bar{t}-\tau) \sum_{k=1}^{\infty} \frac{N_2(s_{kn})}{D'(s_{kn})} e^{s_{kn}\tau}\, d\tau \tag{54}$$

where the convolution integral has been applied to the second term in the numerator of Equation 49. An important point to note about this expression is that it is independent

of the form of the imposed potential function $\eta^o(\bar{t})$. The only restriction is that the perturbation must be small so that the assumption of linearity in the kinetic equation applies.

When a sinusoidal potential function with amplitude η_c^o is inserted into Equation 54, integrated, and transients are eliminated by taking the limit as $\bar{t} \to \infty$, then

$$b_n(\bar{t}) = \sum_{k=1}^{\infty} \frac{N_2(s_{kn})}{D'(s_{kn})} \left[\frac{-\eta_{ss}}{s_{kn}} + \frac{\eta_c^o}{\bar{\omega}^2 + s_{kn}^2} (\bar{\omega} \sin \bar{\omega}\bar{t} - s_{kn} \cos \bar{\omega}\bar{t}) \right] \tag{55}$$

The long-time limit of $a_n(\bar{t})$ is obtained by substituting the definition of $b_n(\bar{t})$ into Equation 44 and rearranging:

$$\begin{aligned} a_n(\bar{t}) \;=\; & -\frac{2}{\gamma(\alpha_4 + \sigma_n)} \left[\frac{\mathcal{I}^o}{\beta_n} + \frac{\alpha_4}{\beta_n} \eta_{ss} - \frac{\alpha_3 \gamma}{2} \eta_{ss} \sum_{k=1}^{\infty} \frac{N_2(s_{kn})}{D'(s_{kn})} \frac{1}{s_{kn}} \right. \\ & + \sin \bar{\omega}\bar{t} \left(\frac{\alpha_3 \gamma \bar{\omega} \eta_c^o}{2} \sum_{k=1}^{\infty} \frac{N_2(s_{kn})}{D'(s_{kn})} \frac{1}{\bar{\omega}^2 + s_{kn}^2} \right) \\ & \left. + \cos \bar{\omega}\bar{t} \left(\frac{\alpha_4}{\beta_n} \eta_c^o - \frac{\alpha_3 \gamma}{2} \eta_c^o \sum_{k=1}^{\infty} \frac{N_2(s_{kn})}{D'(s_{kn})} \frac{s_{kn}}{\bar{\omega}^2 + s_{kn}^2} \right) \right] \end{aligned} \tag{56}$$

In summary, Equations 55 and 56 can be substituted into Equations 15 and 16 to obtain the stationary-state concentration and overpotential profiles for a reaction occurring in response to a small amplitude, sinusoidally oscillating potential at the inlet of a cylindrical tube.

It can be shown [1] that all s_{kn} are real, negative, and infinite in number and were found by using standard root-finding methods [14] for low-order roots and an

asymptotic expansion for larger roots. Thus, computing the impedance consists of finding the roots of the function $D(s_{kn})$ defined in Equation 52 and then calculating the infinite sums for use in finding values of $\mathcal{A}$ and $\mathcal{B}$ (Equations 21 and 22). Once these values are known, Z_{Re} and Z_{Im} can be computed directly.

Nomenclature

C_{dl}	double-layer capacitance (F/cm^2)
C_i	concentration of species i ($mole/cm^3$)
C_i^o	concentration of species i in bulk solution ($mole/cm^3$)
C_O	concentration of reactant O ($mole/cm^3$)
C_R	concentration of product R ($mole/cm^3$)
d	pore diameter (cm)
$\mathcal{D}$	diffusivity (cm^2/s)
f	frequency (Hz)
F	Faraday's constant
$\mathcal{I}$	dimensionless reaction current at the pore wall; $\frac{F}{RT}\frac{d/2}{\kappa}i_n(z,t)$
$\mathcal{I}_{1d}$	dimensionless reaction current for 1-d model, eqn. 41
$i_n(z,t)$	current density at the pore wall (A/cm^2)
i_o	exchange current density (A/cm^2)
$\mathcal{I}_T$	dimensionless total current, eqn. 17
$\mathcal{I}_{ss}$	dimensionless steady-state current
j	$\sqrt{-1}$
$\mathcal{J}$	dimensionless mass flux at the pore wall; $\frac{d/2}{\mathcal{D}C_O^o}j(z,t)$
$\mathcal{J}_{ss}$	dimensionless steady-state mass flux
$j(z,t)$	mass flux at the pore wall ($mole/cm^2s$)
L	length of pore (cm)
r	distance in radial direction (cm)
R	dimensionless radial distance; $r/(d/2)$
R	ideal gas constant ($J/(mole \cdot K)$)
t	time (s)
T	temperature (K)
$\bar{t}$	dimensionless time (on diffusion time scale); t/t_D
$\hat{t}$	dimensionless time (on capacitance time scale); t/t_{dl}
t_D	characteristic diffusion time; $(d/2)^2/\mathcal{D}$
t_{dl}	characteristic double-layer charging time; $C_{dl}(d/2)/\kappa$
z	distance in axial direction (cm)
Z	dimensionless axial distance; $z/(d/2)$
Z	dimensionless impedance eqn. 26
$\|Z\|$	impedance modulus, eqn. 28
Z_{Im}	Dimensionless imaginary component of impedance, eqn. 27
Z_{Re}	Dimensionless real component of impedance, eqn. 27

GREEK

α_A	anodic transfer coefficient
α_C	cathodic transfer coefficient
β_n	eigenvalues of PDE, $(n-\frac{1}{2})\pi/\gamma$
γ	pore aspect ratio; $L/(d/2)$
Γ_1	$\frac{nF^2\mathcal{D}C_O^o}{\kappa RT}$
Γ_2	$\frac{(d/2)i_o}{C_O^o\mathcal{D}nF}$
δ_j	zeroes of the Bessel function $J_1(u)$
η	dimensionless overpotential; $\frac{nF}{RT}(\Phi_1-\Phi_2)$
η_c^o	amplitude of imposed overpotential function
η_{ss}	steady-state overpotential
η_w	dimensionless overpotential at the pore wall, eqn. 7
θ	dimensionless concentration; $\frac{C-C^o}{C^o}$
θ_{ss}	steady-state concentration
θ_w	dimensionless concentration at the pore wall, eqn. 5
κ	solution conductivity ($\Omega^{-1}\text{cm}^{-1}$)
λ	ratio of the diffusion time scale to the double-layer charging time scale, eqn. 32
σ_n	$\beta_n I_1(\beta_n)/I_0(\beta_n)$
Φ_1	solid potential (V)
Φ_2	solution potential (V)
ω	angular frequency of imposed overpotential function (s^{-1})
$\bar{\omega}$	dimensionless frequency, eqn. 29

References

[1] Viner, A.S., A Model of Steady-State and Impedance Measurements in Flooded Porous Electrodes. MS Thesis, North Carolina State University, Raleigh, NC, 1988.

[2] Winsel, A. "Beitrage zur Kenntnis der Stromverteilung in porosen Elektroden," *Z. Elektrochem.*, **66**, 287-304 (1962). Translated by J. Newman, February, 1973. Available as Document No. UCRL-Trans-1495 from the National Technical Information Service, U.S. Department of Commerce, Front Royal, Virginia.

[3] Darby, R., "Faradaic Impedance of Polarized Porous Electrodes I. First Order Kinetics," *J. Electrochem. Soc.* **113**, 392-396 (1966).

[4] Darby, R., "Faradaic Impedance of Polarized Porous Electrodes II. Non-linear Kinetics," *J. Electrochem. Soc.* **113**, 496-500 (1966).

[5] de Levie, R., "Electrochemical Response of Porous and Rough Electrodes," in: **Adv. in Electrochem. and Electrochem. Eng.**, P. Delahay and C.W. Tobias (eds.), **6**, 329-397, (1967)

[6] Keddam, M., C. Rakotomovo, and H. Takenouti, "Impedance Of A Porous Electrode With An Axial Gradient Of Concentration," *J. Appl. Electrochem.*, **14**, 437-448, 1984.

[7] Rangarajan, S.K., "Theory of Flooded Porous Electrodes. I. Galavanostatic Transients and Generalized Impedance," *J. Electroanal. Chem.* **22**, 89-104 (1969).

[8] Keiser, H. K.D. Beccu, and M.A. Gutjahr, "Abschatzung der Porenstruktur Poroser Elektroden Aus Impedanzmessungen," *Electrochim. Acta*, **21**, 539-543 (1976).

[9] Cachet, C. and R. Wiart, "Coupled Axial Gradients of Potential and Concentration in a Cylindrical Pore Electrode: An Impedance Model," *J. Electroanal. Chem.*, **195**, 21-37 (1985).

[10] Grens, E.A., II, and C.W. Tobias, "Analysis of the Dynamic Behavior of Flooded Porous Electrodes," *Ber. Bunsenges. Phys. Chem.*, **68**, 236-249 (1964).

[11] Grens, E.A., II, and C.W. Tobias, "The Influence of Electrode Reaction Kinetics on the Polarization of Flooded Porous Electrodes," *Electrochim. Acta*, **10**, 761-772 (1965).

[12] Grens, E.A., "On the Assumptions Underlying Theoretical Models for Flooded Porous Electrodes," *Electrochim. Acta*, **15**, 1047-1057, 1970.

[13] Bond, A.M., et al. "A Comparison of the Chronoamperometric Response at Inlaid and Recessed Disc Microelectrodes," *J. Electroanal. Chem.*, **249**, 1-14, 1988.

[14] IMSL, The International Mathematical and Statistical Library (Version 9.2), 2500 ParkWest Tower 1, 2500 CityWest Blvd., Houston, TX, 77042, 1984.

SECTION 4

REVERSIBLE, LINEAR-SWEEP VOLTAMMETRY OF A SOLUBLE REDOX COUPLE: EFFECT OF INITIAL CONCENTRATIONS

by

John W. Weidner and Peter S. Fedkiw
Department of Chemical Engineering
North Carolina State University
Raleigh, NC 27695-7905

Published in

Analytical Chemistry, **62**, 875, 1990

ABSTRACT

Reported are the theoretically predicted peak potentials and currents for the cathodic scan of a reversible redox couple over a range of the initial concentration ratio of oxidized-to-reduced species from zero to infinity. The asymptotic limit for the voltammogram as the initial concentration ratio approaches zero, along with the infinity limit given by classical theory, is used to develop empirical relationships which correlate the peak potential and current to the initial concentration ratio. Dimensionless peak values measured experimentally for different initial concentration ratios of the ferro/ferricyanide redox couple are found to agree with those theoretically predicted.

Introduction

Classical theoretical formulas are available to predict the peak current and potential at a planar electrode during linear-sweep voltammetry (LSV) for the reversible (Nernstian) reaction

$$O + ne^- \rightleftharpoons R \tag{1}$$

where O and R are soluble oxidized and reduced species, respectively, and n is the number of electrons transferred [1,2]. Matsuda and Ayabe [1] and Nicholson and Shain [2] showed that if the reduced species is present initially in negligible amounts and the voltage is swept in the negative direction, the cathodic peak current is proportional to the absolute value of the sweep rate to the one-half power and the corresponding peak potential is sweep-rate independent. Matsuda and Ayabe [1] also demonstrated that if the sweep begins at the equilibrium potential, E_{eq}, the dimensionless peak current and potential depend only upon the product of two dimensionless ratios, $\gamma\theta^*$: the ratio of the square root of the diffusion coefficients of O and R, $\gamma \equiv \sqrt{\mathcal{D}_O/\mathcal{D}_R}$, and the initial concentration ratio of O and R in the bulk electrolyte, $\theta^* \equiv (C_O^*/C_R^*)$. Matsuda and Ayabe [1] presented calculations for the case where $\gamma\theta^* \rightarrow \infty$. Left numerically unexamined was the influence of R when its concentration is not negligibly small. Farsang *et al.* [3], using the same formula as derived by Matsuda and Ayabe [1], examined the influence of $\gamma\theta^*$ on the peak values over the narrow range of $0.22 \leq \gamma\theta^* \leq 5.5$ and found a shift in the potential to more negative values and an increase in the dimensionless peak current as $\gamma\theta^*$ decreased.

Nicholson and Shain [2] considered the case of starting the sweep at a non-equilibrium potential, E_i, in the limit of the reduced species concentration equal to zero ($\theta^* = \infty$). They obtained a current-potential relationship which is a function of an analogous dimensionless grouping, $\gamma\theta$, where γ is the same as defined above, and θ is the concentration ratio at the *electrode surface* given by the Nernst equation immediately *after* E_i is applied. This non-equilibrium initial condition gives rise to a Cottrell current in the early portion of the sweep which they showed does not significantly affect the peak current or potential as long as $\gamma\theta > 650$. This corresponds to starting the sweep at a potential which is at least $200/n$ mV ($T = 25°C$) positive of the peak potential.

In what follows, the Matsuda and Ayabe [1] equation is applied to calculate the peak potential and current over the range of $\gamma\theta^*$ from zero to infinity. Also presented is an explicit heretofore unrecognized formula for the peak values in the limit of $\gamma\theta^* \rightarrow 0$. The peak values at the two limiting behaviors are used to deduce and develop an easy-to-apply empirical relationship which correlates the results as a function of $\gamma\theta^*$ over the entire range. The calculations are confirmed by experimental measurements. The effect of mistakingly applying the Nicholson and Shain [2] formula for regions of $\gamma\theta^*$ below its range of validity is also quantified.

Peak Current and Potential Calculations

Matsuda and Ayabe [1] solved the one-dimensional transient diffusion equation for both soluble redox species, and obtained the time-dependent surface concentrations for O

and R in terms of the reaction current. Starting the sweep at the equilibrium potential, θ^* is related to E_{eq} by

$$\theta^* = \exp\left[\left(\frac{nF}{RT}\right)(E_{eq} - E^{o'})\right] \tag{2}$$

where $E^{o'}$ is the formal potential. For the case of reversible kinetics, substituting equation 2, the surface concentrations and the sweep rate, v, into the Nernst equation results in the integral equation for the current

$$\int_0^{at} \frac{\chi(z)dz}{\sqrt{at - z}} = \frac{1 - \exp(-at)}{1 + \gamma\theta^* \exp(-at)} \equiv L(at) \tag{3}$$

where t is time, $a \equiv \left(\frac{nF}{RT}\right)v$ which is positive for a cathodic sweep, and $\chi(at)$ is the dimensionless current defined as

$$\sqrt{\pi}\chi(at) \equiv \frac{i(at)}{nFAC_O^*(\mathcal{D}_O a)^{1/2}} \tag{4}$$

where F is Faraday's constant, A is the electrode area, and $i(at)$ is the time-dependent reaction current which is positive for a cathodic reaction. The product (at) is the displacement of the dimensionless potential from the starting potential.

Equation 3 differs from the analogous formula given by Nicholson and Shain (equation 22 of [2]) in that by their assumption of C_R^* is equal to zero, the numerator of $L(at)$ is equal to one, and θ^* is replaced by θ where θ is given by

$$\theta = \exp\left[\left(\frac{nF}{RT}\right)(E_i - E^{o'})\right] \tag{5}$$

Equation 3 is an Abel integral equation [5] for $\chi(at)$ with the solution

$$\sqrt{\pi}\chi(at) = \frac{(1+1/\gamma\theta^*)}{4\sqrt{\pi}} \int_0^{at} \frac{dz}{\sqrt{at-z}\cosh^2(\frac{\ln\gamma\theta^*-z}{2})} \tag{6}$$

The analogous current-potential relationship derived by Nicholson and Shain (equation 33 of [2]) from the solution of equation 3 with a unity numerator for $L(at)$ and θ replaced by θ^* is

$$\sqrt{\pi}\chi(at) = \frac{1}{\sqrt{\pi(at)}(1+\gamma\theta)} + \frac{1}{4\sqrt{\pi}} \int_0^{at} \frac{dz}{\sqrt{at-z}\cosh^2\left(\frac{\ln\gamma\theta-z}{2}\right)} \tag{7}$$

(For the calculations presented here, the integrals in equations 6 and 7 were numerically evaluated using the IMSL [6] quadrature subroutine DQDAGS which accommodates integrands having end-point singularities.)

Although equation 6 as $\gamma\theta^* \rightarrow \infty$ is identical to the $\gamma\theta \rightarrow \infty$ limit of equation 7, θ^* and θ are not interchangeable. The leading term in equation 7 is a result of assuming the initial concentration of the reduced species is zero, and predicts a Cottrell current upon application of E_i at the start of the sweep. This term can be significant when $\gamma\theta$ is not large. To illustrate this point, the effect on the voltammogram of erroneously replacing θ with θ^* in equation 7 is shown in Figure 1 with the potentials plotted relative to the half-wave potential, $E_{1/2} \equiv E^o + \left(\frac{RT}{nF}\right)\ln\gamma$ [2]. At $\gamma\theta^* = 20$, the dimensionless peak current and potential predicted from equation 6 both differ from those found using equation 7 (with θ set equal to θ^*) by 2%, and at $\gamma\theta^* = 2$, the percentage difference is 6% and 33%, respectively.

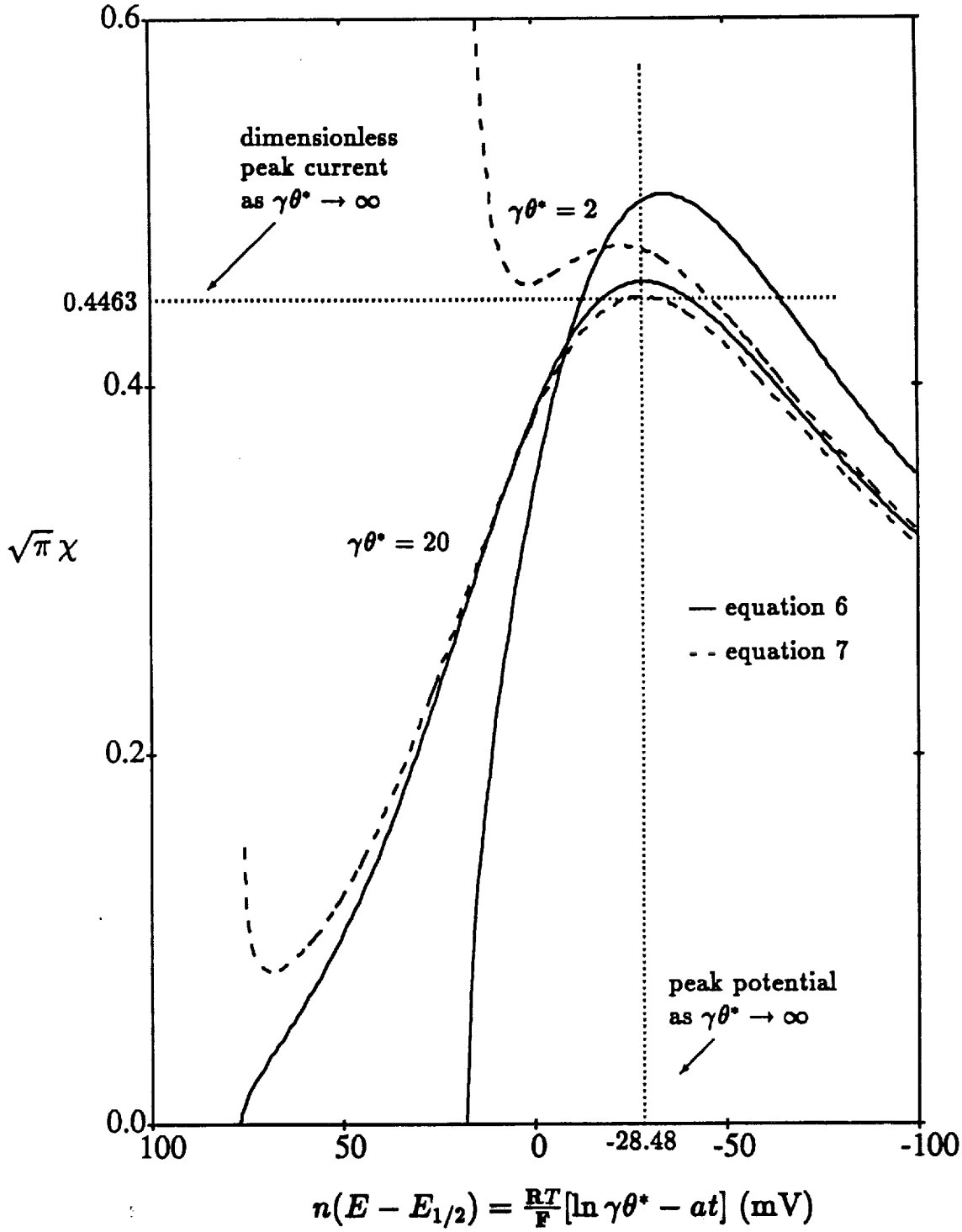

Figure 1: Predicted linear-sweep voltammograms from a planar electrode. The solid lines are the voltammograms generated from equation 6. The dashed lines are voltammograms generated from equation 7 with θ replaced by θ^*. The potentials, in mV, are for $T = 298$ K.

The dimensionless peak current and potential may be determined as a function of $\gamma\theta^*$ by calculating the voltammogram using equation 6 to locate graphically the peak position. However, a more convenient analytical procedure was derived by differentiating equation 6 with respect to (at) and setting the result equal to zero. The potential which satisfies the resulting expression is the peak potential which, when substituted into equation 6, specifies the peak current. Newton's method was used to solve the resulting non-linear equation for the peak potential generated from this procedure. The same technique was applied to equation 7 (with θ replaced by θ^*) and the resulting dimensionless peak currents and potentials from the two predictions are compared in Figure 2 as a function of $\gamma\theta^*$. The dimensionless peak potential, E_p^*, is defined as

$$E_p^* \equiv [(at)_p - \ln \gamma\theta^*] \tag{8}$$

where $(at)_p$ is the dimensionless peak potential relative to the equilibrium potential.

Nicholson and Shain [2] report their results at $\gamma\theta = 650$, and Matsuda and Ayabe report theirs at $\gamma\theta^* = 165,000$, and from Figure 2 we see that θ and θ^* are interchangeable at these values; that is, no difference is found in the predicted peak values regardless whether equation 6 or 7 is used. Replacing θ^* with θ at smaller values of θ^*, however, will lead to differing results. Further, for values of $\gamma\theta^* \leq 1.60$, equation 7 does not predict a peak current because the Cottrell current dominates the transient response.

The dimensionless peak values ($\sqrt{\pi}\chi_p = 0.4463$ and $E_p^* = 1.109$) given by Matsuda and Ayabe [1] and Nicholson and Shain [2] are the limiting values as $\gamma\theta^* \rightarrow \infty$. Limiting

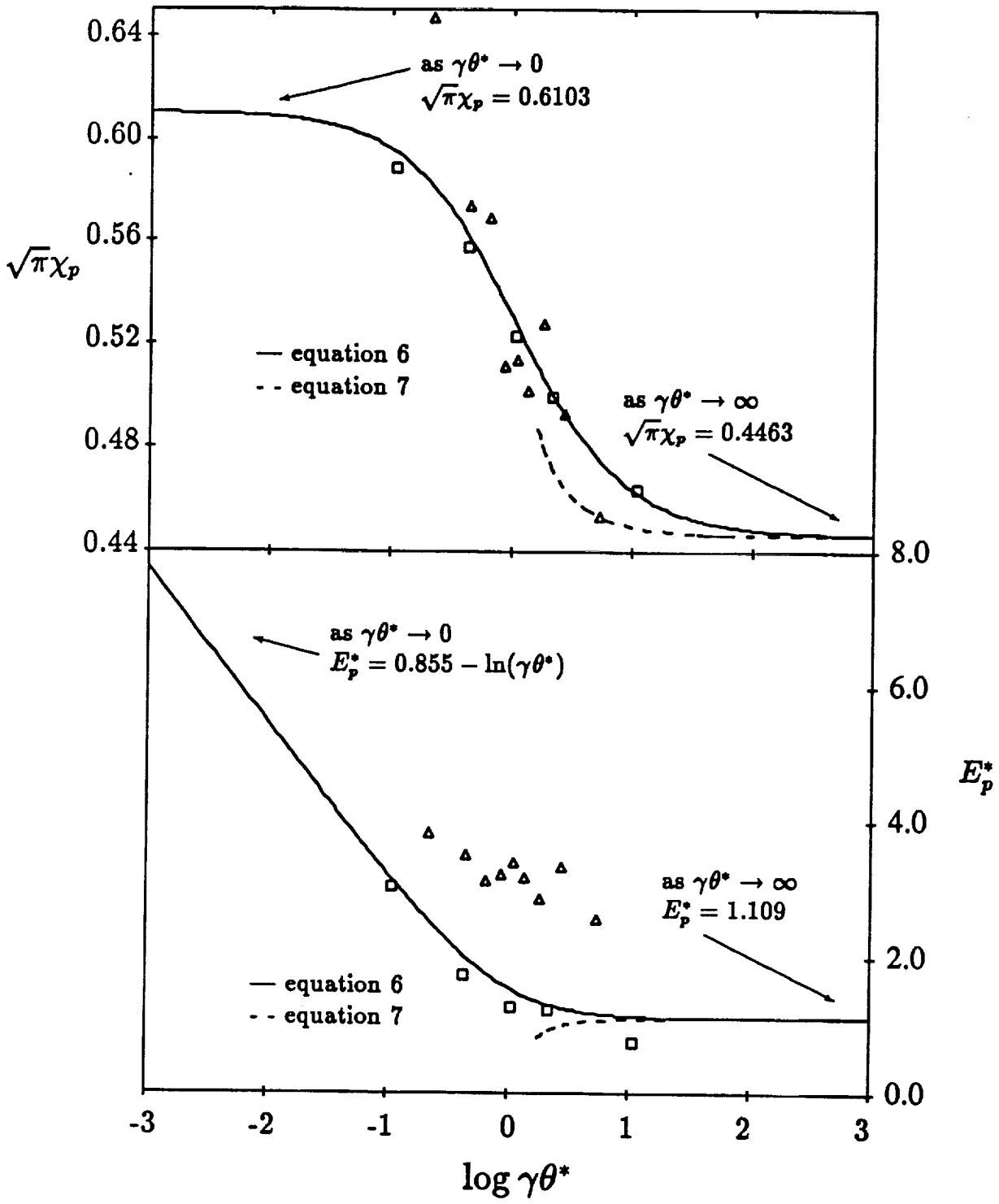

Figure 2: Dimensionless peak currents and potentials for linear-sweep voltammetry on a planar electrode as a function of $\gamma\theta^*$. The solid lines result from the use of equation 6, and the dashed lines result from the use of equation 7 with θ replaced by θ^*. For $\gamma\theta^* \leq 1.60$, equation 7 cannot predict peak values. The symbols are the peak values which were obtained experimentally using the $Fe(CN)_6^{-4}/Fe(CN)_6^{-3}$ redox couple. □—present results; △—Tomcsanyi *et al.* [4] data.

values for the dimensionless peak current and potential can also be obtained for $\gamma\theta^* \rightarrow 0$ by taking the limit of equation 6 as $\gamma\theta^*$ approaches zero which, after some mathematical manipulation, results in

$$\sqrt{\pi}\chi(at)\Big|_{\gamma\theta^* \rightarrow 0} = \frac{1}{\sqrt{\pi}} \int_0^{at} \frac{\exp(-z)}{\sqrt{at - z}}\, dz \tag{9}$$

Following the analogous calculus procedure applied to equation 6 to calculate the peak potential, Newton's method was applied to determine numerically $(at)_p = 0.855$ in the limit of $\gamma\theta^* \rightarrow 0$. The corresponding dimensionless peak current found from equation 9 is 0.6103.

Empirical Correlations

The following one parameter empirical relationship, motivated by the asymptotic trends seen in Figure 2, was fit to the theoretically predicted dimensionless peak currents from equation 6

$$\sqrt{\pi}\chi_p(\gamma\theta^*) = \sqrt{\pi}\chi_p(0) - \left[\sqrt{\pi}\chi_p(0) - \sqrt{\pi}\chi_p(\infty)\right]\left[\frac{\gamma\theta^*}{m + \gamma\theta^*}\right] \tag{10}$$

where $\sqrt{\pi}\chi_p(0)$ and $\sqrt{\pi}\chi_p(\infty)$ are the known dimensionless peak currents at the limits $\gamma\theta^* \rightarrow 0$ and $\gamma\theta^* \rightarrow \infty$, respectively, and m is an empirical parameter which was found by least-squares fit of equation 10 to the data in Figure 2. The resulting correlation is

$$\sqrt{\pi}\chi_p(\gamma\theta^*) = 0.6103 - 0.164\left[\frac{\gamma\theta^*}{1.08 + \gamma\theta^*}\right] \tag{11}$$

The following one parameter empirical relationship, also motivated by the asymptotic trends seen in Figure 2, was fit to the theoretically predicted peak potentials from

equation 6

$$E_p^*(\gamma\theta^*) = \ln\left\{[\exp E_p^*(0)]^m + [\exp E_p^*(\infty)]^m\right\}^{1/m} \tag{12}$$

where $E_p^*(0)$ and $E_p^*(\infty)$ are the known dimensionless peak potentials at the limits $\gamma\theta^* \rightarrow 0$ and $\gamma\theta^* \rightarrow \infty$, respectively. The parameter m was found by least-squares fit to the data in Figure 2. The resulting correlation is

$$E_p^*(\gamma\theta^*) = \ln\left[\left(\frac{2.35}{\gamma\theta^*}\right)^{1.19} + \quad 3.74\right]^{0.84} \tag{13}$$

For $0 < \gamma\theta^* < \infty$, equations 11 and 13 deviate from the exact values by at most 0.1% and 1%, respectively, differences which are visually indistinguishable in Figure 2. The maximum 1% error resulting from equation 13 (which occurs in the vicinity of $\gamma\theta^* = 3$) translates to less than a 0.5 mV ($n = 1$ and $T = 298$ K) error which is experimentally insignificant.

Experimental Results

Linear-sweep voltammetry was conducted using the ferro/ferricyanide redox couple in 1.0 M KCl at five different concentration ratios. The concentration of the ferricyanide was maintained at 0.010 M, and five different ferrocyanide concentrations were used: 0.0010 M, 0.0050 M, 0.010 M, 0.025 M and 0.10 M. Cottrell experiments were run in order to determine γ by taking the ratio of the product of $(i \cdot t^{1/2})$ for oxidation-to-reduction experiments, and $\gamma = 1.09$ was obtained which agrees within 1% of that calculated using the diffusion coefficients for O and R given by Adams [7]. Therefore,

the $\gamma\theta^*$ values for the five concentrations ratios are 10.9, 2.18, 1.09, 0.436, and 0.109. All experiments were performed in a single-compartment cell at room temperature with a 1.6 mm diameter Pt-disk as the working electrode which was not perfectly flush with the surface, and Ag/AgCl as the reference electrode. Voltammograms were generated at nine different sweep rates ranging from 4 to 150 mV/s and were run in duplicate. The *dimensionless* peak current, $\sqrt{\pi}\chi_p$, was obtained by plotting the *dimensional* peak current, i_p, versus the absolute value of the sweep rate to the one-half power, $|v|^{1/2}$. The slope, $\frac{di_p}{d|v|^{1/2}}$, resulting from linear regression of these data was used to calculate $\sqrt{\pi}\chi_p$ since from equation 4

$$\sqrt{\pi}\chi_p(\gamma\theta^*) = \frac{(\mathbf{R}T)^{1/2}}{(n\mathbf{F})^{3/2}C_O^* A\mathcal{D}_O^{1/2}} \frac{di_p}{d|v|^{1/2}} \tag{14}$$

The unknown product $A\mathcal{D}_O^{1/2}$ was determined by performing a series of linear sweeps at which only the oxidized species was present ($\gamma\theta^* = \infty$), and solving equation 14 for $A\mathcal{D}_O^{1/2}$ using $\sqrt{\pi}\chi_p = 0.4463$. The product $A\mathcal{D}_O^{1/2}$ calculated in this manner was then used in equation 14 at the lower values of $\gamma\theta^*$ to obtain $\sqrt{\pi}\chi_p(\gamma\theta^*)$. The peak potential, $(at)_p$, which is independent of the sweep rate, was read directly from the voltammogram for each value of $\gamma\theta^*$, and equation 8 was used to calculate E_p^*.

The experimental dimensionless peak currents and potentials (open squares) are compared to the theoretical values in Figure 2. The experimentally determined peak currents deviate from those theoretically predicted by at most 1%. The measured peak potentials also closely agree with those predicted, except for $\theta^* = 10$ at which a 10

mV deviation occurs. Also included in Figure 2 are the experimental data reported by Tomcsanyi *et al.* [4] (open triangles) from LSV run on a Pt electrode in 1.0 M KCl using the ferro/ferricyanide redox couple. The scatter is larger in these data, but the trend in $\sqrt{\pi}\chi_p(\gamma\theta^*)$ is evident. The peak potentials obtained by Tomcsanyi *et al.* [4] were reported only to the nearest 10 mV and are 30 to 40 mV higher than the theory predicts.

References

[1] Matsuda, Hiroaki; Ayabe, Yuzo *Z. Elektrochem.* **1955**, *59*, 494-503.

[2] Nicholson, Richard S.; Shain, Irving *Anal. Chem.* **1964**, *36*, 706-723.

[3] Farsang, Gyorgy; Rozsondai, Bela; Tomcsanyi, Laszlo *Magy. Kem. Foly.* **1970**, *76*, 233-236.

[4] Tomcsanyi, Laszlo; Farsang, Gyorgy; Rozsondai, Bela *Magy. Kem. Foly.* **1970**, *76*, 236-240.

[5] Golberg, Michael A. *Solution Methods for Integral Equations: Theory and Application*, Michael A. Golberg (ed.); Plenum Press: New York, 1979; Chapter 1.

[6] IMSL, *MATH/LIBRARY, FORTRAN Subroutines for Mathematical Applications*; IMSL: Houston, TX, 1987.

[7] Adams, Ralph N. *Electrochemistry of Solid Electrodes*; Marcel Dekker: New York, 1969; Chapter 8.

Credit

This work was supported by a grant from the NASA-Lewis Research Center (NAG 3-649).

SECTION 5

LINEAR-SWEEP VOLTAMMETRY IN A TUBULAR ELECTRODE: MODEL OF A POROUS ELECTRODE

by

John W. Weidner and Peter S. Fedkiw
Department of Chemical Engineering
North Carolina State University
Raleigh, NC 27695-7905

in preparation for submission to

Journal of the Electrochemical Society

Abstract

A pore in a porous matrix is modeled as a cylindrical electrode and the mass and charge conservation equations are solved in the context of this geometry for the simple redox reaction $O + ne^- \rightleftharpoons R$ when the potential at the pore aperture is ramped linearly in time. The resulting linear-sweep voltammograms depend on the combined effect of kinetic, ohmic and mass-transfer resistances, and determining the transfer coefficient, the standard rate constant or the number of electrons transferred is accomplished by correlating the peak currents and potentials to the governing system parameters. The correlations are established by introducing simplifications at various parameter limits. The first simplification is to neglect axial diffusion which allows the diffusion equation to be analytically solved giving the surface concentration of the redox species in terms of the reaction current and the solution potential at the electrode surface. In the absence of solution resistance, correlations are established in the limit of reversible (Nernstian) and irreversible kinetics which relate the peak currents and potentials to the sweep rate by making use of the known peak values obtained from a planar electrode and a thin-layer cell as the high and low sweep-rate asymptotes, respectively. To quantify ohmic effects in the absence of axial diffusion, an analytical solution to the Laplace equation for the potential is coupled to the analytical solution to the diffusion equation. The peak currents and potentials obtained when axial diffusion is negligible are compared to those obtained when the two-dimensional conservation equations are solved numerically in order to determine under what conditions axial diffusion affects the voltammogram.

1 Introduction

Electroanalytic techniques used to study the kinetics on planar electrodes do not always lend themselves to studying flooded porous electrodes. For example, hydrodynamic methods (e.g. rotating-disk electrodes [1]) are not useful since the reaction surface is inside the porous matrix, and therefore controlling forced convection only affects the material transport to the pore mouth but not within the matrix. In contrast, linear-sweep voltammetry (LSV) in which the electrolyte is stagnant can be used to perform *in situ* kinetic studies on flooded porous electrodes. However, the presently available mathematical methodology that has been developed to determine kinetic parameters using LSV on a planar electrode [2,3,4,5] and in a thin-layer cell [6,7,8] is not applicable for a pore except at limiting sweep rates. At high sweep rates the diffusion layer is small relative to the pore diameter and the voltammogram has the characteristics of LSV on a planar electrode when ohmic resistance is negligible. For deep pores and low sweep rates, radial and axial concentration gradients are small for the major fraction of the pore volume and consequently the pore behaves like a thin-layer cell. However, at moderate sweep rates in the presences of ohmic resistance and axial diffusion, LSV can not be characterized by these two limiting cases, and the result of LSV depends on the combined effects of ohmic, mass-transfer and kinetic resistances.

This paper considers two-dimensional mass and charge transport in a tube-analog

model of a pore in a porous matrix for the reaction

$$O + ne^- \rightleftharpoons R \tag{1}$$

where O and R are soluble oxidized and reduced species, respectively, and n is the number of electrons transferred. If the rate of charge transfer is governed by the Butler-Volmer kinetic expression, the peak current and potential is shown to be a function of six dimensionless parameters. Solving the coupled material and charge conservation partial differential equations numerically is computer intensive (on the order of an hour of CPU per simulation on an IBM/3090), and so carrying out the simulations to correlate the peak currents and potentials to the governing system parameters would be formidable. Therefore, the approach taken in this study is to conduct a parametric evaluation of the two-dimensional model by introducing simplifications at various parameter limits, and use a finite-element numerical solution to bridge the gap between the limiting cases.

The first simplification is to neglect axial diffusion which allows the diffusion equation to be analytically solved giving the surface concentration of the redox species in terms of the reaction current and the solution potential at the electrode surface. Further assuming solution resistance is negligible reduces the computation time over three orders-of-magnitude from the finite-element solution procedure which facilitates correlating the peak currents and potentials to the governing system parameters. In the limit of reversible (Nernstian) and irreversible kinetics, correlations are established which relate the peak currents and potential to the sweep rate by making use of the peak values

obtained from a planar electrode [2,5] and a thin-layer cell [6,7]. Analogous correlations were obtained by Aoki *et al.* [9] for LSV in a rectangular cell for reversible kinetics and negligible ohmic resistance, and later confirmed experimentally [10].

The correlations presented here, which assume solution resistance is negligible, are shown to be useful also when solution resistance is appreciable by *a priori* accounting for ohmic effects. The effect of solution resistance on the voltammogram is quantified by coupling the analytical solution to the one-dimensional, transient diffusion equation to the analytical expression for the solution potential at the electrode surface obtained by solving the two-dimensional Laplace equation [11,12]. In parameter regions in which numerical difficulties prevent voltammograms from being generated from these coupled non-linear equations, the finite-element numerical solution is used.

These correlations can be used to determine whether the electron transfer is reversible or irreversible; if the kinetics are reversible, the correlations may be used to estimate the number of electrons being transferred, or if the kinetics are irreversible, the transfer coefficient and the standard rate constant may be extract from LSV measurements. The results are not valid if material axially diffusing through the pore mouth contributes appreciably to the current. The influence of axial diffusion will depend on the sweep rate for a given pore length since the slower the sweep, the larger is the fraction of the pore volume that will be effected by axial diffusion. Again, the finite-element numerical solution is used to determine the parameter regions in which the correlations

are not valid due to axial diffusion.

2 Mathematical Model

2.1 Assumptions

For the purpose of model development, a porous electrode is assumed to be a collection of identical, non-interconnected cylindrical pores that are filled with electrolyte. Since all pores are equivalent in this idealized electrode, the behavior of the complete electrode will be the same as that predicted for a single pore. Alternatively, it is possible to predict the performance for several different pore sizes and then combine the results based on a given pore-size distribution, as suggested by Winsel [11] and de Levie [13].

A cylindrical tube of diameter d extends from $z = 0$ to a distance L within the electrode. At the pore aperture ($z = 0$), the tube is exposed to the bulk solution containing both oxidized species O and reduced species R. The potential at the inlet of the tube is potentiostatically controlled. The inner wall of the tube is electroactive and the closed end ($z = L$) is inactive. Other assumptions are:

1. The solid phase is isopotential.
2. The reaction is a simple redox process between soluble reacting species.
3. No other processes limit or alter the rates of mass transfer and charge transfer (i.e. no adsorption or desorption and no preceding or following reactions).
4. The electrolyte is well supported so that the solution-phase potential is governed by the Laplace equation.

5. Diffusion is the dominant mass-transfer mechanism.
6. The diffusion coefficients for the two reacting species are equal ($\mathcal{D}_O = \mathcal{D}_R = \mathcal{D}$).
7. Non-faradaic current is negligible.
8. There is no uncompensated ohmic resistance from the reference electrode to the pore aperture.
9. The electrolyte in the reservoir is stagnant and the axial concentration gradient of the reacting species at the pore opening is proportional to the difference between the bulk and inlet concentrations.
10. The potential is radially uniform at the pore aperture.

Assumptions 1-5 are common to most models of porous electrodes, although some, such as that of Grens and Tobias [14,15], include the effects of migration and variable conductivity. Grens [16] addresses the importance of these and other assumptions for the prediction of steady-state current density with a one-dimensional model. For the system to be considered here (i.e. a simple redox reaction in a well-supported electrolyte) it is reasonable to neglect these effects.

The assumption of equal diffusivities (assumption 6) eliminates the diffusion equation for one of the redox species. In a previous study [5] we included the effect of differing diffusion coefficients in the calculations for reversible LSV on a planar electrode, and found for a cathodic sweep when the diffusion coefficient of the oxidized species was 50% higher than that of the reduced species (a significant variation) the peak current was less than 2% greater and the peak potential 5/n mV (T = 298 K) more negative than if the diffusion coefficients were equal. If the kinetics are irreversible, the concentration

distribution of only the reactant species is important and assumption 6 has no effect on the voltammogram. Neglecting uncompensated resistance (assumption 7) limits the usefulness of the results if the potential drop between the reference electrode and the pore aperture is appreciable since the sweep rate at the pore opening would no longer be linear. However, uncompensated resistance may be negligible even when ohmic losses inside the pore are appreciable if the cross-sectional area available for current flow is larger outside the pore then inside, and the distance from the reference electrode to the pore mouth is small. Neglecting double-layer charging (assumption 8) places a lower limit on the reactant concentration since only the reaction current decreases with a decreasing concentration, and an upper limit on the sweep rate since the charging current is a stronger function of the sweep rate than is the reaction current.

Assumption 9 is an attempt to account for mass-transfer resistance in the bulk electrolyte by conceptualizing the pore aperture as an electroactive disk embedded on an insulating plane. Bond *et al.* [17] calculated the steady-state current to such a disk when the reactant surface concentration was uniform, and using Farady's law they related the concentration gradient at the surface to the difference between the bulk and surface concentrations. Assumption 10 is invoked for mathematically convenience; in reality the potential at the tube inlet is radially dependent. A rigorous treatment which would eliminate the last two assumptions would require the simultaneous solution of the governing equations inside and outside the tube — a fairly intractable problem.

2.2 Governing Equations

The concentration of the oxidized species is governed by the time-dependent, two-dimensional diffusion equation

$$\frac{\partial C_O}{\partial t} = \mathcal{D}\left[\frac{\partial^2 C_O}{\partial z^2} + \frac{1}{r}\frac{\partial}{\partial r}\left(r\frac{\partial C_O}{\partial r}\right)\right] \tag{2}$$

where C_O is the oxidized species concentration, $\mathcal{D}$ is the diffusion coefficient, t is the time, and r and z are the radial and axial coordinates, respectively.

The concentration of the reacting species is initially uniform throughout the pore and equal to that in the reservoir (equation 2a). The material flux at the pore inlet is proportional to the difference between the bulk and inlet concentration (equation 2b) with the proportionality constant obtained by modeling the pore aperture as an electroactive disk on an insulating plane [17]. The concentration gradients at the back of the pore (equation 2c) and along the centerline (equation 2d) are zero, and the gradient at the pore wall is proportional to the reaction current (equation 2e). These constraints can be expressed mathematically as

2a) $t = 0; \quad C_O = C_O^o$

2b) $z = 0; \quad \dfrac{\partial C_O}{\partial z} = (-8/\pi d)\,(C_O^o - C_O)$

2c) $z = L; \quad \dfrac{\partial C_O}{\partial z} = 0$

2d) $r = 0; \quad \dfrac{\partial C_O}{\partial r} = 0$

2e) $r = (d/2); \quad \mathcal{D}_O\dfrac{\partial C_O}{\partial r} = \dfrac{-i_n}{n\mathbf{F}}$

where the superscript o indicates the spatially uniform initial concentration, $\mathbf{F}$ is Faraday's constant, and i_n is the local reaction current density at the electrode surface which

is positive for a cathodic reaction. For reactions in which the kinetics are governed by the Butler-Volmer rate equation, i_n is given by

$$i_n = n\mathbf{F}k^o \left\{ C_O \exp\left[-\alpha n f(E_w - E^{o'})\right] - C_R \exp\left[(1-\alpha) n f(E_w - E^{o'})\right] \right\} \qquad (3)$$

where k^o is the standard rate constant, $f \equiv \frac{\mathbf{F}}{\mathbf{R}T}$, α is the cathodic transfer coefficient, E_w and $E^{o'}$ are the solution potential at the tube wall and the formal potential of the redox couple, respectively, and C_R is the reduced species concentration.

Due to the assumption of equal diffusivities, the concentration of the oxidized and reduced species are related by

$$C_O^o + C_R^o = C_O(z,r,t) + C_R(z,r,t) \qquad (4)$$

The Laplace equation governs the solution potential

$$0 = \frac{\partial^2 E}{\partial z^2} + \frac{1}{r}\frac{\partial}{\partial r}\left(r\frac{\partial E}{\partial r}\right) \qquad (5)$$

The potential at the pore opening starts at the equilibrium potential, E_{eq}, and changes linearly with time as set by the sweep rate, $\nu \equiv -\frac{dE}{dt}$ (equation 5a), the potential gradients at the closed end of the pore (equation 5b) and the centerline (equation 5c) are zero, and the gradient at the electrode surface is proportional to the reaction current (equation 5d). These boundary conditions can be expressed mathematically as

5a) $z = 0; \quad (E - E_{eq}) = -\nu t$

5b) $z = L; \quad \frac{\partial E}{\partial z} = 0$

5c) $r = 0; \quad \frac{\partial E}{\partial r} = 0$

5d) $r = d/2; \quad \kappa\frac{\partial E}{\partial r} = i_n$

where κ is the conductivity of the electrolyte.

Equation 2 is rewritten in a dimensionless form as

$$\frac{\partial C_O^*}{\partial \tau} = \frac{\partial^2 C_O^*}{\partial X^2} + \frac{1}{Y}\frac{\partial}{\partial Y}\left(Y\frac{\partial C_O^*}{\partial Y}\right) \tag{6}$$

6a) $\tau = 0; \quad C_O^* = 1$

6b) $X = 0; \quad \frac{\partial C_O^*}{\partial X} = (-4/\pi)\,(1 - C_O^*)$

6c) $X = \gamma; \quad \frac{\partial C_O^*}{\partial X} = 0$

6d) $Y = 0; \quad \frac{\partial C_O^*}{\partial Y} = 0$

6e) $Y = 1; \quad \frac{\partial C_O^*}{\partial Y} = -\sqrt{\sigma} I^*$

where the dimensionless parameters are defined in Table 1, and I^* is the dimensionless local reaction current density at the electrode surface

$$I^* \equiv \frac{i_n}{n\mathrm{F}C_O^o(nf\nu\mathcal{D})^{1/2}} \tag{7}$$

The dimensionless form of equation 5 is

$$0 = \frac{\partial^2 E^*}{\partial X^2} + \frac{1}{Y}\frac{\partial}{\partial Y}\left(Y\frac{\partial E^*}{\partial Y}\right) \tag{8}$$

8a) $X = 0; \quad E^* = \ln \xi - \sigma\tau$

8b) $X = \gamma; \quad \frac{\partial E^*}{\partial X} = 0$

8c) $Y = 0; \quad \frac{\partial E^*}{\partial Y} = 0$

8d) $Y = 1; \quad \frac{\partial E^*}{\partial Y} = (J/\Lambda)\, I^*$

The dimensionless Butler-Volmer equation is

$$I^* = \Lambda\left[C_O^* e^{-\alpha E_w^*} - \left(\frac{1 + \xi - \xi C_O^*}{\xi}\right) e^{(1-\alpha)E_w^*}\right] \tag{9}$$

Parameter	Interpretation	Definition
J	$\frac{\text{ohmic resistance}}{\text{kinetic resistance}}$	$\frac{n^2 f \mathbf{F} k^o d C_O^o}{2\kappa}$
α	cathodic transfer coefficient	
γ	$\frac{\text{length}}{\text{radius}}$	$\frac{2L}{d}$
Λ	$\frac{\text{mass-transfer resistance}}{\text{kinetic resistance}}$	$\frac{k^o}{(nf\nu\mathcal{D})^{1/2}}$
ξ	initial concentration ratio	C_O^o/C_R^o
σ	$\frac{\text{diffusion time}}{\text{sweep time}}$	$\frac{d^2 nf\nu}{4\mathcal{D}}$

Table 1: The definitions of the dimensionless parameters that govern LSV in a cylindrical electrode and their physical interpretation.

Since LSV in a cylindrical electrode depends upon all six parameters listed in Table 1, and each finite-element numerical simulation takes on the order of an hour of CPU time on an IBM/3090, it is desirable to make some simplifications to the above model, as discussed below.

2.3 Negligible Axial Diffusion: With and Without Appreciable Solution Resistance

The first simplification is to neglect axial diffusion. This has practical significance if the duration of a single linear sweep is short since radial diffusion will predominate for the major fraction of the pore volume. Equation 6 reduces to

$$\frac{\partial C_O^*}{\partial \tau} = \frac{1}{Y}\frac{\partial}{\partial Y}\left(Y\frac{\partial C_O^*}{\partial Y}\right) \tag{10}$$

10a) $\tau = 0; \quad C_O^* = 1$

10b) $Y = 0; \quad \frac{\partial C_O^*}{\partial Y} = 0$ 10c) $Y = 1; \quad \frac{\partial C_O^*}{\partial Y} = -\sqrt{\sigma} I^*$

Taking the Laplace transform of equation 10 with respect to τ, solving the resulting ordinary differential equation for the transformed concentration, relating the gradient of the transformed concentration at the electrode surface to the transformed reaction current, and finally applying the convolution property of Laplace transforms to invert back to the time domain results in

$$C_O^*(1,\tau) = 1 - 2\sqrt{\sigma}\int_0^\tau \left[1 + \sum_{n=1}^{\infty} e^{-\lambda_{n_1}^2(\tau-\tau')}\right] I^*(\tau')d\tau' \tag{11}$$

where λ_{n_1} are the zeros of the first-order Bessel function $J_1(\lambda_{n_1}) = 0$. Equation 11 is valid regardless of the reaction rate equation since it relates the concentration of O at the electrode surface to an, as yet, unspecified reaction current.

2.3.1 Reversible Kinetics

For a reversible electrochemical reaction, the surface concentrations of O and R are coupled through the Nernst equation to the solution potential by

$$\frac{C_O(d/2,t)}{C_R(d/2,t)} = \exp\left[nf(E_w - E^{o'})\right] \tag{12}$$

where $E^{o'}$ is the formal potential. Writing equation 12 in dimensionless form and utilizing equation 4 gives

$$C_O^*(1,\tau) = \frac{(1+\xi)e^{E_w^*}}{\xi\left[1+e^{E_w^*}\right]} \tag{13}$$

where E_w^* is an arbitrary function of time. Substituting equation 11 into equation 13, and solving for the integral expression results in a Volterra integral equation of the first kind

$$\int_0^\tau \left[1 + \sum_{n=1}^{\infty} e^{-\lambda_{n_1}^2(\tau-\tau')}\right] I_{rev}^*(\tau')d\tau' = \frac{\xi - e^{E_w^*}}{2\xi\sqrt{\sigma}\left[1+e^{E_w^*}\right]} \equiv g(E_w^*) \tag{14}$$

where the subscript *rev* denotes reversible kinetics.

The dimensionless current, $I_{rev}^*(\tau)$, can be determined numerically [2] by approximating the integral in equation 14 as

$$\int_0^\tau \left[1 + \sum_{n=1}^{\infty} e^{-\lambda_{n_1}^2(\tau-\tau')}\right] I_{rev}^*(\tau')d\tau' \approx \sum_{\mu=0}^{q-1} B_\mu I_{rev}^*(qh - \mu h) \tag{15}$$

where h is the width of each interval such that $\tau = qh$ and $\tau' = \mu h$. The coefficients B_μ are determined by approximating the unknown function $I^*_{rev}(\tau')$ by linear expressions in the individual intervals, integrating the left side of equation 15, and solving for the coefficients. For $\mu = 0$ this procedure results in

$$B_0 = \frac{h}{2} - \sum_{n=1}^{\infty} \left(\frac{1 - e^{-\lambda_{n_1}^2 h} - \lambda_{n_1}^2 h}{\lambda_{n_1}^4 h} \right) \tag{16}$$

and for μ from 1 to $q-1$

$$B_\mu = h + \sum_{n=1}^{\infty} \frac{e^{-\lambda_{n_1}^2 h(\mu-1)}}{\lambda_{n_1}^4 h} \left(1 - e^{-\lambda_{n_1}^2 h}\right)^2 \tag{17}$$

Substituting equation 15 into equation 14, and solving for $I(qh)$ gives

$$I^*_{rev}(qh) = \frac{g(E^*_w) - \sum_{\mu=1}^{q-1} B_\mu I^*_{rev}(qh - \mu h)}{B_0} \tag{18}$$

If it is further assumed that the solution resistance is negligible, then the potential at the tube wall is equal to the potential applied at the pore opening ($E^*_w = \ln \xi - \sigma\tau$), and the peak current and potential is obtained by stepping equation 18 through time until a maximum in the current is obtained. The voltammograms generated by the numerical solution of equation 18 depend only upon σ and ξ.

In order to assess the accuracy of the integral approximation given in equation 15, an alternative solution to equation 10 was generated by solving the equation for a unit step change in the potential at the tube wall and using Duhamel's superposition principle [18] to account for the time-dependent boundary condition given by equation 13. The

resulting current-potential expression is

$$I^*_{rev}(\tau) = 2(1+\xi)\sqrt{\sigma}\sum_{n=1}^{\infty}\int_0^{\tau}\frac{\exp\left[-[\sigma\tau' + \lambda^2_{n_o}(\tau-\tau')]\right]}{[1+\xi\exp(-\sigma\tau')]^2}d\tau' \qquad (19)$$

where λ_{n_o} are the zeros of the zeroth-order Bessel function $J_o(\lambda_{n_o}) = 0$.

In the presence of appreciable solution resistance, the two-dimensional Laplace equation for the potential (equation 8) must be solved to obtain E^*_w. Winsel [11] and Viner and Fedkiw [12] solved equation 8 to determine E^*_w as a function of axial position for an arbitrary time-dependent potential variation at the pore opening. For a linearly varying potential at the pore mouth, the result is

$$E^*_w(X,\tau) = -\sigma\tau + \frac{2J}{\Lambda\gamma}\sum_{n=1}^{\infty}\frac{I_o(\beta_n)}{\beta_n I_1(\beta_n)}\sin\beta_n X\int_0^{\tau} I^*(X',\tau)\sin\beta_n X'\,dX' \qquad (20)$$

where $I_o(\beta_n)$ and $I_1(\beta_n)$ are zero- and first-order modified Bessel functions, respectively, and $\beta_n \equiv (n-\frac{1}{2})\pi/\gamma$. Equation 20 is valid regardless of the reaction rate equation.

2.3.2 Irreversible Kinetics

When the kinetics are irreversible, the back reaction may be ignored and for a cathodic reaction the Butler-Volmer kinetic expression given in equation 9 reduces to

$$I^*_{irrev} = \Lambda C^*_O e^{-\alpha E^*_w} \qquad (21)$$

where the subscript *irrev* indicates irreversible kinetics. Substituting equations 11 and 15 into equation 21 and solving for the current results in

$$I^*_{irrev}(qh) = \frac{\Lambda\left[1 - 2\sqrt{\sigma}\sum_{\mu=1}^{q-1} B_\mu I^*_{irrev}(qh-\mu h)\right]}{e^{\alpha E^*_w} + 2\sqrt{\sigma}\Lambda B_0} \tag{22}$$

where B_0 and B_μ are given in equations 16 and 17, respectively. Equations 20 and 22 are coupled when solution resistance is appreciable.

3 Results and Discussion

Correlations which relate the peak currents and potentials obtained from LSV in a tubular electrode to the governing dimensionless parameters are obtained for reversible (Nernstian) and irreversible kinetics by assuming solution resistance and axial diffusion are negligible (equations 18 or 22). Solution resistance is then accounted for by coupling the analytical solution to the one-dimensional diffusion equation to the analytical expression for the solution potential at the electrode surface (equation 20). In parameter regions in which numerical difficulties prevent these coupled non-linear equations from being evaluated, a finite-element numerical solution is used to solve equations 6 and 8. The parameter regions in which axial diffusion may be ignored is determined by comparing the peak currents obtained with and without the axial component of the diffusion equation included in the model.

3.1 Negligible Axial Diffusion

3.1.1 Negligible Solution Resistance

Reversible kinetics

In the absence of solution resistance, equation 18 was applied by letting $E_w^* = (\ln \xi - \sigma\tau)$ for 51 different values of σ ranging from 10^{-1} to 10^4 at 30 different values of ξ ranging from 10^{-3} to 10^3. Richardson extrapolation [20] was used to speed the convergence of the infinite series for the B_μ coefficients (equations 16 and 17), and all other non-oscillating series given in this paper. Figure 1 shows the dimensionless peak currents and potentials as a function of $\sqrt{\sigma}$ for three different values of ξ. Only some of the calculations up to $\sqrt{\sigma} = 20$ are shown in Figure 1 in order not to clutter the figures and to emphasize the behavior at large and small σ. As $\sigma \to \infty$, the diffusion layer is small relative to the pore diameter and the peak values approach those obtained from a planar electrode (i.e. the peak current is proportional to $\nu^{1/2}$ and the peak potential is sweep rate independent). Weidner and Fedkiw [5] developed empirical correlations for the peak current and potential as a function of ξ for LSV on a planar electrode and these are listed in Table 2. The peak current obtained from LSV on a planar electrode is within 5% of the peak current obtained from that on a cylindrical electrode for $\sigma > 300$, and the peak potentials are within $5/n$ mV of each other for $\sigma > 40$.

As the sweep rate approaches zero ($\sigma \to 0$), the radial concentration gradients

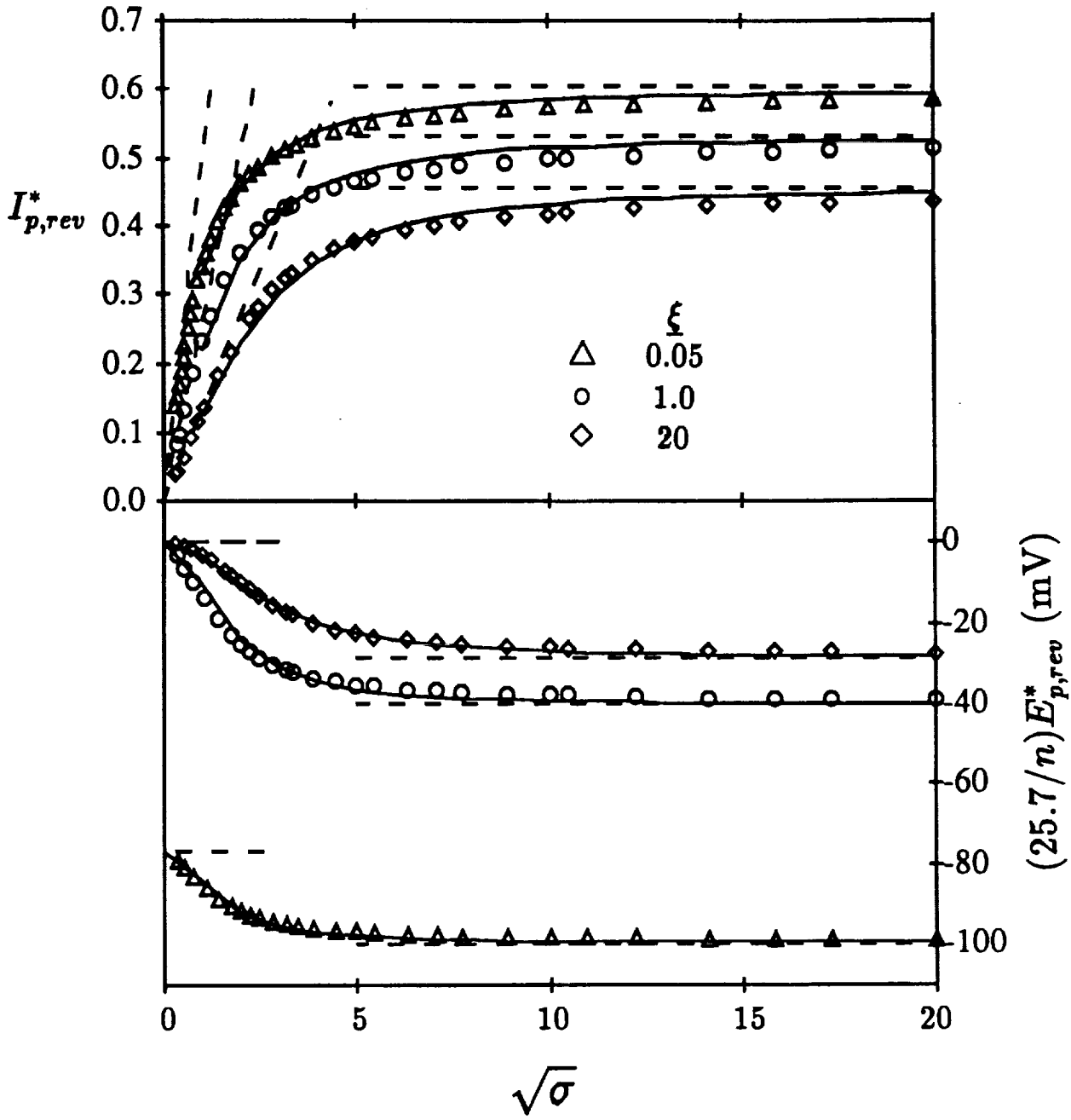

Figure 1: Dimensionless peak currents and potentials for linear-sweep voltammetry in a cylindrical electrode when the kinetics are reversible, and ohmic losses and the axial diffusion flux are negligible. The symbols result from the use of equation 18 and the solid lines are the correlations which were fit to the calculations (equations 24 and 26). The dashed lines as $\sigma \rightarrow \infty$ are the dimensionless peak currents and potentials obtained from LSV on a planar electrode [5], and those as $\sigma \rightarrow 0$ are the equations for the dimensionless peak currents and potentials in a thin-layer cell [6] (see Table 2). The potential, in mV, is for $T = 298$ K.

Peak Current or Potential Expression	Reference	σ Limit
$\xi \geq 1;$ $\quad \dfrac{(1+\xi)\sqrt{\sigma}}{8\xi}$ $I^*_{p,rev}$(thin-layer) = $\xi \leq 1;$ $\quad \dfrac{\sqrt{\sigma}}{2(1+\xi)}$	[6]	$\sigma < \exp\left[3.91\left(\dfrac{\xi}{0.59+\xi}\right) - 2.81\right]$
$\xi \geq 1;$ $\quad 0$ $E^*_{p,rev}$(thin-layer) = $\xi \leq 1;$ $\quad \ln \xi$	[6]	$\sigma < 0.5$
$I^*_{p,rev}(\text{planar}) = 0.6103 - 0.164\left(\dfrac{\xi}{1.08+\xi}\right)$	[5]	$\sigma > 300$
$E^*_{p,rev}(\text{planar}) = \ln\left[\left(\dfrac{2.35}{\xi}\right)^{1.19} + 3.74\right]^{0.84}$	[5]	$\sigma > 40$

Table 2: Expressions for the peak current and potential on a planar electrode and in a thin-layer cell for reversible kinetics. The σ limit indicates the value at which the peak currents are within 5% and the peak potentials within $5/n$ mV ($T = 298$ K) of the values calculated from LSV in a cylindrical pore if solution resistance and axial diffusion are negligible.

approach zero and the voltammograms have the characteristics of LSV in a thin-layer cell. Hubbard and Anson [6] derived a current-potential relationship for LSV in a thin-layer cell when only the oxidized species is initially present ($\xi = \infty$) and the voltage is swept in the negative direction. They found that the cathodic current is proportional to the sweep rate and given by

$$I_{rev}(\text{thin-layer}) = \frac{n^2 f \mathbf{F} \nu V C_O^o e^{E^*}}{A\left[1 + e^{E^*}\right]^2} \tag{23}$$

where V is the volume of the thin-layer cell. When the initial concentration of the reduced species is not negligibly small, equation 23 remains valid except that C_O^o is replaced by $(C_O^o + C_R^o)$. When $C_O^o > C_R^o$ ($\xi > 1$), the peak is obtained by differentiating equation 23 with respect to time and setting the resulting equation equal to zero. The potential which satisfies the resulting equation is the formal potential ($E_p^* = 0$) which, when substituted into equation 23, gives the peak current. However, when $C_O^o < C_R^o$ ($\xi < 1$) the starting potential is negative with respect to the formal potential and therefore the peak current occurs at the start of the sweep ($E_p^* = \ln \xi$) and the current decays as the oxidized species is reduced. We see from Figure 1 that the dimensional peak current is proportional to the sweep rate at low σ and the peak potential approaches zero as predicted from equation 23. The dimensionless peak values in the limit of $\sigma \rightarrow 0$ are listed in Table 2. The upper limit of σ for which the the thin-layer-cell approximation is valid is a strong function of ξ. For $\xi \geq 5$, the peak current obtained from equation 18 is within 5% of $I_{p,rev}^*(\text{thin-layer})$ given in Table 2 when $\sigma < 2$, but for $\xi \leq 0.1$, σ has to

be less than 0.1 for the two currents to be within 5% of each other. A one-parameter least-squares fit was performed for the upper σ limit as a function of ξ, and the result is shown in Table 2

The following empirical relationship, motivated by the asymptotic trends seen in Figure 1, was fit to the dimensionless peak currents calculated from equation 18

$$I^*_{p,rev}(\sigma) = \left[I^*_{p,rev}(\text{thin-layer})^m + I^*_{p,rev}(\text{planar})^m\right]^{1/m} \tag{24}$$

where m is an empirical parameter which was found by least-squares fit of equation 24 to the dimensionless peak currents for 51 different values of σ. The parameter m was obtained at 30 different values of ξ, and a two-parameter empirical equation for m was generated as a function of ξ and is listed in row 1 of Table 3.

Substituting $I^*_{p,rev}(\text{thin-layer})$ for $\xi \geq 1$ and $I^*_{p,rev}(\text{planar})$ into equation 24 along with the definitions for I^* and σ gives

$$\left(\frac{\hat{i}_p}{\sqrt{\nu}}\right)^m = \left[\frac{\pi n^2 f \mathbf{F} d^2 L C^o_O (1+\xi)}{16\xi}\right]^m \nu^{m/2} + \left[1.57(n\mathbf{F})^2 d^2 L C^o_O I^*_{p,rev}(\text{planar})\right]^m \tag{25}$$

where $\hat{i}_p$ is the peak current which would be measured if solution resistance was negligible. Therefore, plotting $\left(\hat{i}_p/\sqrt{\nu}\right)^m$ versus $\nu^{m/2}$ should yield a straight line if the kinetics are reversible, and the slope and intercept may be used to estimate n. Table 3 lists the proper way to plot LSV data in order to yield a straight line, along with the equations for the resulting slope and intercept.

The following empirical relationship, also motivated by the asymptotic trends seen

	Eqn.	m	Plot	slope	intercept
$\xi \geq 1$ $I^{\circ}_{p,rev}$ $\xi \leq 1$	24	$-0.565\left[\frac{\xi^{2.62}}{0.729+\xi^{2.62}}\right]-1.475$	$\left(\frac{i_p}{\sqrt{\nu}}\right)^m$ vs $\nu^{m/2}$	$\left[\frac{\pi n^2 f \mathbf{F} d^2 L C^{\circ}_O (1+\xi)}{16\xi}\right]^m$ $\left[\frac{\pi n^2 f \mathbf{F} d^2 L C^{\circ}_O}{4(1+\xi)}\right]^m$	$\left(1.57(n\mathbf{F})^2 d^2 L C^{\circ}_O I^{\circ}_p(\text{planar})\right)^m$ $\left(1.57(n\mathbf{F})^2 d^2 L C^{\circ}_O I^{\circ}_p(\text{planar})\right)^m$
$E^{\circ}_{p,rev}$	26	$5.07\left[\frac{\xi^{2.68}}{1.98+\xi^{2.68}}\right]+2.13$	$\left[\frac{\left(E^{\circ}_p - E^{\circ}_p(\text{thin-layer})\right)}{\nu}\right]$ vs $\left(E^{\circ}_p - E^{\circ}_p(\text{planar})\right)$	$-\frac{nfd^2}{4m\mathcal{D}}$	0
$I^{\circ}_{p,irrev}$	27	-1.81	$\left(\frac{i_p}{\sqrt{\nu}}\right)^m$ vs $\nu^{m/2}$	$(0.289n^2 f \mathbf{F} d^2 L C^{\circ}_O \alpha)^m$	$\left(1.56n\mathbf{F}LC^{\circ}_O d\sqrt{\alpha n f \mathcal{D}}\right)^m$
$E^{\circ}_{p,irrev}$	29	2.05	$\left(\nu e^{\alpha E^{\circ}_p}\right)^m$ vs $\nu^{m/2}$	$\left(\frac{0.458k^{\circ}}{\sqrt{\alpha n f \mathcal{D}}}\right)^m$	$\left(\frac{4k^{\circ}}{\alpha n f d}\right)^m$

Table 3: Correlations for the peak currents and potentials as a function of the sweep rate, ν, and the proper way to plot the data in order to determine the desired kinetic parameters.

in Figure 1, was fit to the theoretically predicted peak potentials from equation 18

$$E^*_{p,rev}(\sigma) = \left[E^*_{p,rev}(\text{planar}) - E^*_{p,rev}(\text{thin-layer})\right]\left[\frac{\sigma}{m+\sigma}\right] + E^*_{p,rev}(\text{thin-layer}) \qquad (26)$$

The two-parameter empirical equation for m as a function of ξ is listed in row 2 of Table 3.

Only one parameter (m) was used to fit the peak current and potential calculations in order to facilitate a graphical analysis of experimental data. The disadvantage to a one-parameter fit is that equation 24 is only accurate to within 5% and equation 26 to within $5/n$ mV (T = 298K). Although this error may be significant, peak values estimated from equations for LSV on a planar electrode or in a thin-layer cell result in even larger errors if the value of σ is outside the range listed in Table 2. Therefore, these correlations provide more accurate estimates of the peak values at moderate sweep rates than is possible with planar or thin-layer theory alone.

The error in the simulated voltammogram arising from the integral approximation given in equation 15 was assessed by comparing the peak currents obtained from equation 18 to those obtained from equation 19 which was derived using Duhamel's superposition principle. Although the peak current for equation 19 may be obtained by generating an entire voltammogram, a more convenient analytical procedure was derived by differentiating equation 19 with respect to τ and setting the result equal to zero. The potential which satisfies the resulting expression is the peak potential which, when substituted into equation 19, specifies the peak current. Newton's method was used to solve

the resulting non-linear equation for the peak potential generated from this procedure. At $\xi = 1000$, the peak currents for σ varying from 10^{-1} to 10^{4} calculated from the two current-potential relationships agreed to within 0.1% of each other, verifying the integral approximation.

Irreversible kinetics

In the absence of solution resistance, equation 18 was applied by letting $E_w^* = (\ln \xi - \sigma\tau)$ for 51 different values of σ ranging from 10^{-1} to 10^{4} at 9 different values of α ranging from 0.1 to 0.9. As stated by Matsuda and Ayabe [3] and reaffirmed in our calculations, the kinetics can be assumed irreversible if $\Lambda \leq 10^{-3}$ and was the value used in the calculations. Figure 2 shows the dimensionless peak currents and potentials as a function of $\sqrt{\sigma}$ for three different values of α. As with reversible kinetics the peak values approach those obtained from a planar electrode as $\sigma \rightarrow \infty$ [4] and approach the thin-layer peak values as $\sigma \rightarrow 0$ [7]. Table 4 lists the peak current and potential expressions for LSV on a planar electrode and in a thin-layer cell which are used in the correlations.

The following empirical relationship, which is analogous to that used when the kinetics were reversible, was fit to the theoretically predicted dimensionless peak currents obtained from equation 22

$$I_{p,irrev}^*(\sigma) = \left[I_{p,irrev}^*(\text{thin-layer})^m + I_{p,irrev}^*(\text{planar})^m\right]^{1/m} \qquad (27)$$

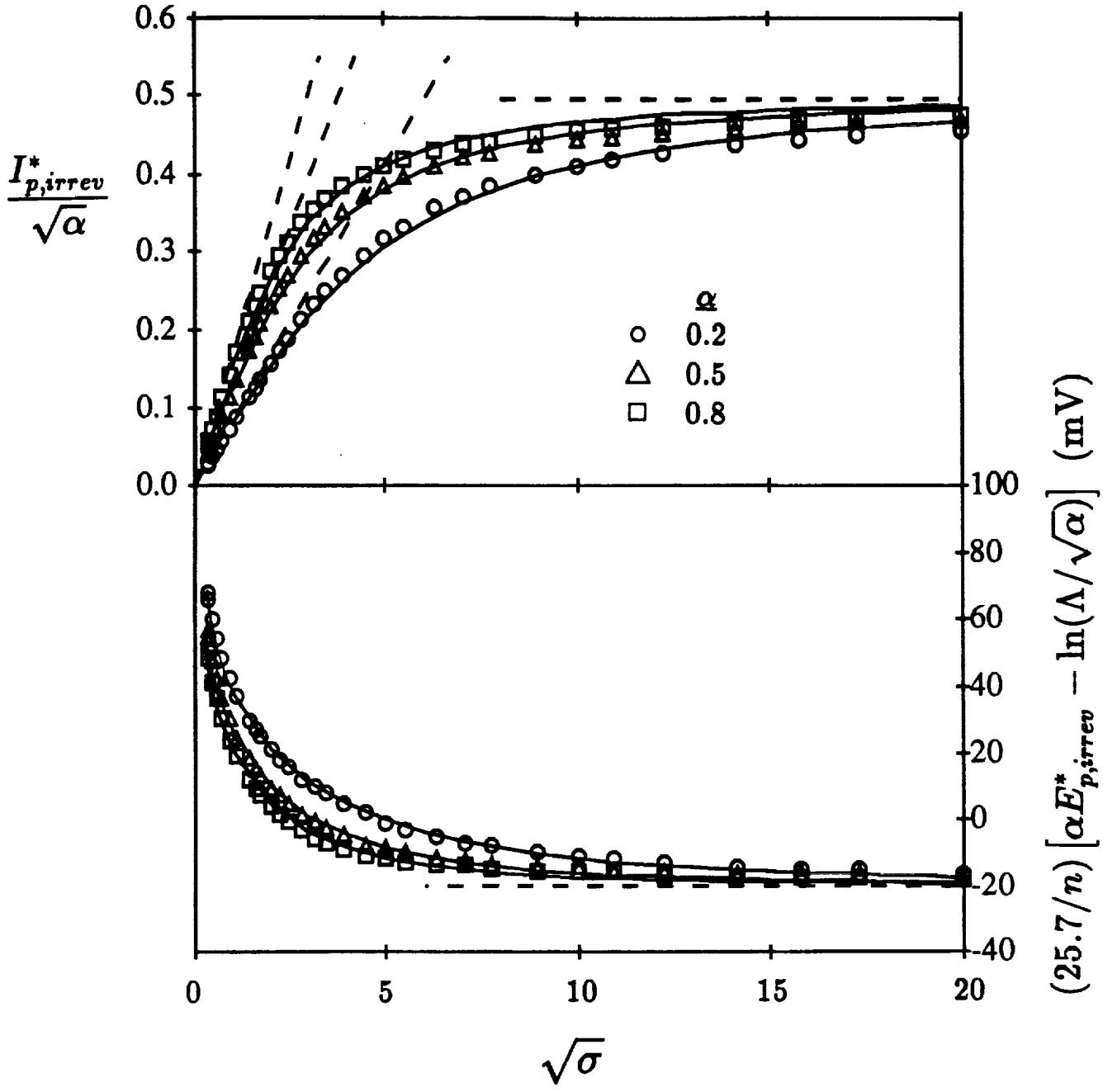

Figure 2: Dimensionless peak currents and potentials for linear-sweep voltammetry in a cylindrical electrode when the kinetics are irreversible and ohmic resistance and axial diffusion are negligible. The symbols result from the use of equation 22 and the solid lines are the correlations which were fit to the calculations (equations 27 and 28). The dashed lines as $\sigma \rightarrow \infty$ are the dimensionless peak currents and potentials obtained from LSV on a planar electrode [4], and those as $\sigma \rightarrow 0$ are the equations for the dimensionless peak current in a thin-layer cell [7] (see Table 4). The potential ordinate approaches $(-\ln \sigma)$ as $\sigma \rightarrow 0$. The potential, in mV, is for $T = 298$ K.

Peak Current and Potential Expression	Reference	σ Limit
$I^*_{p,irrev}(\text{thin-layer}) = 0.1896\,\alpha\sqrt{\sigma}$	[7]	$\sigma < 3$
$E^*_{p,irrev}(\text{thin-layer}) = \frac{1}{\alpha}\left[\ln\left(\frac{\Lambda}{\sqrt{\alpha}}\right) - \ln\left(\frac{\sqrt{\alpha\sigma}}{2}\right)\right]$	[7]	$\sigma < 12$
$I^*_{p,irrev}(\text{planar}) = 0.4958\sqrt{\alpha}$	[2]	$\sigma > 2000$
$E^*_{p,irrev}(\text{planar}) = \frac{1}{\alpha}\left[\ln\left(\frac{\Lambda}{\sqrt{\alpha}}\right) - 0.780\right]$	[2]	$\sigma > 400$

Table 4: Expressions for the peak current and potential on a planar electrode and in a thin-layer cell for irreversible kinetics. The σ limit indicates the value at which the peak currents are within 5% and the peak potentials within $5/n$ mV ($T = 298$ K) of the values calculated from LSV in a cylindrical pore if solution resistance and axial diffusion are negligible.

were m is an empirical parameter which was found by least-squares fit of equation 27 to the dimensionless peak currents for 51 different values of σ. The fit was performed at nine different values of α, and all the m values were within 1% of each other. Taking m as a constant, α can be estimated from the slope of a $\left(\hat{i}_p/\sqrt{\nu}\right)^m$ versus $\nu^{m/2}$ plot. The slope and intercept of the straight line and the average value for the parameter m are listed in row 3 of Table 3.

The following empirical relationship, motivated by the asymptotic trends seen in Figure 2, was fit to the theoretically predicted dimensionless peak potentials obtained from equation 22

$$\exp \alpha E^*_{p,irrev}(\sigma) = \left[\left(\exp \alpha E^*_{p,irrev}(\text{thin-layer})\right)^m + \left(\exp \alpha E^*_{p,irrev}(\text{planar})\right)^m\right]^{1/m} \quad (28)$$

where m is an empirical parameter which was found by least-squares fit of the above equation to the peak potentials. The nine m values, corresponding to the different α values, were within 5% of each other with the average value listed in row 4 of Table 3. Equation 28 may be simplified and the peak potentials written in the form which is plotted in Figure 2 giving

$$\alpha E^*_{p,irrev} - \ln(\Lambda/\sqrt{\alpha}) = 0.488 \ln\left[0.202 + \left(\frac{2}{\sqrt{\alpha\sigma}}\right)^{2.05}\right] \quad (29)$$

After α is determined from the experimental peak-current data, the peak potentials can be used to estimate the standard rate constant, k^o, by plotting the data as indicated in row 4 of Table 3 and evaluating the slope and intercept.

3.1.2 Appreciable Solution Resistance

Reversible kinetics

Since the current and the potential are position dependent when solution resistance is appreciable, and the solution potential at the tube wall (equation 20) is a function of the total current, equations 18 and 20 are coupled and must be solved simultaneously. The total current as a function of applied potential at each time step was obtained by dividing the pore into N segments of equal length and calculating the current in each segment using equation 18 with the total current being the sum of the individual segment currents. The N current and N potential equations were simultaneously solved using the IMSL [19] non-linear equation-solver subroutine DNEQNJ which makes use of a user-supplied Jacobian. The Filon algorithm [21] was used to perform the integration in equation 20, and a binomial averaging algorithm [22] was used to extrapolate the infinite series. Unfortunately, numerical difficulties prevented the non-linear equation solver from converging in a parameter region were solution resistance was appreciable. Increasing the number of divisions in the pore may have allowed the non-linear equation solver to converge, but at $N = 20$ the amount of computer time per simulation was on the order of that needed to solve numerically the two coupled partial differential equations, and so the following procedure was used to account for solution resistance when the kinetics are reversible.

Equations 6 and 8 were simultaneously solved using the IMSL [19] finite-element procedure PDE/PROTRAN, and the Butler-Volmer kinetic expression (equation 9) was numerically integrated along the tube wall using the IMSL [19] subroutine DQDAGS at each time step. The Butler-Volmer equation is valid for reversible kinetics as long as Λ is large. Matsuda and Ayabe found that the kinetics could be assumed reversible if $\Lambda \geq 15$, and so a value of $\Lambda = 50$ was used in the calculations to insure reversibility. It was observed that for $\sigma = 1$ and $\xi = 100$ the peak currents and potentials depend only upon the grouping $(J/\Lambda)\gamma^2 \equiv \Theta$ as long as γ was greater than 100. The lower bound on γ is due to appreciable axial diffusion of material into the pore through the pore aperture. The effect of axial diffusion on the voltammogram will be addressed further in the next section.

The peak currents, normalized by the peak currents which would be obtained if solution resistance was negligible, are plotted in Figure 3 as a function of Θ. From Figure 3 we see that at $\Theta = 1$ solution resistance diminishes the peak current by less than 1%, but at $\Theta = 10$ the peak current has been reduce by 13% due to ohmic effects, and by 24% at $\Theta = 20$.

In order to assess the numerical accuracy of the finite-element numerical solution, an alternative current calculation was performed by numerically integrating the current in the electrolyte, i_s, at the inlet to the tube using Ohm's law ($i_s = \kappa \nabla E$). The potential gradient was estimated by using a three-point-derivative formula. The two independent

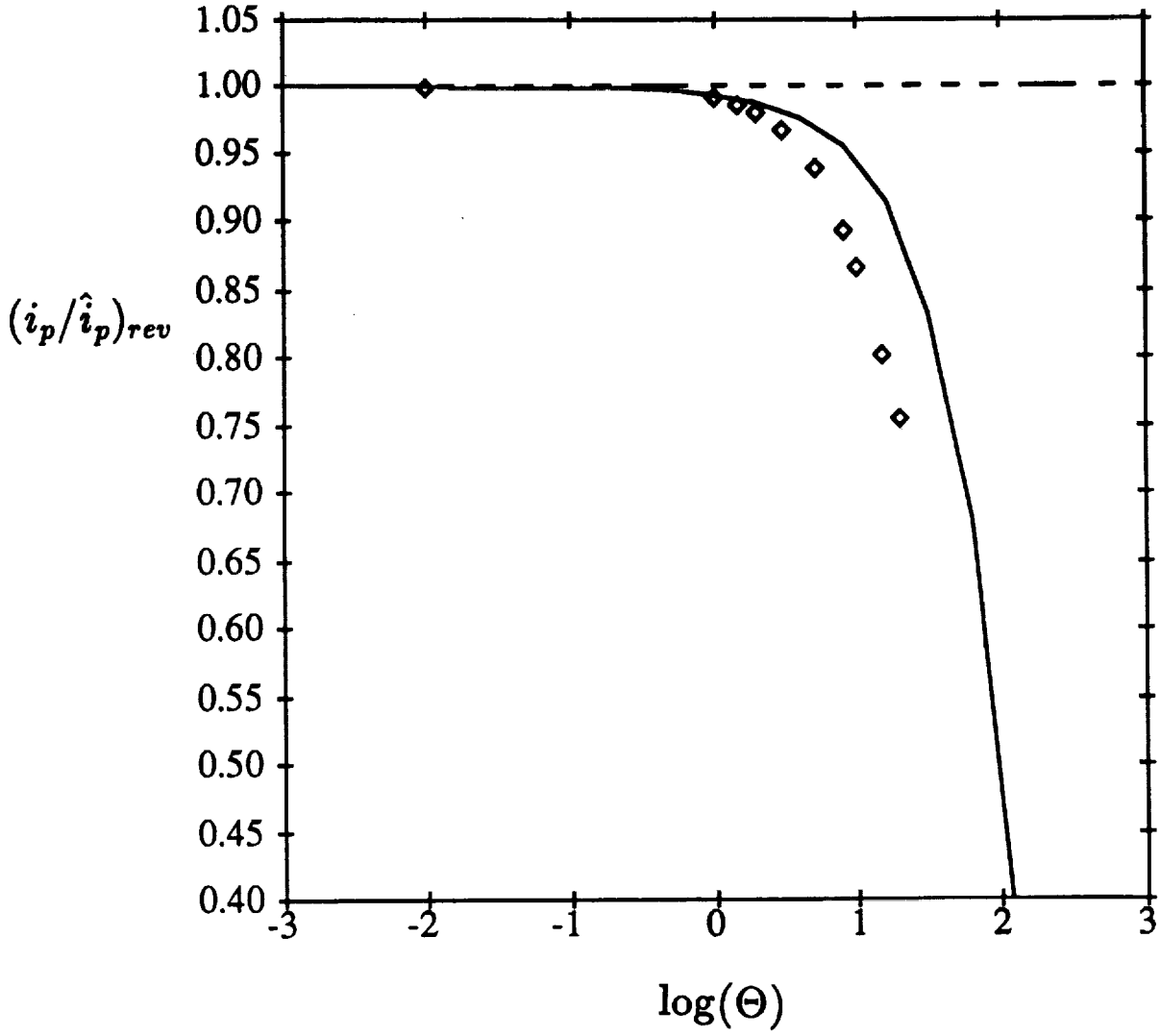

Figure 3: The normalized peak current in a cylindrical electrode when the kinetics are reversible as a function of the dimensionless grouping $(J/\Lambda)\gamma^2 \equiv \Theta$. The peak current, i_p, is normalized with respect to the peak current which would be obtained if solution resistance was negligible, $\hat{i}_p$. The symbols are the results from the finite-element numerical solution, and the solid line is the correlation which was established for a thin-layer cell [24] when $\sigma = 1$.

current calculations agreed to within 2% of each other for the results given in Figure 3, but for $\Theta > 20$ the the discrepancy between the currents was larger than 2%.

As shown in Section 3.1.1, the voltammogram will have characteristics of LSV in a thin-layer cell when $\sigma < 3$ in the absence of solution resistance. Hinman *et al.* [23] used a network model to simulate LSV in a thin-layer cell to account for ohmic distortion when the kinetics are reversible. Three assumptions, in addition to the ones made in obtaining the results shown in Figure 3, were made in their analysis: (1) the potential is radially uniform, (2) only the oxidized species is present initially ($\xi = \infty$), and (3) the rate at which the potential changes with time is uniform throughout the cell as set by the sweep rate. Using the same set of assumptions we applied a continuum model to the thin-layer cell [24], and found that the normalized peak current was a function of a single variable which in the present nomenclature is $\Theta\sqrt{\sigma}$. The resulting correlation is plotted in Figure 3 for $\sigma = 1$.

Both models predict a precipitous drop in the peak current as Θ is increased past one, but the drop is steeper in the present calculations. For example, at $\Theta = 10$ the peak current calculated from the thin-layer model [24] is 9% higher than that calculated by numerically solving the two coupled partial differential equations (equations 6 and 8). The assumption of a radially-uniform potential should be valid at $\sigma = 1$ since the thin-layer approximation holds for $\sigma < 3$ (see Tables 2) and a small concentration gradient leads to a small potential gradient. The difference in the *normalized* peak currents

resulting from a non-zero initial concentration of the reduced species should be negligible since the difference between the peak current for $\xi = 100$ and $\xi = \infty$ in a thin-layer cell when solution resistance is negligible is only about 1%. The difference in the peak currents predicted from the two models is therefore expected to result from assuming the sweep rate is uniform throughout the pore. As indicated by equation 23, the local current is not only a function of the axial dependent potential, but it is also directly proportional to the local rate of change of the potential, $d|E|/dt$. Since $d|E|/dt$ decreases with distance into the pore, setting $d|E|/dt$ equal to the sweep rate, ν, overestimates the current.

Yet to be determined is the functional dependence of the normalized peak current on σ and Θ. From our previous study [24] we expect the normalized peak currents to only be a function of the grouping $\Theta\sqrt{\sigma}$ when the thin-layer approximation holds. The shift in the peak potential due to ohmic effects also needs to be quantified. The effect of ξ on the peak current in the presence of solution resistance has not been explored either, but the effect on the normalized peak current is expected to be small.

Irreversible kinetics

The effect of solution resistance on the voltammogram when the kinetics are irreversible and axial diffusion is negligible was determined by simultaneously solving equations 20 and 22 with the pore divided into 10 segments. This value for N was used since no noticeable effect on the peak current was observed for larger N, and the computer

time per simulation scaled as N^2. The normalized peak currents were found to depend only upon Θ for $\sigma \geq 20$, and $\Theta\sqrt{\sigma}$ for $\sigma \leq 2$. Figures 4 and 5 show the normalized peak currents obtained for $\sigma \geq 20$ and $\sigma \leq 2$, respectively. For $\sigma \geq 20$, numerical difficulties prevented the non-linear equation solver from converging for $\Theta > 10$, and so in this Θ range equations 6 and 8 had to be solved using the finite-element numerical solution. Comparisons between the two solution procedures were made at $\Theta \leq 10$ for $\sigma = 100$ and the resulting peak currents were within 0.2% of each other as long as $\gamma \geq 10$, a difference which would be visually indistinguishable in Figure 4. All the calculations shown in Figure 5 were obtained from the finite-element solution.

A totally empirical, three parameter least-squares-fit of the results in Figure 4 produced the following correlation for the normalized peak current as a function Θ for $\sigma \geq 20$.

$$(i_p/\hat{i}_p)_{irrev} = \left[(1.372 - 0.438\log\Theta)^{-7.50} + 1\right]^{-0.1333} \tag{30}$$

Five different values of σ between 20 and 500 were used in the correlation in which Θ ranged from 10^{-2} to 10^2. A three parameter least-squares-fit was also made of the calculations in Figure 5 which resulted in the the following correlation for the normalized peak current as a function $\Theta\sqrt{\sigma}$ for $\sigma \leq 2$.

$$(i_p/\hat{i}_p)_{irrev} = \left[\left(1.606 - 0.497\log\Theta\sqrt{\sigma}\right)^{-6.77} + 1\right]^{-0.1477} \tag{31}$$

In establishing this correlation, σ ranged from 0.2 to 2, and Θ from 10 to 100.

The simulations which established equations 30 and 31 were run with $\alpha = 0.5$. It is

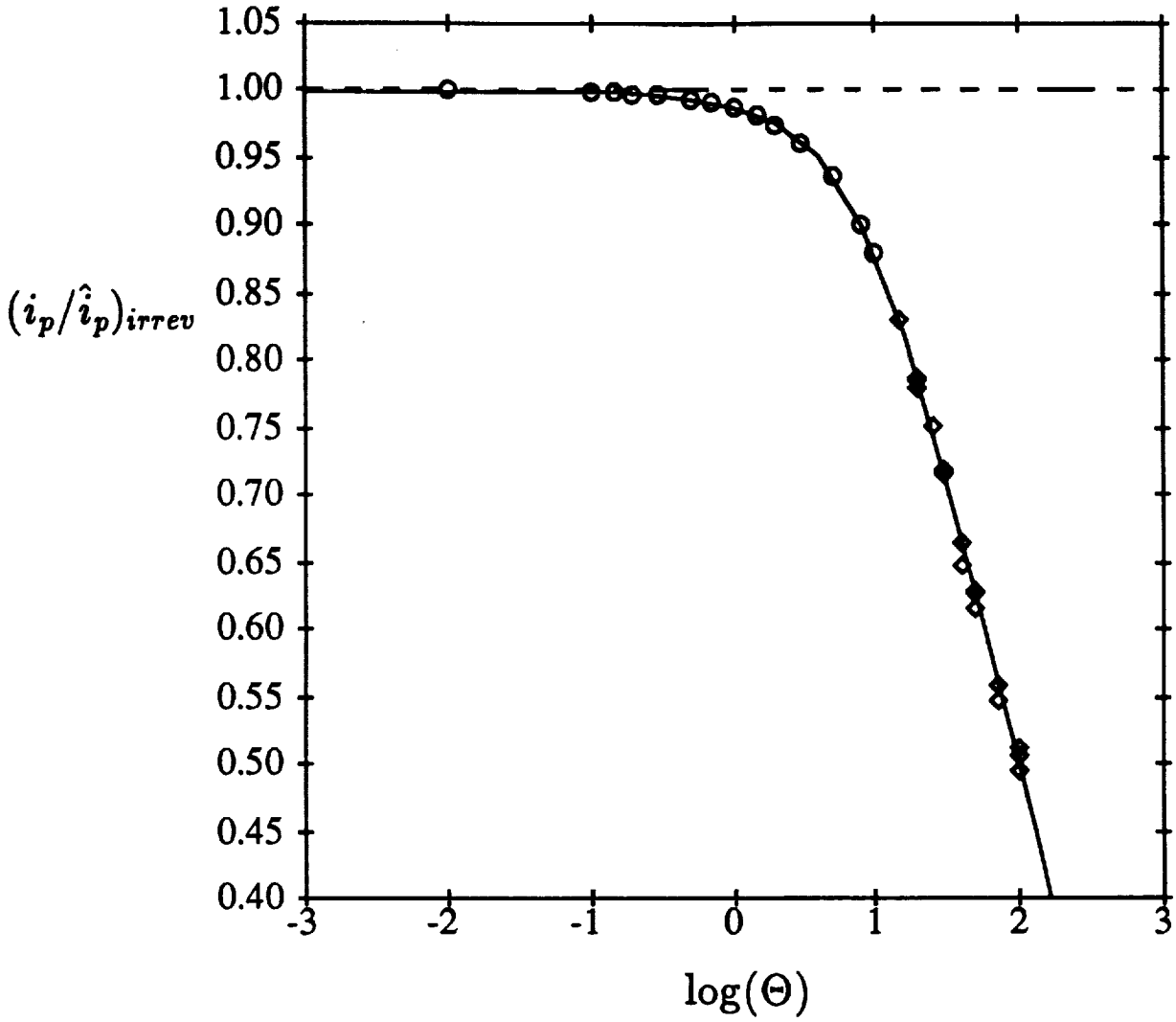

Figure 4: The normalized peak current in a cylindrical electrode as a function Θ for $\sigma \geq 20$ when the kinetics are irreversible and axial diffusion is negligible. The peak current, i_p, is normalized with respect to the peak current which would be obtained if solution resistance was negligible, $\hat{i}_p$. The circles (o) are the results from simultaneously solving equations 20 and 22, and the diamonds ($\diamond$) are the results from the finite-element solution. The solid line is the correlation which was fit to the calculations (equation 30).

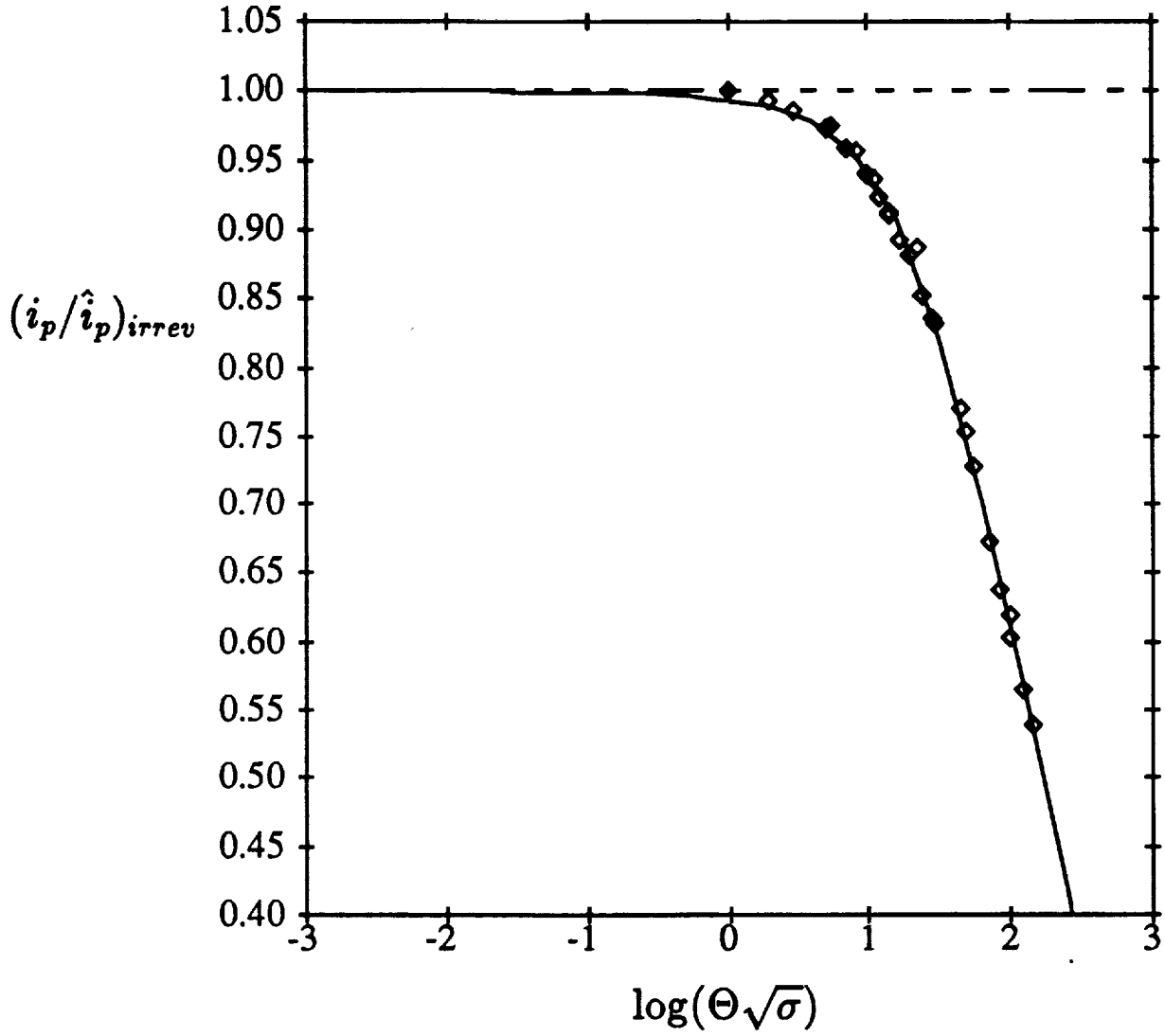

Figure 5: The normalized peak current in a cylindrical electrode as a function $\Theta\sqrt{\sigma}$ for $\sigma \leq 2$ when the kinetics are irreversible and axial diffusion is negligible. The peak current, i_p, is normalized with respect to the peak current which would be obtained if solution resistance was negligible, $\hat{i}_p$. The symbols are the results from the finite-element solution, and the solid line is the correlation which was fit to the calculations (equation 31).

not expect that normalized peak currents will be a strong function of α (if at all), but that remains to be determined. Analogous correlations to those for the normalized peak currents as a function of Θ still need to be established for the shift in the peak potential due to solution resistance. Also, more simulations are required in order to quantify the ohmic effects in the σ region between 2 and 20.

In order to check the accuracy of the finite-element calculations, the currents obtained from the integration of the Butler-Volmer kinetic expression were compared to those resulting from radially-integrating Ohm's law at the pore aperture, and for $\sigma \geq 20$ and $\Theta \leq 100$ an agreement within 1% was obtained. No calculations were performed at larger values of Θ since at $\Theta = 100$ the voltammogram is severly distorted with the peak spread over tens of mV, and so simulating LSV beyond this point would be of no practical use.

3.2 Effect of Axial Diffusion

The above correlations will not hold if appreciable material diffuses into the pore from the reservoir which will occur if σ is too small for a given γ. In order to determine the lower bound of σ as a function of γ above which axial diffusion can be neglected, the finite-element technique was used to solve equation 6 with the potential at the pore wall set by the sweep rate. For the case of reversible kinetics, the Nernst equation was used as the boundary condition at the electrode surface instead of the Bulter-Volmer equation,

and it was observed that for $\xi = 10$, the current due to diffusion of material into the pore contributes less than 2% to the peak current if $\sigma > 42/\gamma$. This bound of σ is valid for $\xi > 10$, and results in a percentage error less than two for $\xi < 10$. When the kinetics were irreversible, it was observed that axial diffusion can be ignored as long as $\sigma > 75/\gamma$.

Material diffusing through the pore mouth will contribute a larger fraction of the current as the potential becomes more non-uniform since the potential driving force at the pore aperture will need to be increased in order to drive the reaction at the back of the pore to an appreciable rate. Therefore, a larger value of σ will be required at a given γ so that the assumption of negligible axial diffusion is valid. The relationship between σ and γ has yet to be determined when solution resistance is appreciable.

4 Summary

Correlations were established for determining kinetic parameters from LSV in a cylindrical electrode. Due to the complex dependence of the peak currents and potentials on the governing parameters, simplifications were introduced at various parameter limits. The first simplification was to neglect axial diffusion which allows the diffusion equation to be analytically solved giving the surface concentration of the redox species in terms of the reaction current and the solution potential at the electrode surface. Further assuming solution resistance is negligible reduces the computation time over three orders-of-magnitude from the finite-element solution numerical procedure facilitated the

establishment of the desired correlations. In the limit of reversible (Nernstian) and irreversible kinetics, correlations were established which relate the peak currents and potentials to the sweep rate by making use of the peak expressions on a planar electrode and in a thin-layer cell.

The correlations, which are established assuming solution resistance is negligible, are also useful when solution resistance is appreciable since the currents can be adjusted to give peak data which would have been obtained in the absence of ohmic effects. The effect of solution resistance on the peak current was quantified for the irreversible-kinetic case for $\sigma \geq 20$ and $\sigma \leq 2$, but more simulations are needed to quantify the peak currents for σ falling between these two limits. More calculations also need to be performed in order to establish correlations when the kinetics are reversible. Correlations have yet to be established for the peak potential calculations which has been collected thus far.

Acknowledgement—This work was supported by a grant from the NASA-Lewis Research Center (NAG 3-649).

References

[1] Bard A.J., and L.R. Faulkner, **Electrochemical Methods**, John Wiley & Sons, New York, NY (1980).

[2] Delahay, P., *J. Am. Chem. Soc.*, **55**, 1190 (1953).

[3] Matsuda, H. and Y. Ayabe, *Z. Elektrochem.*, **59**, 494 (1955).

[4] Nicholson, R.S. and I. Shain, *Anal. Chem.*, **36**, 706 (1964).

[5] Weidner, J.W. and P.S. Fedkiw, *Anal. Chem.*, May (1990).

[6] Hubbard, A.T. and F.C. Anson, *Anal. Chem.*, **38**, 58 (1966).

[7] Hubbard, A.T., *J. Electroanal. Chem.*, **22**, 165 (1969).

[8] Hubbard, A.T. and F.C. Anson, **Electroanalytical Chemistry**, A.J. Bard (ed.), **4**, 129-214, Marcel Dekker, New York, NY (1970).

[9] Aoki, K., K. Tokuda and H. Matsuda, *J. Electroanal. Chem.*, **146**, 417 (1983).

[10] Daruházi, L., K. Tokuda and G. Farsang, *J. Electroanal. Chem.*, **264**, 77 (1989).

[11] Winsel, A., *Z. Elektrochem.*, **66**, 287 (1962). Translated by J. Newman, February, 1973. Available as Document No. UCRL-Trans-1495 from the National Technical Information Service, U.S. Department of Commerce, Front Royal, Virginia.

[12] Viner, A.S. and P.S. Fedkiw, *J. Electrochem. Soc.*, **137**, 1435 (1990).

[13] de Levie, R., **Adv. in Electrochem. and Electrochem. Eng.**, P. Delahay and C.W. Tobias (eds.), **6**, 329 (1967).

[14] Grens, E.A., II, and C.W. Tobias *Ber. Bunsenges. Phys. Chem.*, **68**, 236 (1964).

[15] Grens, E.A., II, and C.W. Tobias, *Electrochim. Acta*, **10**, 761 (1965).

[16] Grens, E.A., *Electrochim. Acta*, **15**, 1047 (1970).

[17] Bond, A.M., D. Luscombe, K. B. Oldham and C. G. Zoski, *J. Electroanal. Chem.*, **249**, 1 (1988).

[18] Hildebrand, F.B., **Advanced Calculus for Applications-Second Edition**, Prentice-Hall, Englewood Cliffs, NJ (1976).

[19] IMSL, **MATH/LIBRARY, FORTRAN Subroutines for Mathematical Applications**, IMSL, Houston, TX (1987).

[20] Bender, C.M. and S.A. Orszag, **Advanded Mathematical Methods for Scientists and Engineers**, McGraw Hill, New York, NY (1978).

[21] Davis, P.J. and P. Rabinowitz, **Methods of Numerical Integration**, Academic Press, New York, NY (1975).

[22] Dahlquist, G. and Å. Björk, **Numerical Methods**, Translated by N. Anderson, Prentice Hall, New York, NY (1974).

[23] Hinman, A.S., S. Pons and J. Cassidy, *Electrochim. Acta*, **30**, 89 (1985).

[24] Fedkiw, P.S. and J.W. Weidner, *Electrochim. Acta*, **33**, 421 (1988).

Notation

A	electrode area, cm^2
B_μ	coefficient in integral approximation
C_O	concentration of oxidized species of redox couple, mol/cm^3
C_R	concentration of reduced species of redox couple, mol/cm^3
C_O^o	initial concentration of oxidized species of redox couple, mol/cm^3
C_R^o	initial concentration of reduced species of redox couple, mol/cm^3
C_O^*	C_O/C_O^o
$\mathcal{D}$	diffusion coefficient of the redox species, cm^2/s
E	solution potential, V
$E^{o'}$	formal potential of redox couple, V
E_{eq}	equilibrium initial potential, V
E^*	dimensionless potential, $nf(E - E^{o'})$
f	$\mathbf{F/RT}$ V/equiv
$\mathbf{F}$	Faraday's constant, C/equiv
h	width of interval in integral approximation
i	total reaction current, A
$\hat{i}$	total reaction current when solution resistance in negligible, A
i_n	current density at electrode surface, A/cm^2
i_s	current density in solution, A/cm^2
i_o	exchange current density, A/cm^2
I_o	zeroth-order modified Bessel function
I_1	first-order modified Bessel function
I^*	dimensionless current, $i_n/(nfC_O^o\sqrt{nf\nu\mathcal{D}})$
J_o	zeroth-order Bessel function
k^o	standard rate constant, cm/s
m	empirical parameter
n	number of e^- in redox couple
$\mathbf{R}$	gas constant, J/(mol·K)
t	time, s
T	temperature, K
r	distance from center of pore, cm
V	volume of pore, cm^3
X	dimensionless axial coordinate, $2z/d$
Y	dimensionless radial coordinate, $2r/d$
z	distance from the pore aperture, cm

Greek

β_n	$(n-\frac{1}{2})\pi/\gamma$
λ_{n_o}	zeros of zeroth-order Bessel function J_o
λ_{n_1}	zeros of first-order Bessel function J_1
κ	conductivity of the electrolyte, $(\text{ohm} \cdot \text{cm})^{-1}$
ν	sweep rate, $-\frac{dE}{dt}$, V/s
τ	dimensionless time, $td/2\mathcal{D}$

Subscripts

irrev	irreversible kinetics
p	value at peak of voltammogram
rev	reversible kinetics
w	value at tube wall

SECTION 6

ON-GOING WORK

The PhD candidate, Mr. Weidner, is currently performing linear sweep voltammetry experiments for a number of redox couples in a tubular electrode to confirm the theoretical calculations presented in Section 5. Upon completion of this work he will then repeat these same measurements for a nickel electrode and attempt to verify the methodology for this electrode reaction. We anticipate completion of the dissertation no later than May, 1991 and we shall forward, when available, the dissertation and any additional papers which result from the project.